Chem Soc Rev

TUTORIAL REVIEW

View Article Online
View Journal | View Issue

Check for updates

Cite this: *Chem. Soc. Rev.*, 2026, **55**, 5590

Received 21st February 2026

DOI: 10.1039/d6cs00220j

rsc.li/chem-soc-rev

Precision graphene nanoribbons: chemical strategies for tailored edge, backbone, and electronic structure

Xinyu Chen,†[a] Yuanhuan Qiu,†[a] Jin-Jiang Zhang,[b] Xiangyang Liu,*[a] Ji Ma, *[ce]
Xu Wang*[a] and Xinliang Feng *[bd]

Graphene nanoribbons (GNRs), quasi-one-dimensional graphene nanostructures, are promising candidates for next-generation electronic, optoelectronic, and spintronic applications due to their tunable (opto-)electronic and magnetic properties. The intrinsic properties of GNRs are critically determined by atomic-scale structural parameters such as width, edge configuration, and backbone architecture, all of which can be precisely designed and regulated through bottom-up synthetic strategies. Recent years have witnessed remarkable progress in the bottom-up chemical synthesis of GNRs, and a diverse array of innovative structural engineering strategies, such as edge topology modulation, backbone modification, and heterojunction construction, have been developed. These advances have enabled precise control over GNR characteristics and have deepened understanding of their structure–property relationships, correlating atomic-scale features with electronic band structure, charge-carrier mobility, spin polarization, and topological states. This review summarizes the latest developments of precision GNRs, focusing on how rational design and synthetic breakthroughs have transformed GNRs into a versatile, atomically precise materials platform. By integrating advanced synthesis and characterization methods, the research field is paving the way for functional GNR-based devices in future electronic, spintronic, and quantum information systems.

Key learning points

1. Fundamental knowledge of precision GNRs, including the definition and significance, the principles of bottom-up synthetic strategies, and the critical structure–property correlations.
2. Chemical strategies for tailed edges in GNRs, including the conventional and unconventional edge topologies, edge doping with heteroatoms, and chemical functionalization on the edges.
3. Backbone engineering in GNRs, including the creation of hybrid GNRs, and the incorporation of non-benzenoid rings, periodic nanopores, or helical structure within the ribbon backbone.
4. Heterostructure engineering in GNRs, including recent advances in synthetic methods and the distinct electronic features emerging from these heterostructures, such as tailored band alignment and topological interface states.
5. Current challenges and future perspectives on the precision synthesis, structure characterization and functional device integration of defined GNRs.

1. Introduction

Graphene, a two-dimensional crystalline material composed of sp^2-hybridized carbon atoms, has been regarded as a transformative material for next-generation technologies due to its extraordinary electronic, thermal, and mechanical properties.[1–9] Its ultra-high carrier mobility and outstanding stability offer great promise for high-frequency electronics and flexible devices.[4,7] However, the intrinsic zero bandgap of graphene, arising from its hexagonal symmetry and linear band dispersion at the Dirac points, fundamentally limits its use in electronics and optoelectronics by impeding current switching.[3,9] Thanks to the quantum

---

[a] *College of Polymer Science and Engineering, State Key Laboratory of Advanced Polymer Materials, Sichuan University, Chengdu, 610065, P. R. China. E-mail: wangxu@scu.edu.cn, lxy@scu.edu.cn*

[b] *Max Planck Institute of Microstructure Physics, Weinberg 2, Halle 06120, Germany. E-mail: xinliang.feng@mpi-halle.mpg.de*

[c] *Beijing National Laboratory for Molecular Sciences, CAS Key Laboratory of Organic Solids, Institute of Chemistry, Chinese Academy of Sciences, Beijing 100190, China. E-mail: maji26@iccas.ac.cn*

[d] *Center for Advancing Electronics Dresden and Faculty of Chemistry and Food Chemistry, Technische Universität Dresden, Dresden 01062, Germany*

[e] *College of Materials Science and Optoelectronic Technology, University of Chinese Academy of Sciences, Beijing 100049, China*

† These authors contributed equally: Xinyu Chen and Yuanhuan Qiu.

confinement effect, graphene nanoribbons (GNRs), as nanometer-wide stripes of graphene, acquire a bandgap.[9–13] Their physicochemical properties are governed by atomically precise structures, enabling systematic modulation of electronic, optical, and magnetic properties through the engineering of width, edge configuration, backbone topology, and doping.[11,14–19] This precise

Xinyu Chen

Xinyu Chen received his BS in Polymer Science and Engineering from Sichuan University, China, in 2020. He is currently pursuing his PhD degree under the supervision of Prof. Xu Wang at the College of Polymer Science and Engineering, Sichuan University. His research focuses on the precise bottom-up synthesis of solution-processable non-planar graphene nanoribbons, the investigation of their intrinsic optoelectronic properties, and their applications in single-molecule electronics.

Yuanhuan Qiu

Yuanhuan Qiu received his BS degree from the College of Polymer Science and Engineering at Sichuan University in 2025. He is currently pursuing a PhD degree under the supervision of Prof. Xu Wang at the same university. His main research focuses on the development and application of high-performance polyimides, as well as the precise synthesis of graphene nanoribbons via bottom-up approaches.

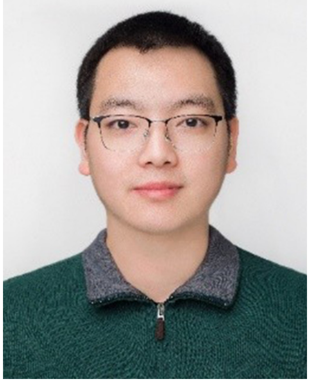

Jin-Jiang Zhang

Jin-Jiang Zhang received his PhD in synthetic chemistry under the supervision of Xinliang Feng at Technische Universität Dresden in 2022. He is currently a postdoctoral researcher at the Max Planck Institute of Microstructure Physics in Halle. His research focuses on the precise synthesis of boron-doped nanographenes and graphene nanoribbons with novel structures and intriguing properties, and their applications in organic nanoelectronics.

Ji Ma

Ji Ma received his PhD in 2019 from Technische Universität Dresden, Germany. He was then appointed as a research group leader at Technische Universität Dresden and later, in 2022, at the Max Planck Institute of Microstructure Physics. In January 2024, he joined the University of Chinese Academy of Sciences as a principal investigator, and he is now a professor at the Institute of Chemistry, Chinese Academy of Sciences (ICCAS). His research focuses on the precise synthesis of functional quantum nanocarbons for applications in organic spintronics and quantum technologies.

Xu Wang

Xu Wang is now a full professor at the College of Polymer Science and Engineering, Sichuan University. He received his PhD degree in materials science in 2014 from Sichuan University and then worked at the University of New Brunswick and Technische Universität Dresden as a postdoctoral researcher and visiting scholar, respectively. His current scientific interests include the synthesis of high-performance polymers and novel nanocarbon materials.

Xinliang Feng

Xinliang Feng has been Full Professor and the Head of the Chair of Molecular Functional Materials at Technische Universität Dresden since 2014. Since 2021, he has been the Director of the Max Planck Institute of Microstructure Physics (Halle), Germany. His current scientific interests include organic synthesis, supramolecular chemistry of π-conjugated systems, bottom-up synthesis and top-down fabrication of graphene and graphene nanoribbons, 2D polymers and supramolecular polymers, as well as 2D carbon-rich conjugated polymers for (opto)electronic applications and for energy storage and conversion.

tunability positions GNRs as a key material for advanced applications in nanoelectronics, spintronics, photonics, and quantum information science.[10,20–28]

In contrast to top-down methods (*e.g.*, electron-beam lithography or carbon nanotube unzipping),[29–39] the bottom-up strategy offers programmable control over structural parameters of GNRs.[16,17,20,40,41] This precise control, in turn, enables tailored modulation of GNR optoelectronic properties, including band structure and charge-carrier transport. Recent years have seen the development of diverse GNR structures alongside detailed investigations into their unique physical and chemical properties.[20,25,42–49] Beyond conventional methods such as modulating the width of GNRs with armchair edges[13,17,40,50–55] or chemically functionalizing zigzag edges,[56–59] a range of more sophisticated structural modulation strategies has recently emerged.[44,45,47,60–70] For instance, the synthesis of GNRs with unconventional edge topologies—such as cove-edge, cove-zigzag hybrid, fjord-edge, chiral-edge, and Janus edge structures—has enabled systematic investigations into the intrinsic relationship between edge geometry and electronic structure.[45,61–63,66,70–74] Furthermore, covalent functionalization of GNR edges in solution phase not only enables further fine-tuning of their band structure, carrier type, and transport properties but also significantly improves their solution processability.[25,42–44,48,60,68,75] This provides a crucial foundation for fabricating high-performance GNR-based single-electron devices.[20,24,25,67] While edge and width modulation are pivotal, backbone engineering of GNRs also offers a distinct and versatile strategy for modulating their intrinsic properties. This approach, which encompasses doping, symmetry modification *via* non-hexagonal rings, and heterojunction formation, has enabled GNRs to exhibit novel quantum phenomena and tailored opto-electronic properties, including topological boundary states and spin-polarized channels.[65,76–86] Thus, systematically organizing these emerging strategies for engineering GNR structures will deepen the understanding of their structure–property relationships and establish a foundation for designing advanced nanoelectronic and quantum devices. In this context, a timely review linking the latest progress in the molecular engineering of GNR edges, backbones, and electronic structures would provide useful guidance to accelerate the transition of GNRs from fundamental synthetic and physical property exploration toward device integrations.

In this review, we will summarize representative advances in the structural design and property investigation of GNRs over the past few years. We first introduce the fundamental structural concepts of GNRs and the correlation between structural topology and electronic structure. We then review recent progress in structural engineering from three key perspectives: edge engineering, backbone engineering, and heterostructure construction. The section on edge engineering examines how modulating edge structure, introducing edge heteroatom substitution, and implementing edge functionalization significantly influence the electronic, magnetic, and transport properties of GNRs. Backbone engineering focuses on electronic structure tuning *via* strategies such as heteroatom doping into the backbone, as well as the synthesis of nonbenzenoid, porous, and curved GNRs. Regarding GNR heterostructures, we will highlight synthetic approaches and the distinct electronic features that emerge from such systems, including tailored band alignment and topological interface states. Finally, we will conclude with a summary of the key developments discussed in this review and provide a forward-looking perspective on the remaining challenges and future opportunities in the precision synthesis and functional exploration of GNRs.

2. Fundamental knowledge of GNRs

The defining characteristic of GNRs lies in the fact that their physicochemical properties—most critically their electronic structure—are determined not only by their chemical composition but also, and often dominantly, by their precise topological configuration.[10–12,14,16,87] A comprehensive understanding of prevalent GNR architectures and their governing electronic mechanisms is thus essential to unraveling electron transport in these quantum-confined systems. This foundational knowledge directly links structural topology to electronic behavior, establishing the basis for the rational design of next-generation nanoelectronic materials.

Based on their edge configurations, which originate from the crystallographic cutting directions of a graphene sheet, GNRs can be primarily classified into two types, namely zigzag-edged GNRs (ZGNRs) and armchair-edged GNRs (AGNRs) (Fig. 1).[11,13,88] The properties of GNRs are profoundly dictated by their edge structures (Fig. 1). For instance, ZGNRs exhibit localized spin-polarized edge states, with ferromagnetic ordering at each zigzag edge and antiferromagnetism across the GNR. This exotic state can be tuned by applying an in-plane transverse electric field, thereby inducing half-metallicity in ZGNRs.[56,88,89] AGNRs exhibit possible metallic or semiconducting behavior depending on their width.[50,52–55,90,91] Specifically, AGNRs can be further classified into three categories. Among these families, ribbons belonging to the $N = 3\mathrm{p}$ and $N = 3\mathrm{p} + 1$ classes, where N denotes the number of carbon dimer lines across the ribbon width and p is an integer, exhibit a bandgap that scales inversely with the ribbon width.[50,51,92] In contrast, ribbons in the $N = 3\mathrm{p} + 2$ class are theoretically predicted to be narrow-bandgap or quasi-metallic.[14,52,54,90]

In addition to the edge structures defined by the graphene lattice orientation, such as armchair- and zigzag-type edges, recent years have witnessed an increasing number of reports of novel GNR edge structures achieved by introducing various types of carbon atom vacancies at AGNR and ZGNR edges.[62,64,71] For example, periodically introducing single-carbon-atom vacancies along the ZGNR edge can produce GNRs with a cove-edge geometry,[61] as illustrated in Fig. 2. The steric hindrance between adjacent C–H bonds in the cove regions typically forces such GNRs to adopt a non-planar [4]helicene configuration. Furthermore, other edge motifs, such as gulf edges and fjord edges, have also been developed.[66,69] The gulf edge is created by removing multiple carbon atoms from a zigzag edge, resulting in a series of relatively wide, cove-like indentations (Fig. 2). The fjord edge incorporates [5]helicene units, whose strong spatial crowding induces a helically twisted conformation along the GNR edges.

Furthermore, by controlling the arrangement of carbon vacancies along the edges of ZGNRs, GNRs with periodic

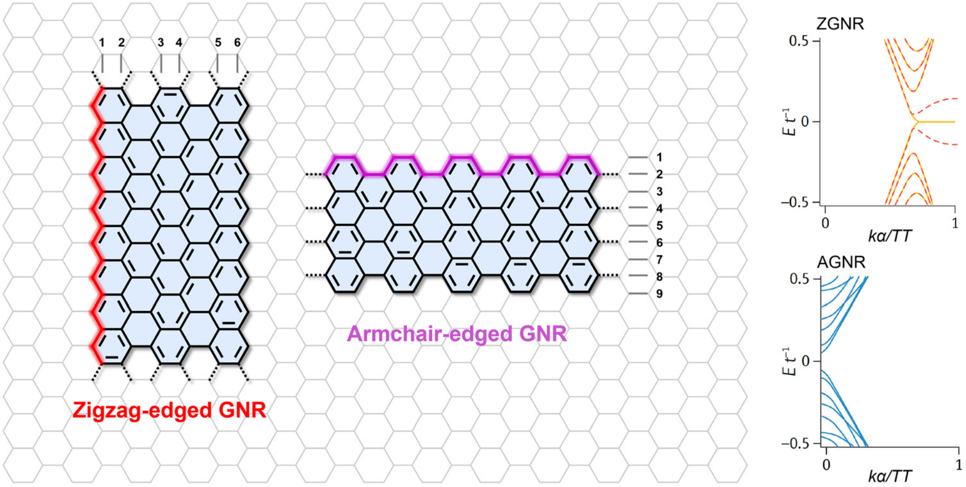

Fig. 1 The chemical structures and corresponding electronic structures of GNRs with zigzag and armchair edges.[10] The band structure of GNR is reproduced with permission from ref. 10. Copyright 2021, Springer Nature.

cove-zigzag hybrid edges can be constructed (Fig. 2).[62,93] By tuning the distribution of cove and zigzag structural units, the geometric configurations and electronic structures of the GNRs can be significantly altered. This highlights the broader potential of edge engineering: combining different edge types to create GNRs with novel hybrid-edge structures. For instance, the recently reported curved GNRs (cGNRs) incorporate cove, zigzag, and armchair edge structures simultaneously into the edges of the GNRs (Fig. 2).[70] While modulating the geometric structure of the GNRs, this design also has a significant impact on their band structure and carrier transport properties. Another important class is chiral-edged GNRs (chGNRs), formed by specifically combining zigzag and armchair segments (Fig. 2).[63,73,94,95] This chiral structure not only enables precise modulation of the electronic band structure through the control of the chiral angle but can also induce spin-polarized edge states in specific configurations. In addition, the intentional breaking of edge symmetry has enabled researchers to fabricate GNRs with asymmetric edge structures on both sides. A representative example is the Janus-type GNR (JGNR), which combines zigzag edges on one side with gulf edges on the other (Fig. 2).[45] This design breaks lattice symmetry, induces sublattice imbalance within the unit cell, and can lead to novel electronic behavior, such as spin-symmetry breaking.

Beyond conventional approaches such as width modulation and edge-structure engineering, precise backbone modification of GNRs represents a critical strategy for tailoring their properties.[76–79,96–105] For example, incorporating non-benzenoid rings (*e.g.*, five-, seven-, or eight-membered rings) disrupts the uniform π-conjugated network, introduces non-planarity, localized gap states, and can significantly alter the electronic bandgap. Moreover, the covalent fusion of two structurally distinct GNR segments enables the construction of intramolecular heterojunctions. The abrupt change in band alignment and local density of states at such an interface can give rise to built-in electric fields and modified quantum-confinement effects.[80,106]

Moreover, heteroatom doping at the edges or within the backbone provides an additional means to modulate the physicochemical properties of GNRs.[23,67,107–117] For instance, thiophene-derived monomers allow efficient sulfur doping *via* cyclodehydrogenation,[112,118,119] while nitrogen-containing heterocyclic units (*e.g.*, pyridine, pyrrole, pyrimidine, or pyrazine) permit precise control over the type and location of nitrogen incorporation.[120–122] These doping strategies not only tune the

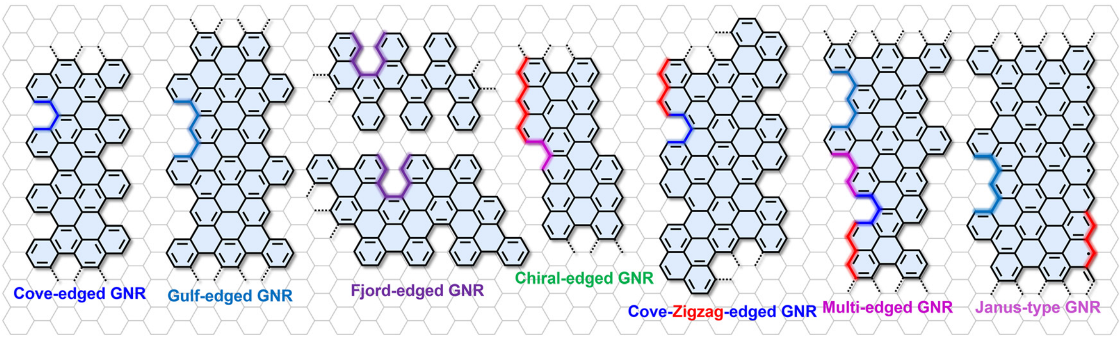

Fig. 2 Novel GNR edge structures achieved by introducing various types of carbon atom vacancies into AGNR and ZGNR edges.

band structure effectively, imparting n-type or p-type conductivity, but can also introduce localized spin states at specific sites,[120,123] thereby influencing chemical reactivity and structural stability.

As discussed above, the electronic band structure, magnetic properties, and carrier transport behavior of GNRs are strongly correlated with their geometric topology, including width, edge configuration, defect distribution, and heteroatom doping. This profound "structure-determines-property" relationship makes atomically precise and controllable synthesis a key prerequisite for realizing functional applications of GNRs. Currently, bottom-up synthesis is the mainstream strategy for achieving atomic-precision fabrication of GNRs, primarily comprising two synthetic routes: on-surface synthesis and solution-phase synthesis, each with distinct characteristics in terms of preparation condition, characterization methods, and compatibility with subsequent processing.[10,11,16,17,20,40,41,124]

On-surface synthesis is typically performed under ultra-high vacuum (UHV) conditions, where custom-designed organic precursors are deposited onto metal single-crystal substrates (*e.g.*, Au(111)) and subjected to thermally induced surface-catalyzed reactions (such as Ullmann coupling and cyclodehydrogenation) to achieve stepwise polymerization, ultimately forming the target GNRs on the substrate.[13,17,88,125,126] With atomic-level precision, this method is uniquely capable of synthesizing GNRs with reactive edges (*e.g.*, zigzag) and constructing complex systems like heterojunctions. It also permits *in-situ*, real-time characterization by scanning tunneling microscopy (STM) and non-contact atomic force microscopy (nc-AFM). However, the resulting products are generally immobilized on conductive substrates, making large-scale transfer challenging.[10,20,126,127] The synthesis is limited by surface diffusion and coupling efficiency, hindering the preparation of ultralong, continuous GNRs. Additionally, it relies on UHV conditions and single-crystal substrates, resulting in high costs and relatively low yields.

Solution-phase synthesis, on the other hand, is conducted in a liquid-phase environment.[16,60,69,128] It involves the stepwise construction of polymer precursors *via* coupling reactions (*e.g.*, Suzuki or Yamamoto) followed by solution-phase cyclodehydrogenation (*e.g.*, Scholl reaction) to form extended conjugated backbones, ultimately yielding GNRs. This approach generally yields GNRs that are solution-processable, suitable for large-scale techniques such as spin coating and printing, and enables detailed spectroscopic characterization and facile functionalization *via* substituent introduction.[25,42–44,60,67,70,72,75] However, controlling length uniformity remains challenging due to the broad polydispersity in polymerization degree, which hinders the production of uniform, ultralong GNRs.[129–137] Moreover, achieving single-dispersed GNRs in the solution phase remains challenging.[25,43,60,67] This is primarily due to the extensive conjugated structure of GNRs, which leads to strong intermolecular π–π interactions between GNRs. As a result, exfoliating and maintaining stable single-GNR dispersion in solution is particularly difficult. Even when dispersion is achieved through physical means, the isolated GNRs tend to rapidly reaggregate, driven by interfacial energy minimization, thereby severely compromising their solution processability and potential device integration.

In the following sections, we will discuss the relationship between synthesis strategies and electronic properties of GNRs, with particular emphasis on edge and backbone structures. Although several reviews have appeared in this field,[11,17,41,47,60,125–127] most have focused primarily on on-surface synthesis, while reviews addressing solution-phase approaches often concentrate on structural classification or solubility enhancement. To bridge these gaps, this review will integrate three key fronts—edge modulation, backbone engineering, and heterostructure construction—within a unified framework. By consolidating representative progress from recent years, this review aims to provide a chemistry-oriented reference for the rational design of functional GNRs, with relevance to nanoelectronic and emerging quantum device applications.

3. Chemical strategy for tailored edges in GNRs

The edge structure of GNRs stands out as one of their most distinctive features, not only determining their geometric topologies but also directly governing their electronic structures.[13,14,20,40,57,88] Therefore, the intrinsic properties of GNRs can be effectively modulated through the precise design of their edge configurations. This section focuses on recent breakthroughs in GNR edge structure design, centered around three key strategies: first, achieving controllable synthesis of GNRs with specific edge topologies by precisely designing the geometric structure of monomers; second, fine-tuning the local charge distribution and band structure through heteroatom doping (*e.g.*, nitrogen, boron, or sulfur) at the edges; and third, covalently functionalizing the GNR edges to enhance solution processability and directionally tailor their opto-electronic properties.

3.1 Edge structure

Edge configuration governs the bandgap and electronic properties of GNRs. While the basic electronic and magnetic behavior of conventional zigzag and armchair edges have been extensively reviewed,[11,17,40,41,124,138] this section focuses instead on recent synthetic advances in AGNRs and ZGNRs—including chiral-edged GNRs that combine both edge types. We will further highlight recent developments in designing GNRs with non-conventional edge architectures, such as cove, fjord, and hybrid edges, emphasizing their optical bandgaps, carrier mobility, solution processability, and emerging phenomena like spin-polarized states and topological boundary modes.

3.1.1 Recent advances in GNRs with conventional edge structures. For AGNRs, extensive previous work has primarily focused on the surface-assisted synthesis of AGNRs with different widths belonging to distinct families and has systematically characterized the correlation between representative widths and their electronic properties.[13,50–52,90] In 2020, Sato *et al.* synthesized a 17-AGNR on an Au(111) surface using a di-bromobenzene-based bianthryl derivative (**1**) as the precursor *via* a bottom-up strategy (Fig. 3a). The synthetic route follows the typical two-step surface reaction process. STM and nc-AFM characterizations directly confirmed its intact armchair-edged configuration and precise width of 17 carbon atoms.[54] More importantly, as a member of the $3p + 2$ family, the 17-AGNR exhibits an exceptionally narrow bandgap (experimentally determined to be 0.19 eV), setting a record among all bottom-up-synthesized AGNRs reported to date.[54] This distinctive narrow-bandgap characteristic arises from its specific width and edge topology, which significantly distinguishes it from AGNRs of other widths (*e.g.*, $N = 7, 9, 13$).

The on-surface synthesis of AGNRs typically relies on the catalytic activity of metal substrates. However, the strong electronic coupling between the metal substrate and the GNRs severely screens or disrupts their designed electronic structures and intrinsic properties, such as magnetic edge states.[88,139] Therefore, GNRs synthesized on metal substrates need to undergo complex transfer processes before they can be used for intrinsic property characterization or device fabrication. In 2020, Amsharov *et al.* proposed an innovative approach for the direct synthesis of atomically precise AGNRs on semiconducting metal oxide surfaces (Fig. 3b).[140] By designing a multifunctional precursor 10,10″-dibromo-1′,4′-difluoro-9,9′:10′,9″-teranthracene, DBDFTA (**2**), they successfully achieved a multi-step, controllable sequence of surface chemical reactions on the $TiO_2(011)$-(2 × 1) surface: intermolecular polycondensation driven by C–Br bond activation, followed by intramolecular cyclodefluorination triggered by C–F bond activation, and subsequent cyclodehydrogenation, ultimately constructing a finite-length 7-AGNR with well-defined zigzag terminal structures (Fig. 3b). STM/scanning tunneling spectroscopy (STS) confirmed the atomic precision of the synthesized GNR structures and revealed their unique electronic features.[140] This work breaks through the conventional reliance on metal-surface catalysis for GNR synthesis. The system exhibits extremely weak electronic coupling between the 7-AGNR and the substrate, thereby providing significant protection to the intrinsic spin-polarized edge states (zigzag end states),

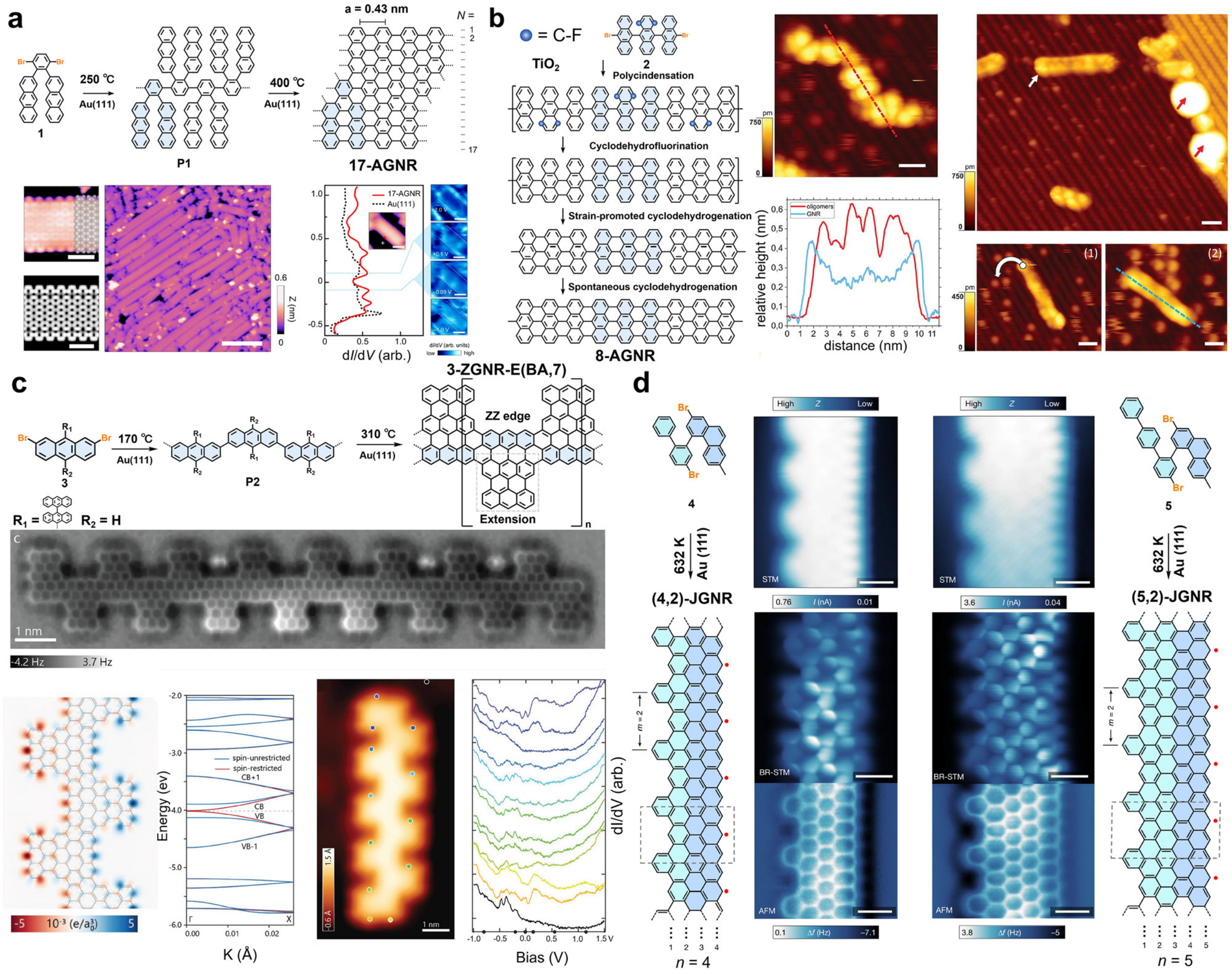

Fig. 3 (a) Bottom-up synthesis, corresponding STM topography, DFT-simulated images, and electronic state characterization of 17-AGNRs. Reprinted with permission from ref. 54. Copyright 2020, Springer Nature. (b) Schematic diagram of the gradual formation of GNR on the surface of metal oxides through multi-step reaction pathways and the process of transformation from oligoanthracenes to GNR characterized by STM. Reprinted with permission from ref. 140. Copyright 2020, American Association for the Advancement of Science. (c) On-surface synthesis, electronic structure, and spin density plot of edge-extended ZGNRs. Reprinted with permission from ref. 57. Copyright 2023, Wiley-VCH. (d) On-surface synthesis and structural characterization of the JGNRs. Reprinted with permission from ref. 45. Copyright 2025, Springer Nature.

whose quasiparticle gap (Δ_{ZZ} = 2.45 ± 0.10 eV) closely matches theoretical predictions for an isolated free-standing system.[140] Although the use of a non-metal substrate weakens the interaction between the GNR and the substrate, its low catalytic activity inhibits long-range molecular diffusion and further C–C coupling, which nevertheless results in quite short GNRs with this method. Later in 2023, Godlewski *et al.* reported a general method for the efficient synthesis of 7-AGNRs on the rutile $TiO_2(110)$-(1 × 1) surface *via* thermally induced intramolecular cyclodehydrogenation.[141] By integrating the well-established two-step process of surface-assisted Ullmann coupling polymerization (300 °C) and cyclodehydrogenation (400 °C), they successfully constructed 7-AGNRs on $TiO_2(110)$ for the first time using the precursor 10,10′-dibromo-9,9′-bianthryl. STM/STS combined with theoretical simulations confirmed the clear atomic configuration of the synthesized nanostructures, which are nevertheless quite short, along with weak electronic coupling between their occupied frontier orbitals and the substrate, demonstrating that this synthesis strategy effectively preserves the intrinsic electronic properties of the GNRs.[141]

Research on ZGNRs has seen relatively limited progress over the past five years. While their edge structures confer unique electronic and magnetic properties, the persistent challenge of achieving precise synthetic control has significantly hampered advancement. In 2023, Fasel *et al.* reported the surface synthesis of edge-extended ZGNRs based on a novel design motif using rationally designed monomer 2,7-dibromo-9,9′:10′,9″-teranthracene (**3**) (Fig. 3c),[57] which undergoes sequential dehalogenative polymerization and cyclodehydrogenation on an Au(111) surface, yielding a 3-ZGNR periodically fused with bianthrene edge-extension units (denoted as 3-ZGNR-E(BA,7)). nc-AFM directly visualizes the atomically precise structure, confirming the covalent attachment of the extension units to the zigzag edges (Fig. 3c). This edge-extended architecture not only introduces periodic topographic modifications along the zigzag periphery but also spatially shifts the spin-polarized edge states toward the outer boundary of the extensions, offering a new pathway to tailor magnetic and electronic properties.[57] Density functional theory (DFT) calculations indicate an open-shell ground state with pronounced spin polarization in the gas phase, while strong coupling to the metallic substrate quenches the spin polarization upon adsorption (Fig. 3c). The design motif is highly versatile; varying the R_1 and R_2 substituents allows the incorporation of diverse edge extensions and heteroatom doping, thereby opening a route toward structurally diverse and functionally tunable GNR heterojunctions and complex topological GNRs along the zigzag direction.[57]

A notable achievement is the synthesis of JGNRs with asymmetric zigzag-edge structures reported by Lu *et al.* in 2025 (Fig. 3d).[45] Based on Lieb's theorem and topological classification theory, this work introduces periodically arranged topological defect arrays of benzene rings on one side of ZGNRs, breaking structural symmetry and inducing lattice imbalance to achieve spin symmetry breaking. Notably, when the defect spacing is $m = 2$, the magnetic states at the defect edges are completely quenched, leaving only localized ferromagnetic edge states on the intact zigzag edges, thereby forming a one-dimensional ferromagnetic quantum spin chain.[45] They employed an innovative asymmetric Z-shaped precursor design, utilizing a multi-step synthetic strategy to separately construct two structural units: methylphenanthrene and oligophenyls of specific lengths, namely biphenyl or terphenyl. These units were then covalently linked *via* a key Suzuki coupling reaction, thereby customizing monomers 2-bromo-4-(4-bromo-[1,1′-biphenyl]-2-yl)-7-methylphenanthrene (**4**) and 2-bromo-4-(4-bromo-[1,1′:4′,1″-terphenyl]-2-yl)-7-methylphenanthrene (**5**), which are capable of independently regulating the edge configurations on both sides of the final GNRs. However, due to the structural asymmetry of the monomer, the yield of the target GNR structure is low, and the achievable ribbon length remains limited (with the largest portion centered around 15 nm for polymeric precursor). The synthesized JGNRs were directly examined by STM and nc-AFM, which confirmed the expected asymmetric edge morphology. STS further revealed that, in contrast to symmetric 5-ZGNRs, both types of JGNRs exhibit unique localized electronic states near the intact zigzag edge, with their ferromagnetic edge states preserved even on a metal substrate.[45]

In recent years, research on the on-surface synthesis of chGNRs with both zigzag and armchair edge structures has been steadily deepened.[73,94,142] Owing to their unique non-trivial edge configurations and tunable electronic structures, such GNRs exhibit significant potential in nanoelectronics and spintronics. Related studies have focused on molecular precursor design, regulation of on-surface reaction pathways, and characterization of chirality-dependent properties, thereby further expanding the structural diversity and property-tuning space of GNRs. In 2021, Pascual *et al.* reported the atomic-precision synthesis of a series of chGNRs with tunable chiral vectors (n,m) *via* designed molecular precursors (**6**, **7**, **8**, **9**) and on-surface reactions.[73] By varying bromination sites and the number of anthracene units in the precursors, they precisely controlled the width, chiral angle, and edge configuration of the resulting GNRs (Fig. 4a). For instance, adjusting the bromination site parameter a allowed access to distinct chiral configurations such as (3,1) and (2,3), characterized by alternating zigzag and armchair edge segments. The electronic and topological properties of these chGNRs were found to depend strongly on width and chirality (Fig. 4a).[73] With decreasing width, the system can transition from a metallic edge state to a symmetry-protected topological insulator, and further to a trivial insulator. Notably, the bandgap and spatial distribution of topological boundary states vary with chiral angle: for example, (3,1,8)-chGNR exhibits a narrow gap and end-localized topological states, while (3,2,8)-chGNR shows a wider gap (∼300 meV) and more confined end states.[73] Oteyza *et al.* successfully synthesized carbonyl (ketone)-functionalized chGNR (K-chGNRs) and their pristine counterparts (P-chGNRs) *via* precise molecular precursor design and on-surface synthesis strategies (Fig. 4b).[94] By controlling the presence and position of ketone groups in the precursors, and through post-synthetic surface reactions such as oxygen atom removal or addition, they successfully introduced π-radicals at specific sites in chGNRs, thereby constructing spin-active systems

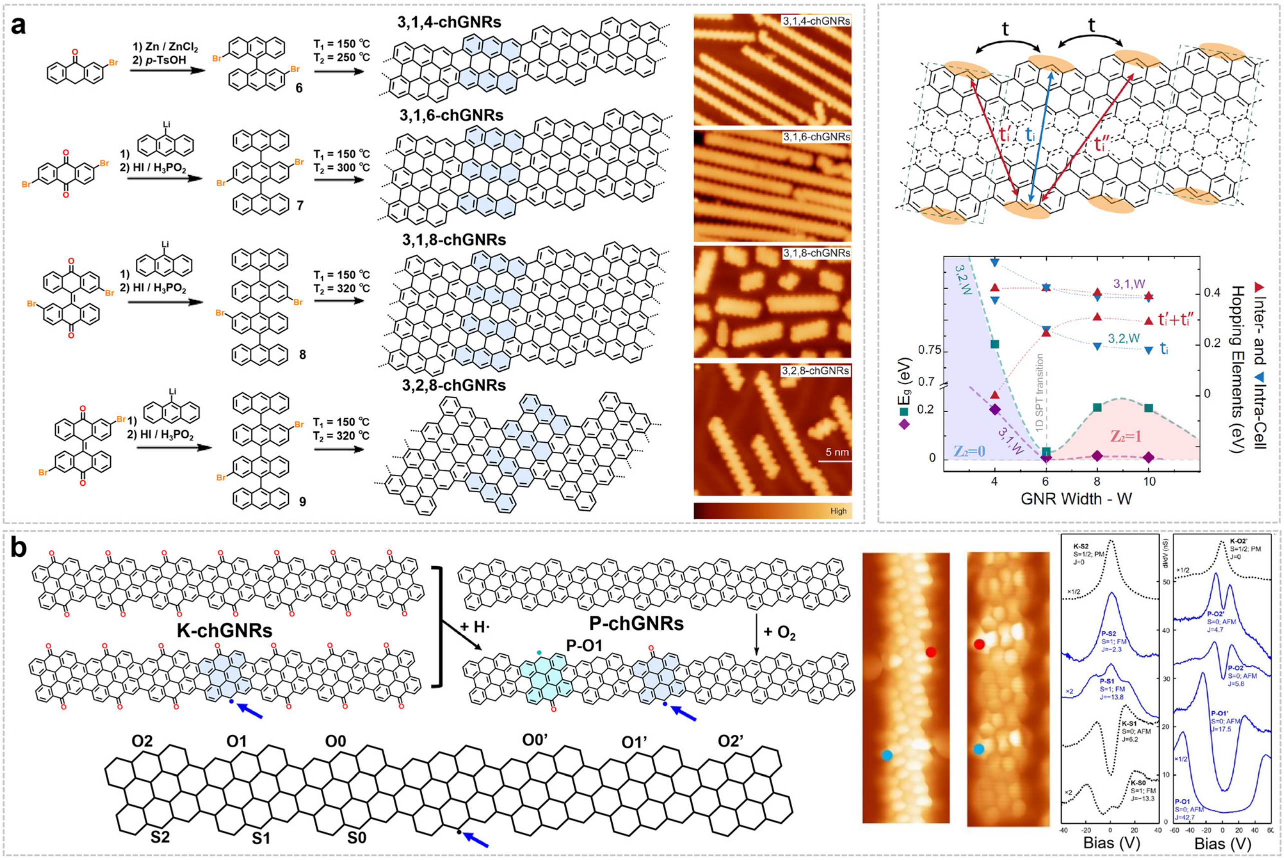

Fig. 4 (a) Synthetic strategy, STM characterization, and topological band structure simulation of chGNRs. Reprinted with permission from ref. 73. Copyright 2021, Springer Nature. (b) Schematic diagram of the magnetic chGNR fabrication process alongside BR-STM images and d*I*/d*V* spectra of radical pairs, revealing their spin-polarized states and magnetic coupling. Reprinted with permission from ref. 94. Copyright 2021, American Chemical Society.

with single radicals or tunable radical pairs. The research reveals that the magnetic interactions in these chGNRs depend not only on the relative positions of the radicals (same side *vs.* opposite side, spatial separation) but also critically on the chiral structure. For instance, in chirally asymmetric chGNRs, the spin density distribution exhibits distinct chirality-dependent extension, leading to significant variations in the exchange coupling strength depending on the relative chiral orientation of the radical pairs (Fig. 4b). Moreover, comparisons between K-chGNRs and P-chGNRs show that carbonyl functionalization not only substantially widens the bandgap but also confines the spatial extent of localized spin states, resulting in notably weaker exchange coupling for the same geometric arrangement of radicals compared to the pristine GNRs.[94]

3.1.2 Advances in GNRs with unconventional edge topologies. In addition to the aforementioned research advances on armchair, zigzag, and chGNRs, a series of GNRs with unconventional edge structures have been developed in recent years, including those with cove-edged, gulf-edged, fjord-edged, cove-zigzag-edged, and other hybrid edge architectures.[61–64,70–72,93] These structures are primarily synthesized *via* solution-based methods, and the resulting non-planarity enhances the solubility of these GNRs in common organic solvents, thereby enabling subsequent functionalization and device integration.

A cove-type edge structure can be constructed at the edge of ZGNRs by creating vacancies through the removal of specific carbon atoms. For example, starting from a zigzag configuration, eliminating a single carbon atom between two zigzag segments yields the GNR with a cove-type edge (Fig. 5a). In our early work, the monomer 11,11′-dibromo-5,5′-bischrysene (**10**), which was designed to form a cove-type edge structure, was synthesized and subsequently subjected to intermolecular Ullmann coupling followed by cyclodehydrogenation, leading to the first synthesis of GNRs with a cove-edge structure (CGNRs).[61] The most distinctive structural feature of these GNRs stems from their cove-edged geometry: the steric repulsion between adjacent C–H bonds in the [4] helicene unit along the edges forces the GNR backbone into a periodic torsional distortion, stabilizing a nonplanar ''up-down'' alternating conformation (Fig. 5b).[61] This structural characteristic not only endows the GNR with good solution processability but also directly leads to its relatively low intrinsic bandgap of approximately 1.70 eV, exhibiting unique electronic properties distinct from conventional armchair- or zigzag-edged GNRs.[61] However, the resulting CGNRs are quite short, as the on-surface synthesis tends to induce defect formation due to the generation of five-membered rings at the cove edges, which disrupts planarity on the surface.

In addition to solution-phase synthesis, GNRs with cove-edge structures can also be prepared *via* on-surface synthesis strategies.[71] However, this approach faces a key challenge: the intrinsically high reactivity and catalytic activity of metal substrates can promote both necessary cyclization and undesired side reactions. Specifically, the local curvature and strain at cove-edge sites may induce non-regioselective C–H activation and C–C bond formation under catalytic conditions, resulting in five-membered rings.[77] This non-ideal cyclization alters the intended edge structure, markedly affecting the band structure and causing the properties to deviate from theoretical design goals.

Moreover, GNRs with cove-edged segments can also be derived from armchair-edged structures (Fig. 5a). For example, in 2023, we reported the first solution synthesis of a pyrene-based curved GNR (PyGNR) featuring the cove edge structure (Fig. 5c).[64] This work employed a strategically designed tetrahydropyrene-based polyphenylene precursor, enabling a synergistic one-pot process that integrates oxidative dehydrogenation at the K-regions with Scholl cyclodehydrogenation to successfully construct the target GNR. Initially, A_2B_2-type Suzuki polymerization between a 3,7-dimethyloctyl-functionalized 1,4-diiodobenzene (**12**) and a 2,7-diborylated tetrahydropyrene (**11**) afforded a soluble, high-molecular-weight linear polymer (**P3**). Subsequently, a $FeCl_3$-mediated one-pot Scholl reaction simultaneously induced intramolecular cyclodehydrogenation and oxidative dehydrogenation at the tetrahydropyrene units, ultimately yielding the fully conjugated PyGNR. The obtained PyGNR exhibits distinct structural features that directly determine its exceptional properties: first, its repeating unit incorporates cove-type structures along the edges of a 9-AGNR, forming a unique edge topology where cove and armchair edges alternately coexist. Second, derived from its core double-[4]helicene structural motif, the entire GNR backbone adopts a non-planar, curved geometry (confirmed by the single-crystal structure of the model compound). These

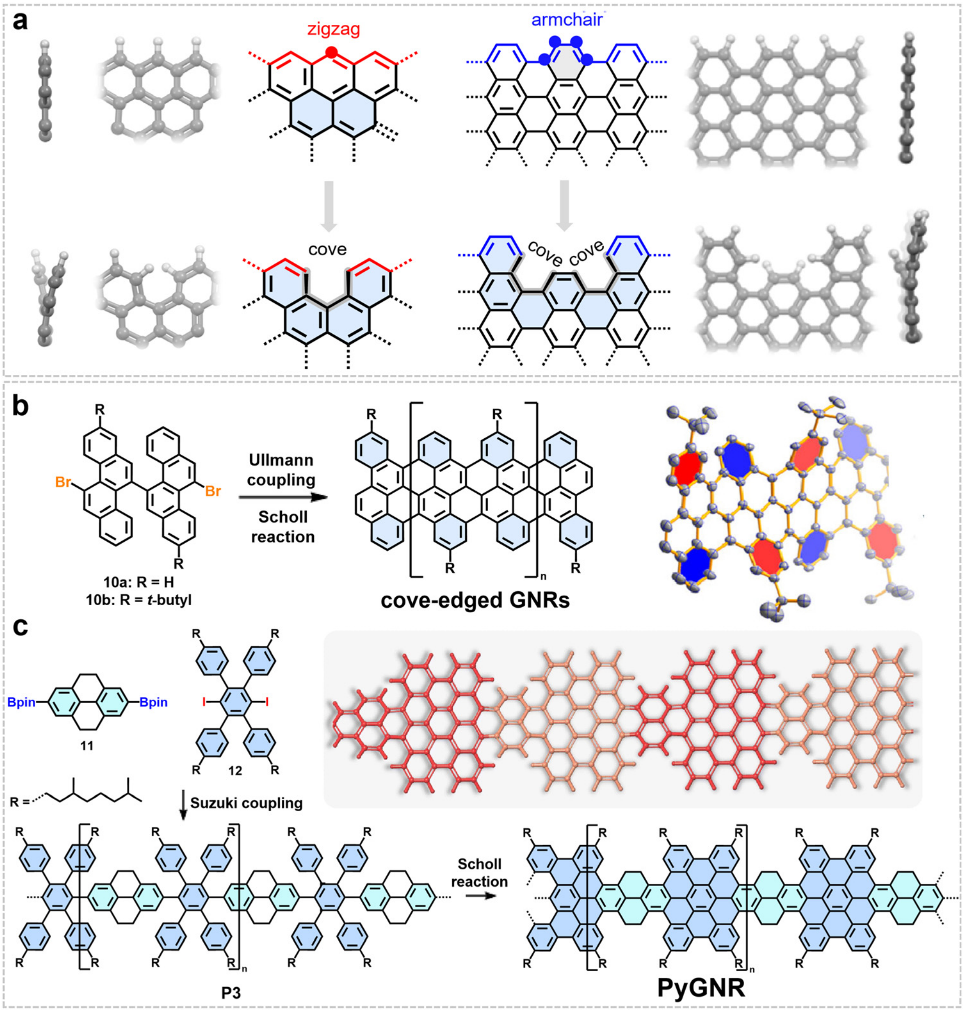

Fig. 5 (a) Schematic diagram illustrating the creation of cove-edged GNRs by introducing vacancies through the removal of specific carbon atoms from GNRs with zigzag or armchair edges. Reprinted with permission from ref. 61. Copyright 2015, American Chemical Society. (b) Structure of targeted cove-edged GNRs and their synthetic process, along with the corresponding single-crystal structure of the model molecule featuring alternating top-down edge structures. Reprinted with permission from ref. 61. Copyright 2015, American Chemical Society. (c) Schematic diagram of the synthetic process for PyGNR with cove and armchair edge structures, as well as the optimized geometry of PyGNR. Reprinted with permission from ref. 64. Copyright 2023, the Royal Society of Chemistry.

structural characteristics collectively endow PyGNR with a narrow optical bandgap of approximately 1.4 eV.[64]

By tuning the distribution of cove structural units along the edges, a series of GNRs with cove-zigzag hybrid edges can be obtained (Fig. 6a).[62] The electronic properties of these GNRs are predominantly governed by the periodic arrangement of the cove and zigzag segments, which enables a continuous transition from semiconducting to near-metallic behavior. Our group selected 6-CZGNR-(2,1) as a representative system and systematically characterized its optoelectronic properties (Fig. 6a).[62] Its synthesis hinges on the design and preparation of a structurally flexible, S-shaped phenanthrene-based key monomer: 1,4-bis(6-chloro-10-dodecylphenanthren-4-yl)benzene. Through Yamamoto coupling polymerization, this monomer yields a snake-like polymer precursor (**P4**), which subsequently undergoes efficient cyclodehydrogenation *via* the Scholl reaction to achieve the target GNR in solution (Fig. 6a). UV-Vis-NIR absorption spectroscopy revealed that 6-CZGNR-(2,1) exhibited a narrow optical bandgap of 0.99 eV, extending its absorption spectrum into the near-infrared region (Fig. 6a).[62] Theoretical calculations reveal that 6-CZGNR-(2,1) exhibits a low effective carrier mass ($m^* = 0.085\ m_0$, Fig. 6a). To experimentally probe its intrinsic charge transport properties without contact-resistance artifacts, time-resolved terahertz (THz) spectroscopy—a non-contact, optically triggered technique—was used to probe the intrinsic charge-carrier mobility (detailed description of time-resolved THz spectroscopy is provided in the SI).[67,74] This method measures the complex photoconductivity of GNR thin films (or GNR solution) under a weak THz field; the intrinsic mobility $\mu = e\tau/m^*$ is extracted *via* the Drude–Smith model, which also provides a backscattering parameter c (ranging from -1 to 0). The value of c reflects the degree of backscattering: $c = 0$ corresponds to pure Drude behavior (no backscattering), while $c = -1$ indicates complete backscattering. The direct current (DC) mobility is then given by $\mu_{\mathrm{DC}} = \mu(1 + c)$, thereby linking the intrinsic mobility to the experimentally relevant DC mobility under backscattering. Using this approach, thin films of 6-CZGNR-(2,1) exhibit an intrinsic mobility ($\mu = e\tau/m^*$) of up to 600 $\mathrm{cm^2\ V^{-1}\ s^{-1}}$ and μ_{DC} ($\mu_{\mathrm{DC}} = \mu(1 + c)$) of 18 $\mathrm{cm^2\ V^{-1}\ s^{-1}}$ in time-resolved THz spectroscopy measurements (Fig. 6a), which is among the highest mobilities reported for GNRs.[62]

Very recently, we showed that design principle of the cove-edge structure could be extended to the synthesis of cove-edged chiral GNRs (CcGNRs) (Fig. 6b).[63] This was achieved by incorporating cove structural motifs into the edges of pristine chiral GNRs while precisely controlling their chiral vector (n,m) or chiral angle (θ). We successfully synthesized two CcGNRs with distinct chiral vectors—specifically (4,2) and (6,2)—following a shared synthetic strategy. Both routes started from the same commercial starting material, 1-bromo-4-(*tert*-butyl)-2-iodobenzene. Through a sequence of precise coupling and cyclization reactions, two aromatic building blocks were constructed:

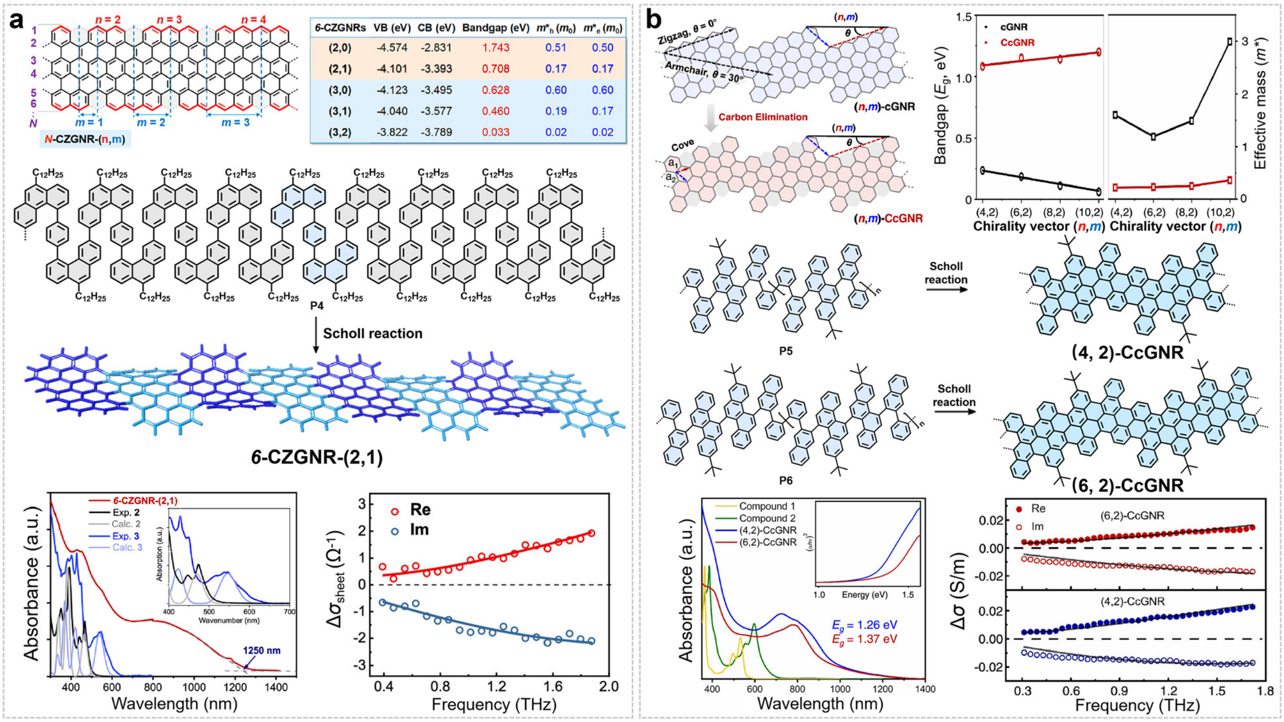

6-CZGNRs	VB (eV)	CB (eV)	Bandgap (eV)	m^*_h (m_0)	m^*_e (m_0)
(2,0)	-4.574	-2.831	1.743	0.51	0.50
(2,1)	-4.101	-3.393	0.708	0.17	0.17
(3,0)	-4.123	-3.495	0.628	0.60	0.60
(3,1)	-4.040	-3.577	0.460	0.19	0.17
(3,2)	-3.822	-3.789	0.033	0.02	0.02

Fig. 6 (a) Schematic illustration and calculated band structure of N-CZGNR-(n,m), along with synthetic routes for 6-CZGNR-(2,1), and their corresponding UV-Vis absorption spectra and frequency-resolved THz complex conductivity. Reprinted with permission from ref. 62. Copyright 2022, American Chemical Society. (b) Illustration of the transformation from pristine (n,m)-cGNRs to cove-edged chiral GNRs ((n,m)-CcGNRs) *via* periodic carbon elimination, including a comparison of their calculated bandgap and effective mass. The synthesis processes for the resulting (4,2)- and (6,2)-CcGNRs are also provided, accompanied by their respective UV-Vis absorption spectra and frequency-resolved THz complex conductivity. Reprinted with permission from ref. 63. Copyright 2024, American Chemical Society.

a chrysene-based fragment (for the (4,2)-type) and a bischrysene-based fragment (for the (6,2)-type). Each building block was then connected *via* Suzuki coupling to a custom-synthesized naphthylboronic acid derivative, yielding two structurally distinct linear oligophenylene precursors. These oligomeric species served as the respective monomers and were separately polymerized *via* nickel-mediated Yamamoto coupling, affording high-molecular-weight linear polymer precursors: **P5** (corresponding to (4,2)-CcGNR) and **P6** (corresponding to (6,2)-CcGNR). Finally, cyclodehydrogenation *via* the Scholl reaction furnished the target CcGNRs.[63] Experimental results confirm that (4,2)-CcGNR (chiral angle 19.1°) exhibits a relatively narrow optical bandgap (1.26 eV) and a higher μ_{DC} ($\mu_{\mathrm{DC}} = \mu(1 + c)$) ($\sim 14\ \mathrm{cm^2\ V^{-1}\ s^{-1}}$), whereas (6,2)-CcGNR (chiral angle 13.9°) has a wider bandgap (1.37 eV) and lower μ_{DC} ($\sim 8\ \mathrm{cm^2\ V^{-1}\ s^{-1}}$) (Fig. 6b). This difference originates from the variations in π-electron delocalization induced by the cove edges and the differing slopes of the band-edge dispersion: structures with larger chiral angles possess more extended electron wavefunctions and lower carrier effective masses, thereby enhancing charge transport capabilities.[63]

In addition to cove-type edges, precision GNRs with other complex non-planar edge topologies have emerged as attractive synthetic targets. A notable example is the work reported in 2021 by Müllen, Narita, and colleagues, who developed an efficient solution-based strategy for synthesizing nonplanar GNRs (FGNR) with fjord edges (Fig. 7a).[74] The successful synthesis of the novel FGNR was guided by two key model compounds, triphenanthro-fused teropyrene and pentaphenanthro-fused quateropyrene. Equipped with bulky *tert*-butyl groups, these models ensured solubility and, crucially, directed regioselective Scholl cyclodehydrogenation.[74] This steric control enabled the asymmetric integration of [5]helicene units, preventing planarization and inducing helical twists. X-ray crystallography confirmed the nonplanar, helically distorted conformations of model compounds, with model compound 2 showing end-to-end twists of 83° and 50° (Fig. 7a). The presence of both *M* and *P* enantiomers underscored the chiral nature imparted by the fjord-edge topology.[74] Building on this, starting from a functionalized *o*-terphenyl monomer (**13**), they prepared a linear poly(*p*-phenylene) precursor (**P7**) *via* AB-type Suzuki polymerization, followed by a regioselective Scholl reaction to ultimately construct the FGNR. Spectroscopic and mass spectrometric analyses confirmed the successful formation of the fjord-edge structure and a high cyclodehydrogenation efficiency of up to 97%. The resulting FGNR exhibited an absorption maximum at 569 nm, with an estimated optical bandgap of approximately 1.99 eV (Fig. 7a). Time-resolved THz spectroscopy revealed an intrinsic charge carrier mobility ($\mu = e\tau/m^*$) of around $100\ \mathrm{cm^2\ V^{-1}\ s^{-1}}$, demonstrating excellent charge transport properties.[74]

Recently, multi-edged GNRs incorporating more than two types of edge structures have also been developed. In 2020, we successfully synthesized a curved GNR with combined edge structures of cove, zigzag and armchair (Fig. 7b).[70] Using 1,8-bis(2-bromophenyl)benzo[*k*]tetraphene (**14**) as the monomer, a dodecylphenyl-substituted poly(diphenylbenzo[*k*]tetraphene) precursor polymer (**P8**) was constructed *via* AA-type Yamamoto polymerization. Subsequent cyclodehydrogenation yielded a curved GNR (cGNR) with a width of 0.7 nm (Fig. 7b). Single-crystal analysis of the corresponding model compounds, which incorporate double [4]helicene units, confirmed the inherent curvature of the structure (Fig. 7b).[70] This nonplanar geometry effectively suppresses inter-ribbon π–π stacking, as evidenced by solid-state ^{1}H–^{1}H DQ–SQ NMR spectroscopy, which shows narrowed autocorrelation signals for aromatic protons. Consequently, the cGNR demonstrates excellent dispersibility in common organic solvents such as chloroform and tetrahydrofuran, mild sonication enables the formation of green stable dispersion of the cGNR with a high concentration of $0.1\ \mathrm{mg\ mL^{-1}}$ in chloroform. Spectroscopic characterization reveals a strong absorption peak in the near-infrared region at 850 nm, corresponding to a narrow optical bandgap of 1.22 eV (Fig. 7b).[70] Furthermore, THz spectroscopy indicates a long charge-carrier scattering time of ∼60 fs and a high intrinsic carrier mobility ($\mu = e\tau/m^*$) of $\sim 600\ \mathrm{cm^2\ V^{-1}\ s^{-1}}$ (Fig. 7b).[70] Later in 2022, our group further reported a curved GNR (cMGNR) with a hybrid edge structure comprising cove-type, armchair, and gulf-type edges (Fig. 7c).[72] The synthesis involves an efficient A_2B_2-type Diels–Alder polymerization between a diethynyl-substituted prefused bichrysene monomer (**15**) and a dicyclopenta[*e*,*l*]pyrene-5,11-dione derivative (**16**) followed by $FeCl_3$-mediated oxidative cyclodehydrogenation of the obtained polyarylenes. The resultant cMGNR has an average length of 71 nm, as estimated by GPC analysis of the corresponding precursor polymer, which is notably longer than other reported curved GNRs. Spectroscopic and theoretical studies indicate that cMGNR exhibits a relatively narrow optical bandgap (1.61 eV) and a μ_{DC} ($\mu_{\mathrm{DC}} = \mu(1 + c)$) of approximately $2\ \mathrm{cm^2\ V^{-1}\ s^{-1}}$, which is lower than that of other reported curved GNRs (Fig. 7c). The relatively low mobility is mainly attributed to a larger effective carrier mass and a flat dispersion in the band structure.[72]

3.2 Edge doping with heteroatoms

The incorporation of heteroatoms (*e.g.*, sulfur, nitrogen, and boron) into GNRs is an important strategy for modulating their intrinsic properties, enabling significant regulation of key physicochemical characteristics, including electronic structure, bandgap, and charge-transport behavior.[117,143–149] Depending on the location of the heteroatoms within the GNR structure, doping strategies can be broadly classified into edge doping and backbone doping. Among these, edge doping is generally more synthetically feasible and straightforward, primarily owing to its modular ‘‘post-functionalization’’ approach: during monomer construction, one only needs to introduce heteroatom-containing functional groups or heterocycles onto the periphery of an all-carbon backbone *via* coupling reactions, followed by cyclodehydrogenation to precisely incorporate the heteroatoms at the GNR edges.[107,109,111,120,121,143,145,150] Since the first report of sulfur-doped GNRs synthesized by Ueda and coworkers in 2012,[118] extensive research has focused on this more controllable edge-doping strategy *via* the on-surface method. By designing different heterocyclic units and tuning the doping sites, this field has achieved systematic control over the band structure and carrier type of GNRs.

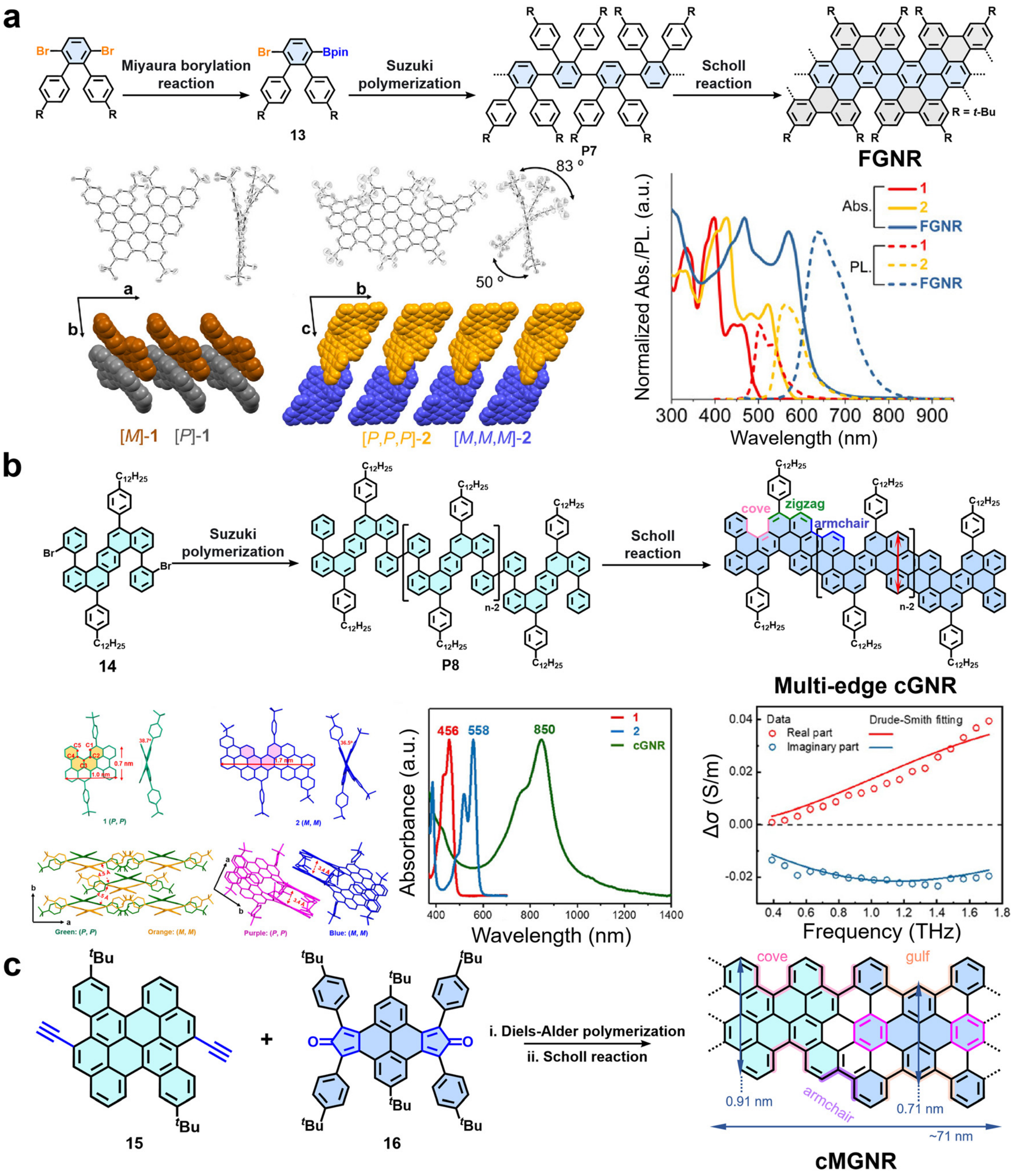

Fig. 7 (a) Schematic illustration of the synthesis of FGNR, crystal structures of model compound, as well as UV-vis-NIR and PL spectra of the model compound and FGNR. Reprinted with permission from ref. 74. Copyright 2021, American Chemical Society. (b) Synthetic route toward cGNR and UV-vis-NIR absorption spectra of the cGNR and the frequency-resolved THz complex conductivity. Reprinted with permission from ref. 70. Copyright 2020, American Chemical Society. (c) Synthetic route to the curved multi-edged GNR (cMGNR), UV-vis-NIR absorption spectra, and frequency-resolved terahertz conductivity of cMGNR.

In 2016, Crommie *et al.* first synthesized sulfur-edge-doped GNRs (S-13-AGNRs) *via* an on-surface synthesis method.[112] This was achieved by designing a monomer (**17**) based on 10,10′-dibromo-9,9′-bianthracene and introducing (2-phenyl)thiophene units through Suzuki coupling (Fig. 8a). The sulfur atoms are precisely incorporated as thiophene rings at the edges, with their lone-pair electrons fully conjugated into the π-system. This doping does not rigidly shift the bands but widens the energy spacing between the conduction and valence-bands, highlighting strong S–C orbital hybridization. Subsequently in 2017, our group and collaborators achieved on-surface synthesis of sulfur-doped chevron-type GNRs using a tailored sulfur-containing oligophenylene monomer (**18**) (Fig. 8b). When deposited on Au(111), the monomer adopts three isomeric configurations due to restricted thienyl-ring rotation. Thermal activation then triggers debromination, polymerization, and cyclodehydrogenation, yielding fully conjugated S-GNRs. The varied cyclization sites (α-C or β-C) of the thienyl rings generate multiple constitutional isomers (Fig. 8b),

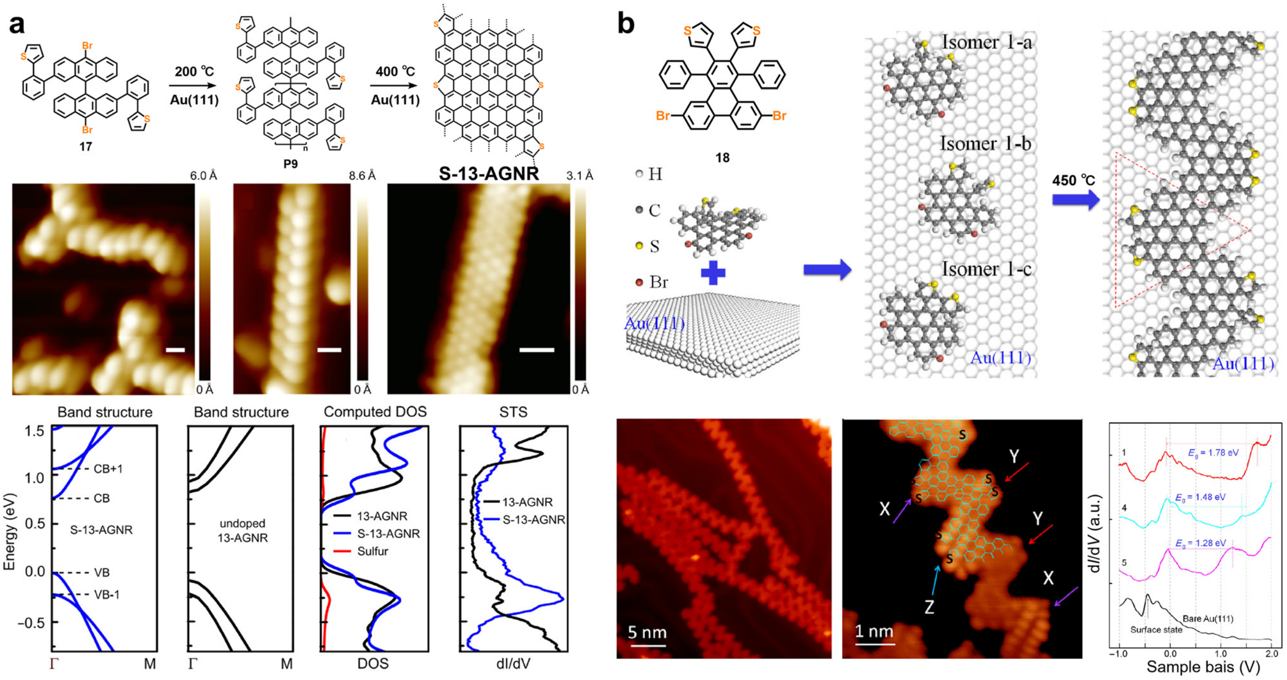

Fig. 8 (a) Reaction scheme, STM characterization, and electronic structure analysis (computed band structures and experimental dI/dV spectra) for S-13-AGNRs in comparison with pristine 13-AGNRs. Reprinted with permission from ref. 112. Copyright 2016, American Chemical Society. (b) STM images and electronic structures for S-GNRs fabricated *via* a bottom-up approach, in which the rotation of thienyl rings gives rise to distinct isomers. Reprinted with permission from ref. 110. Copyright 2017, Tsinghua University Press.

leading to a continuous bandgap variation from 1.28 eV to 1.87 eV within individual ribbons, as confirmed by STM/STS (Fig. 8b).[112]

In contrast to the orbital-coupling mechanism of sulfur, nitrogen doping exhibits a richer and more diverse range of regulatory dimensions, with effects that depend strongly on the doping sites and chemical bonding modes.[122] In AGNRs, introducing nitrogen atoms in different bonding forms—such as edge pyridinic nitrogen or graphitic nitrogen within the backbone (forming C–N or N–N bonds)—enables fine-tuning of the electronic structure.[122] In 2022, *via* an on-surface synthesis strategy, Cai *et al.* successfully fabricated 9-atom-wide nitrogen-doped AGNRs (N-AGNRs) with multiple nitrogen-doping sites, systematically investigating the regulation of their electronic structures by different doping configurations (Fig. 9a).[122] The study employed 3,3′-(3,6-diiodo-1,2-phenylene)dipyridine as the monomer (**19**). By leveraging its controllable adsorption and reaction on an

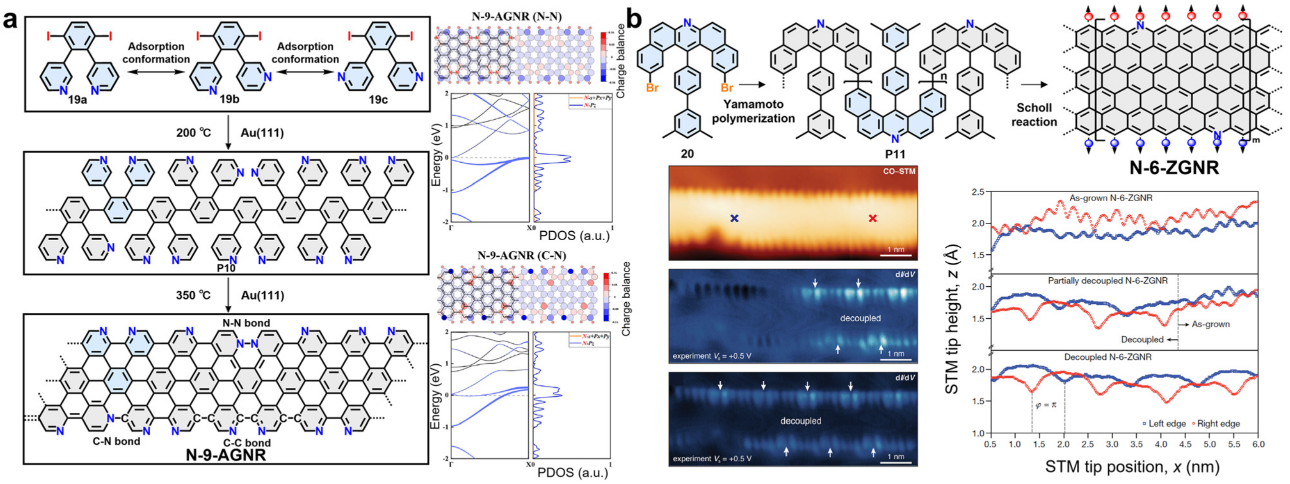

Fig. 9 (a) Schematic diagram of the synthetic process of N-9-AGNRs containing three different covalent bonds and calculated electronic structures and charge distributions of N-9-AGNRs. Reprinted with permission from ref. 122. Copyright 2022, Wiley-VCH. (b) Bottom-up synthesis of N-6-ZGNRs and subsequent analysis of their electronic properties, featuring tip-induced decoupling of magnetic edge states from the Au surface. Reprinted with permission from ref. 56. Copyright 2021, Springer Nature.

Au(111) surface, polymerization and dehydrogenative cyclization were achieved through a two-step annealing process. Due to the conformational flexibility of the precursor, three distinct covalent bond-forming pathways (C–N and N–N coupling) were accessible during cyclization, resulting in GNR segments containing three different types of nitrogen-doping sites (pyridinic nitrogen and graphitic nitrogen). Studies have shown that when nitrogen exists solely as edge pyridinic nitrogen, its role resembles that of hydrogenated carbon atoms, only slightly increasing the bandgap of N-9-AGNR compared to pristine 9-AGNR, while the GNR retains its semiconducting properties. However, if nitrogen is incorporated as graphitic nitrogen within the carbon backbone, its additional electron relative to carbon introduces defect states near the Fermi level, leading to significant band-structure reconstruction. Consequently, N-9-AGNR with C–N bonds and N-9-AGNR with N–N bonds exhibit metallic characteristics (Fig. 9a).[122]

Constructing a nitrogen-atom superlattice along the zigzag edges of ZGNRs can thermodynamically stabilize the highly reactive zigzag edges, thereby enabling the protection, decoupling, and direct observation of their intrinsic magnetic ordering (Fig. 9b).[56] In 2021, Fischer *et al.* employed U-shaped dibenzoacridine (**20**) as the monomer, in which nitrogen-doping sites and bromination sites were pre-designed, and successfully prepared N-6-ZGNR based on the on-surface synthesis strategy (Fig. 9b). This isoelectronic doping largely preserves the ferromagnetic ordering along the edges and the antiferromagnetically coupled spin configuration across the width. Using a scanning probe microscopy (SPM) tip-induced decoupling protocol, they applied a local bias voltage sweep over the N-6-ZGNR, which successfully disrupted the strong π-bonding hybridization between the ribbon's edge states and the Au(111) metal substrate (Fig. 9b). This allowed the GNR to relax into a less strained, lower-energy adsorption geometry, effectively suppressing substrate-induced interference with the electronic edge states. In this decoupled state, STS directly revealed that the large effective exchange field (approximately 850 T) generated by the ferromagnetically ordered zigzag edges induces a pronounced spin splitting of the flat bands arising from the nitrogen lone-pair electrons. The observed spin splitting is about 100 meV, giving rise to two distinct characteristic energy levels: the upper nitrogen flat band at approximately −2.60 V and the lower nitrogen flat band at approximately −2.70 V. These findings provide direct experimental evidence for the intrinsic edge magnetic order in ZGNRs.[56]

In addition to single-heteroatom doping at the edges of GNRs, multi-heteroatom co-doping strategies have been developed in recent years. By synergistically introducing different types of heteroatoms into the GNR edges, enhanced control over the electrical, optical, and transport properties of GNRs can be achieved.[108,109] In 2020, our group reported a strategy of incorporating nitrogen–boron–nitrogen (NBN) units into the edges of GNRs (Fig. 10a).[109] This approach greatly enhances the chemical stability of ZGNRs by preventing edge degradation or fusion, while simultaneously tuning their band structure through an isoelectronic substitution effect (Fig. 10a). We designed and synthesized two U-shaped molecular precursors. Their synthetic route started with a biphenyl derivative, in which a key Suzuki coupling reaction introduced iodinated phenyl rings, followed by reduction, ring-closure, and other steps. Ultimately, the core NBN-dibenzophenalene unit (**21**, **22**) was efficiently constructed by reacting the intermediate with boron trichloride in *ortho*-dichlorobenzene. Subsequently, using on-surface chemistry methods, structurally well-defined NBN-ZGNR1 and NBN-ZGNR2 were obtained (Fig. 10a). Comparing to pristine carbon ZGNRs with bandgaps of 0.27–0.52 eV, the bandgaps of NBN-ZGNRs are notably larger (1.50 eV for NBN-ZGNR1 and 0.90 eV for NBN-ZGNR2).[109] Furthermore, NBN edges possess unique chemical tunability.[151] Theoretical calculations indicate that single-electron oxidation of the NBN unit to form a radical cation can further tune the GNR into a gapless metallic state, enabling dynamic modulation of the electronic structure. Studies also show that even under the conditions of a silicon-intercalated buffer layer, NBN-ZGNRs retain their edge states, demonstrating that this doping not only improves edge stability but also preserves the detectability of their intrinsic electronic properties.[109]

In addition to nitrogen doping (or nitrogen–boron co-doping) and sulfur doping, the introduction of oxygen–boron–oxygen (OBO) heteroatomic motifs at the edges of GNRs has also attracted considerable research interest. For instance, Narita and Müllen *et al.* successfully prepared chGNRs (specifically (4,1)-GNRs) containing OBO units at their edges (Fig. 10b).[111] Starting from the molecular precursor 6,16-dibromo-9,10,19,20-tetraoxa-9*a*,19*a*-diboratetrabenzo[*a*,*f*,*j*,*o*]perylene (**23**), OBO-doped chiral (4,1)-GNRs were successfully synthesized on a surface. STS and theoretical calculations revealed that the introduction of the OBO units significantly modulates the electronic structure of the GNRs. Compared with pristine all-carbon (4,1)-GNRs (bandgap ≈ 0.50 eV), OBO doping widens the bandgap to about 1.50 eV. This increase is primarily attributed to the weak conjugation between the p-orbitals of the OBO segment and the extended π-system of the GNR carbon backbone.[111] However, compared to a similar GNR completely lacking OBO units (bandgap ≈ 1.90 eV), the weak conjugation still reduces the gap by approximately 0.40 eV. The experimental STS bandgap was measured to be around 3.33 eV, which aligns well with the GW approximation calculation result (2.96 eV) after image-charge correction. Notably, the incorporation of OBO units at the GNR edges also enables their lateral self-assembly through intermolecular O···H interactions (Fig. 10b).[111]

Heteroatom-doped GNRs can also be synthesized *via* solution-phase or solid-phase approaches.[107,121,150] However, compared with strategies for preparing all-carbon GNRs *via* conventional Scholl reactions, the synthetic pathways for such doped systems differ. The main challenge lies in the chemical compatibility of many heteroatom-containing precursor molecules under typical Scholl reaction conditions, such as strong Lewis acid or oxidant-driven aromatization/cyclization systems (*e.g.*, $FeCl_3$, DDQ/CF_3SO_3H). Heteroatom functional groups may undergo uncontrolled side reactions (*e.g.*, over-oxidation, elimination, or rearrangement) in strongly acidic or oxidizing environments, leading to degradation of the precursors or the formation of unintended structures. This in turn compromises the chemical precision and

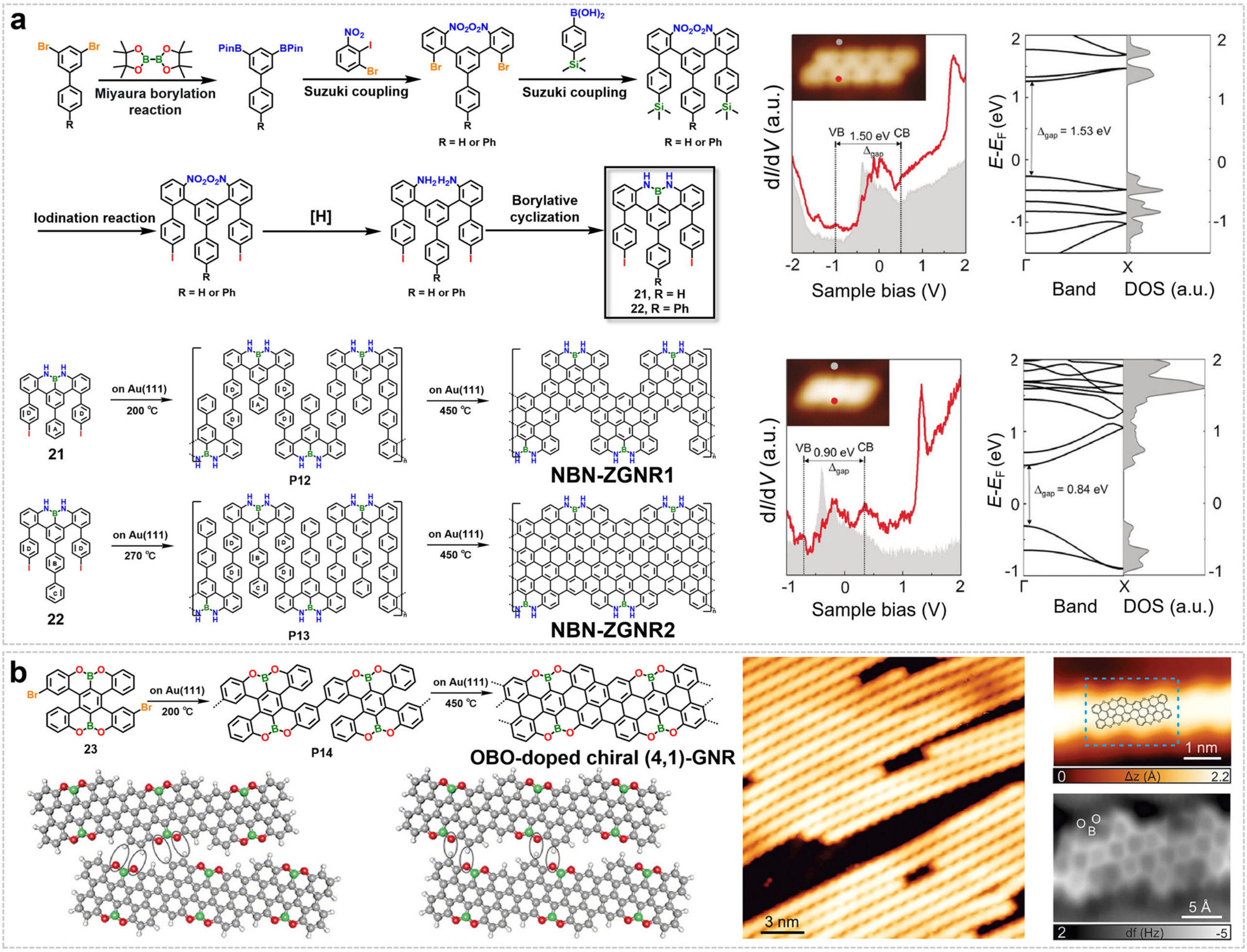

Fig. 10 (a) Synthesis of NBN-doped ZGNRs (NBN-ZGNR1 and NBN-ZGNR2) from designed precursors (M1, M2) and their electronic characterization through STS and band structure calculations. Reprinted with permission from ref. 109. Copyright 2020, Wiley-VCH. (b) Synthesis, STM characterization, and DFT modeling of inter-ribbon interactions in OBO-doped chiral (4,1)-GNRs. Reprinted with permission from ref. 111. Copyright 2018, American Chemical Society.

structural regularity of the resulting GNRs. Based on a solution-phase synthetic strategy employing the photochemical cyclodehydrochlorination (CDHC) reaction, Morin *et al.* successfully prepared two narrow GNRs with thiophene-edged functionalization (*p*T-GNR and *o*T-GNR).[119] The core of the synthetic route lies in the design and synthesis of polychlorinated poly(*p*-phenylene) copolymer precursors (**P15**, **P16**), in which thiophene units were precisely introduced into the monomer structure *via* Suzuki coupling (Fig. 11a). Under mild, metal-free, and oxidant-free photochemical conditions, regioselective CDHC efficiently achieved ''ladder-type'' aromatization, resulting in structurally well-defined GNRs (Fig. 11a). The uniqueness of these GNR structures is reflected in several aspects: Firstly, the arrangement of thiophene units at the edges (*ortho* or *para*) directly determines the symmetry of the GNRs. *o*T-GNR exhibits lateral asymmetry and possesses a permanent dipole moment, offering potential for modulating solid-state packing behavior. Secondly, combined with model compounds and DFT calculations, it is confirmed that both GNRs adopt highly contorted conformations. Among them, *p*T-GNR demonstrates enhanced structural rigidity due to steric congestion in the ''H-type'' contorted region of the thiophene units. Furthermore, spectroscopic characterization reveals that the incorporation of thiophene not only modulates the band structure of the GNRs (*p*T-GNR exhibits a bandgap of 2.61 eV, lower than that of *o*T-GNR at 2.91 eV) but also leads to highly consistent spectra in both solution and solid state, indicating weak π–π interactions and strong backbone rigidity (Fig. 11a).[119]

In 2018, Dong *et al.* proposed a modular synthetic strategy for bandgap engineering of 6-AGNRs (Fig. 11b).[107] The core of this method involves two key steps: first, controlled alternating copolymerization of designed triaryl monomers (**25**) and 1,4-diboronate-substituted aryl monomers (**24**, **26**, **27**) *via* Suzuki cross-coupling polymerization to construct well-defined linear poly(*p*-phenylene) precursors (**P17**, **P18**); subsequently, efficient aromatization of the precursors is achieved through regioselective cyclodehydrogenation under mild conditions using a DDQ/TfOH system, yielding structurally intact 6-AGNRs (Fig. 11b). The prominent advantage of this strategy lies in the modularity and flexibility of monomer design. By selectively introducing

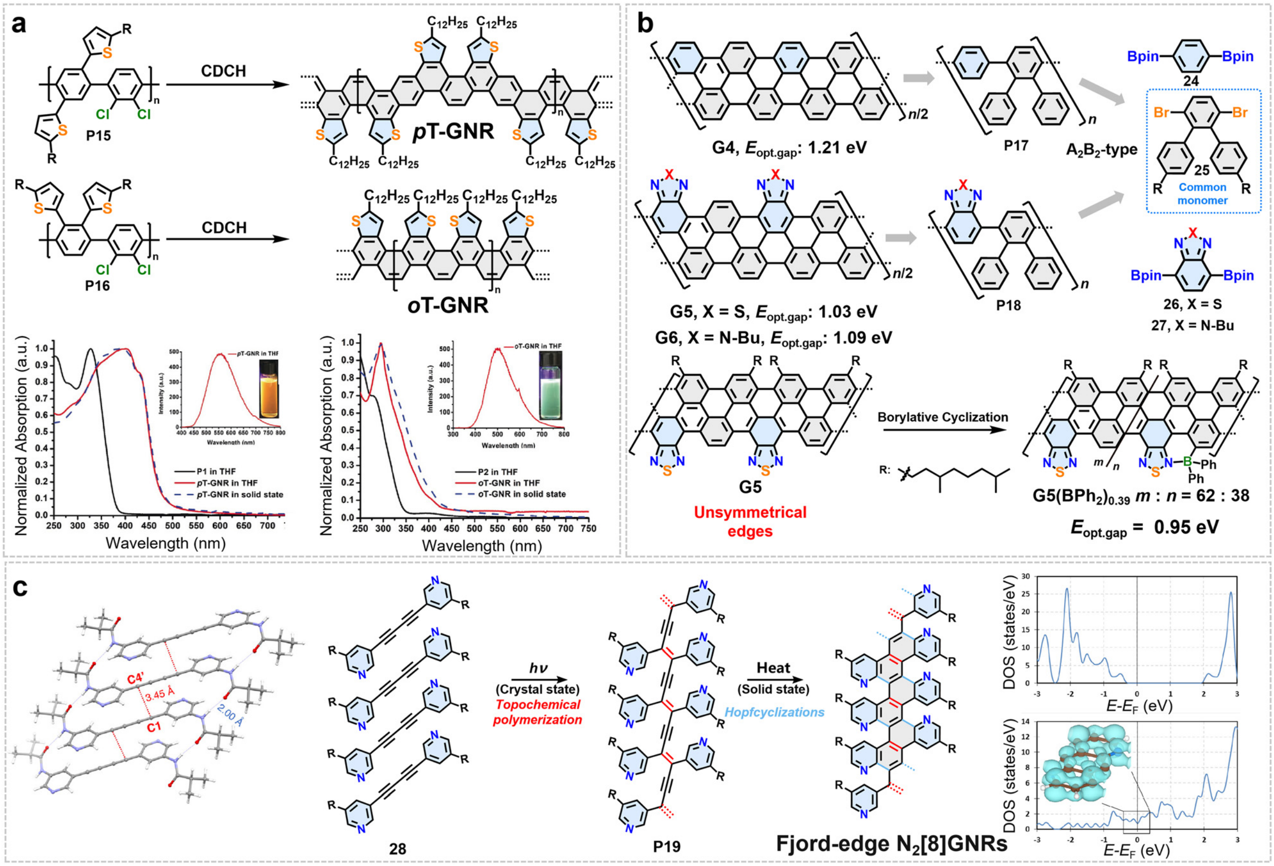

Fig. 11 (a) Synthesis and structures of *p*T-GNR and *o*T-GNR containing thiophene units, and their absorption/PL spectra in both solution and solid state. Reprinted with permission from ref. 119. Copyright 2018, Wiley-VCH. (b) Modular synthesis and heterocyclic edge functionalization for band-gap engineering of AGNRs. (c) Synthesis and electronic structure of fjord-edge N$_2$[8]GNRs: solid-state topochemical polymerization leading to cyclization-aromatization, monomer packing, and DOS for partially and fully cyclized structures. Reprinted with permission from ref. 121. Copyright 2020, American Chemical Society.

heteroaromatic units such as benzothiadiazole or benzotriazole at the edges, the electronic structure of the resulting 6-AGNRs can be directly modulated, leading to a significant reduction in bandgap. Moreover, this approach enables the construction of GNRs with unsymmetrical edge structures, which gives rise to an asymmetric electron density distribution across the ribbon. Experimental results show that the pristine 6-AGNR exhibits a bandgap of 1.21 eV, which decreases to 1.09 eV upon benzotriazole modification and further reduces to 1.03 eV with benzothiadiazole modification (Fig. 11b).[107] This trend in bandgap variation closely resembles the energy-level modulation behavior observed in donor–acceptor alternating conjugated polymers, indicating that edge heterocycle incorporation is an effective approach for tuning the electronic energy levels of GNRs. Furthermore, due to the electron density polarization induced by the asymmetric heterocyclic edges, the electron distribution in the GNRs is significantly skewed toward the heteroatom-containing side. This structural characteristic also creates opportunities for further functionalization. For example, precise introduction of boron atoms into the benzothiadiazole edge *via* C–H borylation allows for an additional reduction of the bandgap to 0.95 eV (Fig. 11b).[107]

In 2020, Rubin *et al.* reported the GNR synthesis strategy based on crystalline-state topochemical photopolymerization, enabling precise construction of site-specific nitrogen doping (Fig. 11c).[121] Using dipyridyl diyne (**28**) as the monomers, this method involves photochemically induced topochemical polymerization in the crystalline state to form polydiacetylene intermediates (**P19**), followed by thermal Hopf cyclization and aromatization under mild conditions, successfully yielding nitrogen-doped [8]-GNRs with a fjord-edge structure (Fig. 11c). Comprehensive characterization confirmed the structural precision of the GNRs and the chemical environment of the nitrogen doping sites. Theoretical calculations further revealed that these GNRs exhibit distinctive bonding topologies and electronic properties: the partially cyclized fjord-edged GNR behaves as a semiconductor with a bandgap of 2.04 eV, whereas the fully cyclized AGNR displays metallic character (Fig. 11c).[121]

3.3 Chemical functionalization on the edges

Covalent functionalization of GNR edges, achieved by incorporating functional units into monomers or substituting edge hydrogens with specific groups (*e.g.*, halogens, alkoxy, cyano, or imide rings), offers a versatile strategy for finely tuning their electronic structure,[152–155] and also importantly, improving the solubility of GNRs in organic solvents *via* introducing steric or polymeric side chains.[42,44,60,68,75] This approach thus enables the solution-processability of GNRs for opto-electronic studies and potential device integrations.

3.3.1 Edge substitution of GNRs.

Edge chlorination represents a typical edge modification strategy that precisely introduces chlorine atoms into the edges of GNRs through electrophilic substitution reactions while maintaining structural integrity.[156] In our previous studies, we developed an edge chlorination method employing CCl_4 as the solvent, iodine chloride as the chlorinating agent, and $AlCl_3$ as the catalyst. This method, performed at 80 °C, was successfully applied to solution-phase synthesized GNRs. By selectively substituting edge hydrogen atoms or *tert*-butyl groups, well-defined chlorinated products were obtained (Fig. 12a).[156] Analyses *via* infrared spectroscopy and X-ray photoelectron spectroscopy confirmed the formation of C–Cl bonds and the preservation of structural integrity, demonstrating that the chlorination reaction achieves atomic-level precision and high controllability (Fig. 12a). Edge chlorination significantly enhances the solubility and processability of GNRs, enabling them to form stable solutions in highly polar solvents such as *N*-methylpyrrolidone or strongly polarizable solvents like 1,2,4-trichlorobenzene (TCB), without the need for surfactants or long alkyl-chain modifications.[156] Furthermore, this modification also tunes the optical properties of GNRs. Compared to pristine GNRs, chlorinated GNRs exhibit a red shift of approximately 37 nm in their absorption peak, corresponding to a reduction in the optical bandgap from about 1.9 eV to about 1.7 eV (Fig. 12a). This change is primarily attributed to the electron-withdrawing effect of the chlorine atoms, which leads to an asymmetric stabilization of the frontier molecular orbitals: the lowest unoccupied molecular orbital (LUMO) is lowered more significantly than the highest occupied molecular orbital (HOMO), thereby narrowing the bandgap.[156] More importantly, the chlorine atoms serve as active reaction sites, enabling further chemical functionalization of GNRs *via* nucleophilic substitution or transition-metal-catalyzed coupling. For instance, they can bond with molecules containing amino, thiol, or arylboronic acid groups, thereby expanding their potential applications.

In addition to introducing halogen atoms at the edges of GNRs, functionalization with groups such as methoxy (yielding GNR-OMe) can also effectively modulate the properties of GNRs (Fig. 12b).[155] Both GNR-H and GNR-OMe with gulf edge were synthesized *via* a solution-phase bottom-up strategy, with the key steps being sequential Diels–Alder polymerization and oxidative cyclodehydrogenation. Specifically, the synthesis of GNR-OMe began with a tetraphenylcyclopentadienone-based monomer bearing four methoxy groups, which was constructed stepwise *via* the functionalization and coupling of benzene derivatives. This monomer underwent AB-type Diels–Alder polymerization under high-temperature reflux in diphenyl ether,

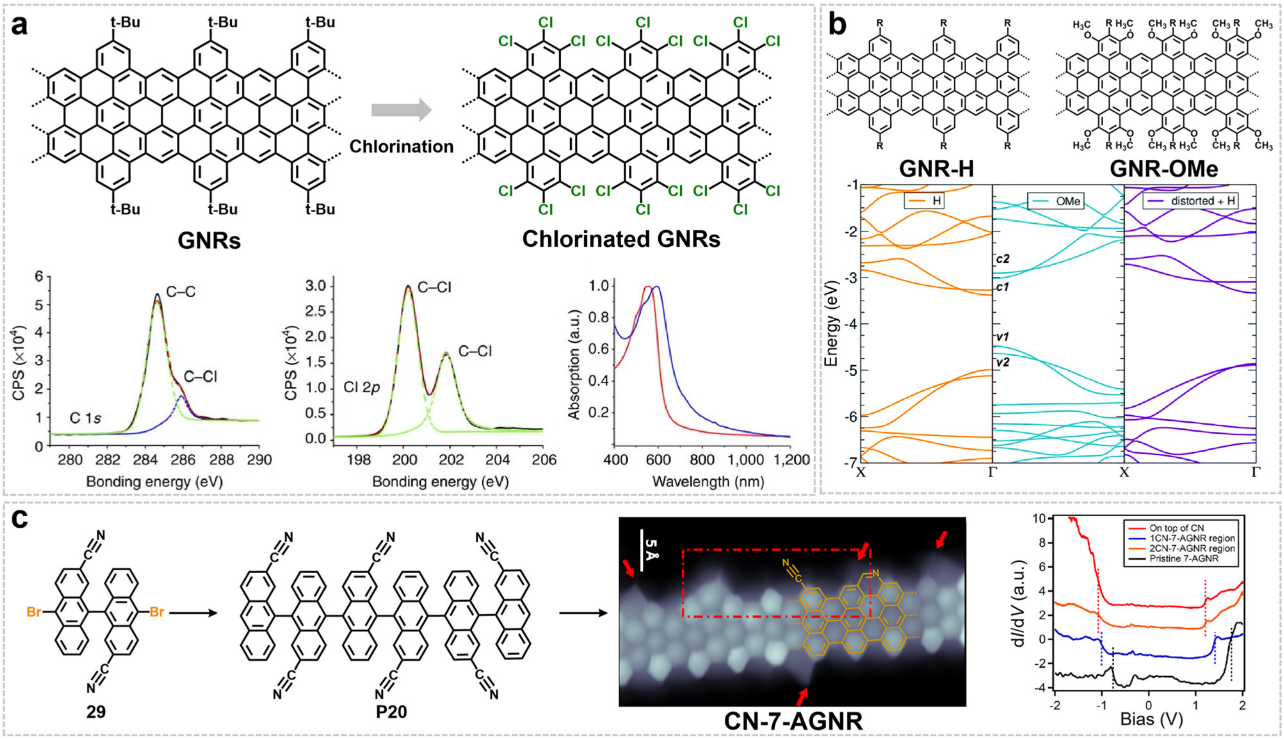

Fig. 12 (a) Scheme and characterization of chlorinated GNRs, showing the bottom-up chlorination process, C 1s XPS, and comparative UV-Vis-NIR spectra with pristine GNRs. Reprinted with permission from ref. 156. Copyright 2013, Springer Nature. (b) A comparative investigation of GNR-H and GNR-OMe encompasses their chemical structures, DFT-computed band structures. Reprinted with permission from ref. 155. Copyright 2022, The Royal Society of Chemistry. (c) Synthesis, structural, and electronic characterization of CN-7-AGNRs. Reprinted with permission from ref. 154. Copyright 2017, American Chemical Society.

yielding a methoxy-substituted polyphenylene precursor. Subsequent oxidative cyclodehydrogenation ultimately afforded well-defined methoxy-functionalized GNR-OMe. As a control, the unsubstituted reference sample GNR-H was synthesized *via* a similar route, using a monomer without methoxy substituents. Theoretical studies reveal that, compared to pristine GNR-H, the introduction of methoxy groups modulates the electronic structure through a dual mechanism (Fig. 12b): first, *via* their electron-donating effect, which induces charge redistribution; and second, through steric hindrance, which causes a non-planar distortion of the GNR backbone. These two effects act synergistically to reduce the bandgap of GNR-OMe by about 150 meV relative to GNR-H and, crucially, to significantly lower the effective mass of charge carriers. Consequently, time-resolved THz photoconductivity spectroscopy shows that methoxy functionalization enhances the photoconductivity of GNRs by approximately 25%.[155]

In contrast to electron-donating groups, the introduction of strong electron-withdrawing groups, such as the cyano group (–CN) *via* on-surface synthesis, follows distinct modulation mechanisms. As shown in Fig. 12c, incorporating CN groups into the edge of 7-AGNR induces pronounced changes not only in its electronic structure but also in its molecular architecture and assembly behavior.[154] First, CN groups act as efficient n-type dopants, resulting in a rigid downward shift of the energy bands (by approximately 0.3–0.5 eV per CN group) along with a slight reduction of the bandgap due to enhanced conjugation. Second, during synthesis, part of the CN groups (*ca.* 35%) undergoes detachment, while a fraction of the remaining intact CN groups can isomerize on the surface and convert *in situ* into pyridine-type rings, revealing a novel reaction pathway (Fig. 12c). Moreover, the introduction of CN leads to a shortening of the GNR length and promotes its oriented alignment on the surface, attributed to intermolecular dipole–dipole interactions. Theoretical calculations further corroborate that the edge-anchored CN groups generate a strong dipole moment directed toward the GNR backbone, lowering the local electrostatic potential and thereby substantially increasing the overall electronegativity of the GNR.[154]

To further expand the dimensionality of functional modulation, larger functional units such as imide rings have also been incorporated at the edges of GNRs.[157–159] For instance, by pre-introducing C–Br bonds into polyphenylene precursors and using Suzuki coupling reactions, precise edge functionalization with groups such as anthraquinone and naphthalene/perylene monoimide (NMI/PMI) can be achieved prior to oxidative cyclodehydrogenation.[160] Compared to pristine GNRs, the absorption spectrum of GNR-NMI shows significant broadening and a redshift in the 400–500 nm range, which can be attributed to aggregation of the NMI units or interactions with adjacent GNRs. Furthermore, AFM studies reveal that edge functionalization can markedly regulate the self-assembly behavior of GNRs. For example, GNR-PMI functionalized with perylene monoimide units forms well-ordered rectangular network structures.[160] Nuckolls *et al.* has conducted extensive research on GNRs with imide ring substitutions.[152,153,158,159] In 2020, they reported the synthesis of GNRs functionalized with imide side chains (Fig. 13a). This strategy involves coupling an electron-deficient perylene diimide (PDI) dimer unit (**30**) to an electron-rich pyrene unit (**31**) *via* Suzuki coupling to construct a linear polymer precursor (cGNR-unc). Subsequently, a visible-light-driven flow photocyclization reaction is employed to achieve efficient and quantitative cyclization of the polymer in solution, yielding a fully conjugated GNR structure.[158] This two-step synthesis is conducted under mild conditions with high yield, producing twisted n-type GNRs of approximately 50 nm in length, with regular structure and minimal defects. The resulting GNRs exhibit reversible electron-acceptor behavior in solution, while thermal removal of the alkyl side chains leads to a substantial enhancement in their film conductivity (Fig. 13a). On the basis of incorporating imide structures into GNRs, by modifying the imide sites with chiral side chains (such as *S*- or *R*-phenethylamine derivatives), the point chirality information can be transmitted to the GNR backbone, inducing the formation of helical structures with single-handedness (chGNRs) (Fig. 13b).[153] This process originates from the synergistic effect between the inherent non-planar cove-edge topology of the imide rings and the stereochemical induction from the chiral side chains. In 2025, the same group further developed a twisted acene-type GNR with excellent mixed ion/electron conductivity (Fig. 13c). The synthesis involved Stille polycondensation, visible-light-driven cyclization, and post-functionalization to introduce hydrophilic side chains (Fig. 13c). This strategy preserves the conjugated backbone for efficient electron transport, while molecular twisting and side-chain engineering synergistically enhance ion transport capability.[159]

3.3.2 Edge functionalization of GNRs. One of the key challenges in the solution-phase synthesis of GNRs is overcoming their limited processability, which stems from pronounced inter-ribbon π–π stacking and strong van der Waals interactions. To mitigate these issues, different edge-functionalization strategies have been developed, including the covalent attachment of polymer chains, hyperbranched macromolecules, or sterically demanding rigid substituents along the GNR peripheries (Fig. 14). Such modifications not only enhance solubility and dispersion stability in organic and aqueous media but also help to suppress aggregation while preserving the electronic integrity of the GNR.[42,44,60,68,75,161] The resulting solution-processable GNRs open pathways for advanced fundamental studies and device-oriented applications, such as the single-electron transistors, intrinsic photoluminescence properties of individual GNR, controlled hierarchical self-assembly in solution, and the development of functional hybrids for biomedical sensing or delivery systems.[24,25,42–44,60,67,68,75,161]

In 2016, our group first reported a bottom-up solution-phase synthesis strategy for preparing structurally well-defined poly(ethylene oxide) (PEO)-functionalized GNRs (Fig. 14a).[75] This route involved pre-introducing ester groups into the monomer units (**33**), followed by polymerization and cyclodehydrogenation to yield GNRs bearing peripheral ester groups. These esters were subsequently hydrolyzed to carboxyl groups (GNR-COOH) and

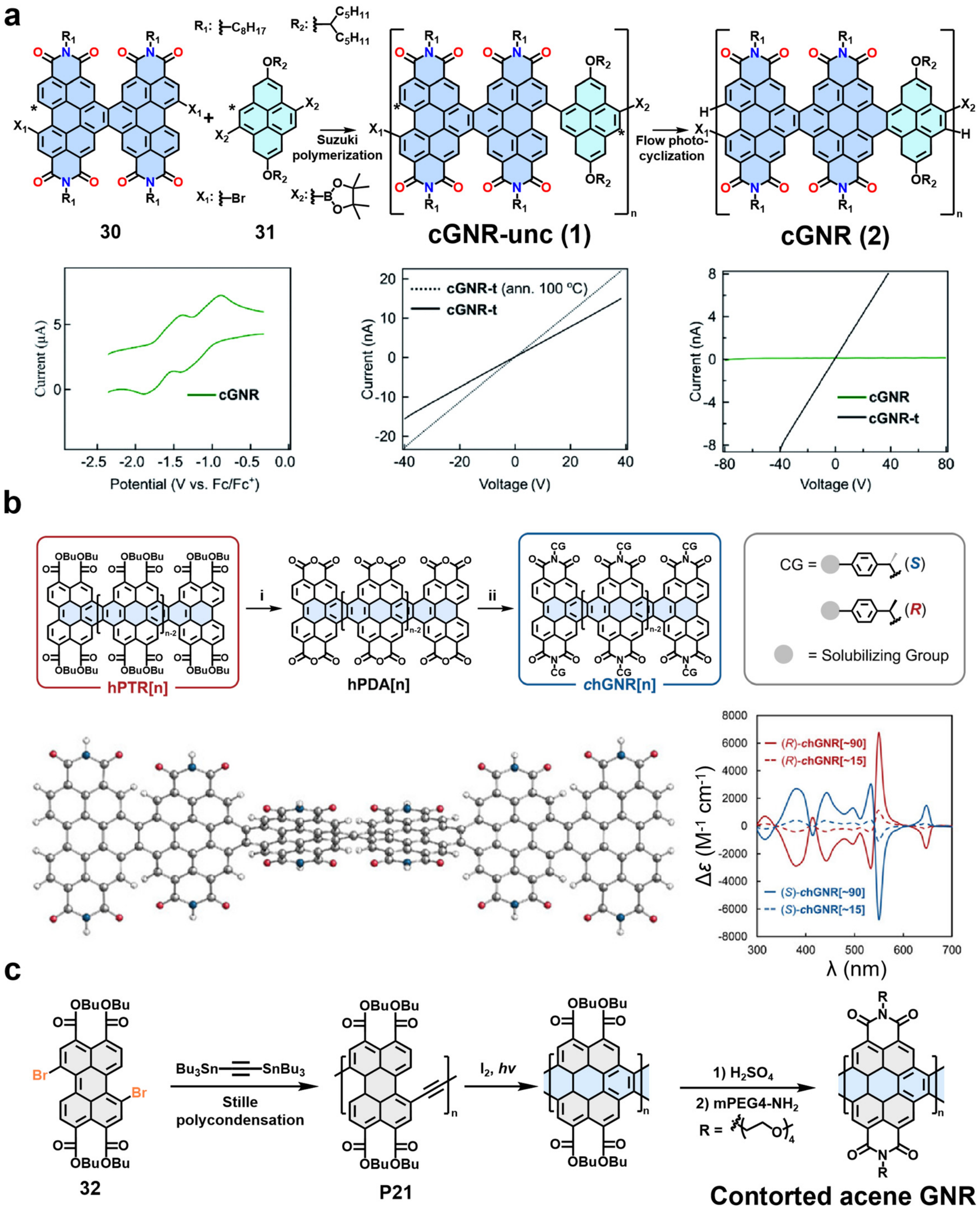

Fig. 13 (a) Synthesis and charge transport characterization of PDI-based GNRs (cGNR and cGNR-t), including cyclic voltammetry and comparative pellet conductivity measurements. Reprinted with permission from ref. 158. Copyright 2020, The Royal Society of Chemistry. (b) Synthesis and chiroptical properties of chGNRs, as well as the DFT-optimized geometry of (*S*)-chGNR[6]. Reprinted with permission from ref. 153. Copyright 2025, Wiley-VCH. (c) Synthetic strategy for contorted acene GNR. Reprinted with permission from ref. 159. Copyright 2025, American Association for the Advancement of Science.

then esterified to covalently graft PEO chains onto the GNR edges, achieving a grafting percentage of up to 46%. The flexible and solvophilic PEO chains effectively suppress π–π aggregation of the GNR backbones by forming coiled or entangled bundles between adjacent ribbons, while their low adsorption energy on graphite keeps them preferentially in solution. Similarly, benzyl ether-type dendrimer monomers of different generations (G1–G3) were synthesized and covalently grafted onto pre-synthesized edge-carboxylated GNRs *via* esterification, yielding the GNR-G1 to GNR-G3 series with grafting ratios of 0.59–0.68 (Fig. 14a).[162] The bulky 3D conformation of the grafted dendrons weakens the π–π interaction of the GNR backbones

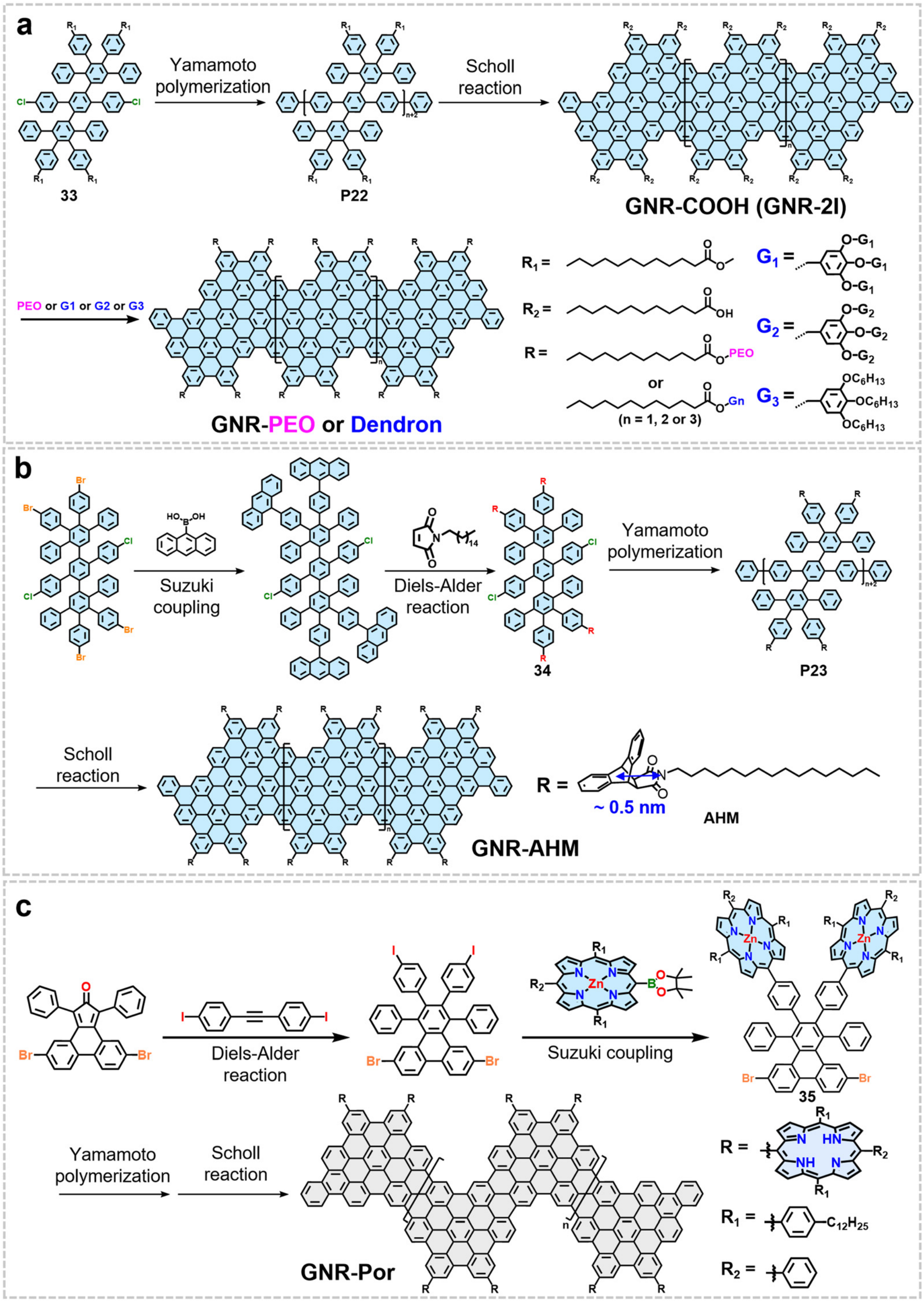

Fig. 14 Schematic illustration of the edge-functionalization strategy for GNRs. (a) Grafting of polymer chains or hyperbranched polymers onto GNR edges; (b) and (c) introduction of sterically bulky groups (AHM group or porphyrin ring at the edges).

through steric hindrance, which is the key to their improved processability.

While functionalization strategies, such as grafting polymers or hyperbranched molecules onto the edges of GNRs, can enhance their dispersibility in solvents, they still struggle to completely suppress interlayer π–π stacking, thereby preventing GNRs from being effectively exfoliated into individual ribbons in solution. In this respect, our group developed a strategy for grafting the anthracene-hexadecylmaleimide (AHM) side group synthesized through Diels–Alder cycloaddition between anthracene units and *N*-hexadecylmaleimide onto GNR edges (Fig. 14b).[42] This side group is synthesized through Diels–Alder cycloaddition between anthracene units and *N*-hexadecylmaleimide. The bulky AHM side groups possess a radius of ∼0.5 nm, exceeding the interlayer spacing of graphite (∼0.34 nm), thereby effectively hindering π–π stacking (Fig. 14b) and thus promoting the exfoliation of GNRs into individual ribbons in solution.[42]

In 2026, Mai *et al.* reported a strategy for synthesizing structurally defined porphyrin-edge-functionalized GNRs (GNR-Por) in solution (Fig. 14c).[44] The synthesis begins with the construction of a polycyclic precursor *via* Diels–Alder cycloaddition, followed by the introduction of porphyrin units at *ortho* positions through a selective Suzuki reaction. Subsequently, a Ni(0)-catalyzed Yamamoto polymerization yields a poly(*para*-phenylene) precursor decorated with Zn–porphyrin moieties on both sides, which is finally converted into chevron-type GNR-Por *via* Scholl cyclodehydrogenation accompanied by concurrent demetallization (Fig. 14c). The key to this synthetic strategy lies in the precise grafting of bulky porphyrin groups onto the edges of GNRs. The porphyrin groups have a lateral dimension of approximately 1.5 nm, which exceeds the interlayer spacing of graphite (about 0.34 nm). Their significant steric hindrance both effectively suppresses aggregation caused by π–π stacking and induces a periodically undulating wavy geometry in the GNR backbone. Together, these two effects promote the single ribbon dispersion of GNRs in solution.[44]

The GNRs produced *via* the aforementioned synthetic strategies exhibit excellent solution dispersibility, tunable self-assembly behavior, and unique optoelectronic properties, as summarized in Fig. 15. Grafting PEO chains imparts excellent solvophilicity to GNR-PEO, enabling dispersion concentrations of up to 1 mg mL^{-1} in common organic solvents and 0.2 mg mL^{-1} in aqueous solution (Fig. 15a). The UV-vis spectrum of its tetrahydrofuran (THF) dispersion shows an absorption peak around 650 nm (optical bandgap ∼1.3 eV), which exhibits a significant redshift in aqueous solution, corresponding to a narrowed bandgap of ∼1.0 eV (Fig. 15a).[75] By adjusting the length of the PEO segments, the self-assembly behavior of GNR-PEO in water can be effectively tuned (Fig. 15b). Leveraging its unique ''rod-coil'' brush-like molecular architecture, the system undergoes one-dimensional hierarchical self-assembly, forming ribbon- or helical-spring-like superstructures whose diameter and pitch can be modulated with PEO chain length (Fig. 15b).[68] The resulting assemblies exhibit strong near-infrared absorption in the 750–850 nm range and display excellent photothermal conversion performance.

In contrast to the PEO-based strategy, edge functionalization with the sterically demanding AHM side group dramatically enhances the dispersibility of GNR-AHM, enabling a dispersion concentration exceeding 5 mg mL^{-1} in THF. Dilute solutions (<0.1 mg mL^{-1}) consist predominantly of individually dispersed GNRs,[25,42,43] as evidenced by dynamic light scattering, the linear relationship between PL intensity and concentration, and ultrafast transient absorption spectroscopy revealing molecular-like excited-state dynamics (Fig. 15c). These dispersions exhibit near-infrared emission with a high quantum yield (9.1%) and a long lifetime (8.7 ns).[42] Building on the aforementioned edge-functionalization strategies, we also synthesized molecular GNRs (MGNR 2) and successfully fabricated single-electron transistors exhibiting exceptionally clean electronic transport properties (Fig. 16).[25] The presence of three-dimensional bulky side groups significantly suppresses π–π stacking between GNRs, enabling high solubility exceeding 5.0 g L^{-1} in solvents (such as chloroform, Fig. 16a) and resulting in bright fluorescence. PL measurements

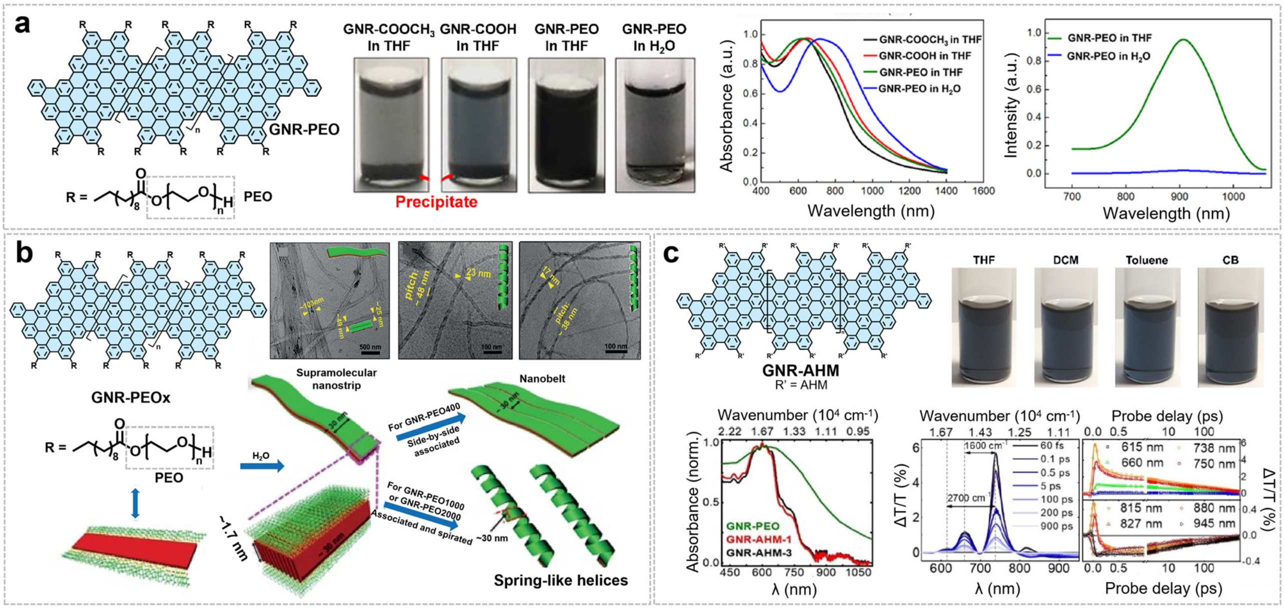

Fig. 15 (a) The structure of GNR-PEO, along with photos of its dispersions in THF and H$_2$O, as well as UV-vis and PL spectra of the dispersions. Reprinted with permission from ref. 75. Copyright 2016, American Chemical Society. (b) Molecular structure of GNR-PEOs and their hierarchical self-assembly in H2O, with corresponding TEM images of the resulting superstructures. Reprinted with permission from ref. 68. Copyright 2018, Wiley-VCH. (c) Structure, spectral properties, and ultrafast spectral characterization of GNR-AHMs. Reprinted with permission from ref. 42. Copyright 2018, American Chemical Society.

further reveal that at low concentrations (below 0.1 g L^{-1}), the emission spectrum comprises two distinct peaks centered at 625 nm and 670 nm, with peak areas increasing with concentration; above this threshold, the high-energy peak disappears, indicating suppressed inter-ribbon exciton transfer due to effective debundling (Fig. 16b). In contrast, conventionally alkyl-chain-modified GNRs show severe aggregation, which hinders the construction of single-GNR devices (Fig. 16b). In terms of device performance, MGNR 2-based single-electron transistors display electronic transport cleanliness comparable to that of suspended carbon nanotube systems: their stability diagrams exhibit well-defined, periodic Coulomb diamonds with sharp edges and a series of distinct excited-state spectral lines (Fig. 16b). Further analysis reveals pronounced electron–phonon coupling, corroborated by the observation of a Franck–Condon blockade.[25]

Additionally, introducing functional groups into GNRs enables distinct functionalities. For instance, grafting nitronyl nitroxide radicals onto GNR edges experimentally confirmed long-predicted magnetic edge states, revealing room-temperature spin coherence times in the microsecond range and enabling coherent spin manipulation.[27] By synthesizing gulf-type edge GNRs bearing azide groups (N_3-cGNRs) and covalently attaching Cy5 fluorescent dyes *via* copper-catalyzed click chemistry, Fischer *et al.* successfully achieved high-resolution, non-destructive optical imaging of individual GNRs on insulating substrates such as glass, silicon, and silicon/silicon dioxide. Using super-resolution radial fluctuation technology, this method enhanced spatial imaging resolution to approximately 40–50 nm, significantly surpassing the optical diffraction limit, thereby enabling clear distinction between isolated GNRs and GNR bundles.[163]

4. Backbone engineering in GNRs

Unlike merely modifying the edge configuration of GNRs, directly performing chemical design on the GNR backbone—such as constructing hybrid backbones, introducing non-hexagonal topological units, creating pores in the backbone, and precisely incorporating curvature and strain—can fundamentally reshape the distribution of their electronic wavefunctions, modulate charge-carrier transport pathways, and tailor quantum confinement effects. These backbone-level modulations not only enable continuous tuning of GNR bandgaps and band alignments over a wide range but also introduce magnetic properties and topological boundary states that are difficult to achieve *via* the aforementioned edge-engineering strategies.[67,113,123,164,165]

4.1 GNR hybrids

In the last section, we discussed how structurally precise precursors can be used *via* bottom-up synthesis to achieve selective heteroatom doping at the edges of GNRs and examined the influence of different doping elements on their properties. In this section, we further summarize recent efforts to embed heteroatoms into the backbone lattice, thereby yielding hybrid GNR architectures, and discuss how such backbone

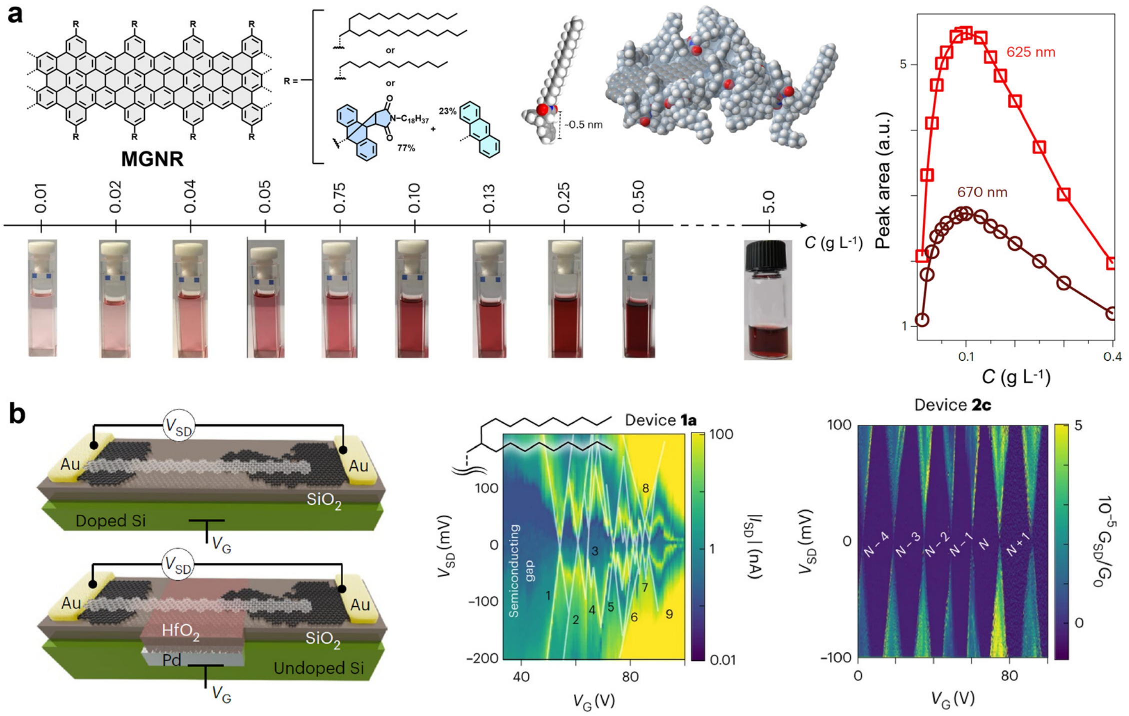

Fig. 16 (a) Structure of the MGNR backbone with highlighted side-chain functionalization, relationship between PL peak areas and *C* for the two constituent peaks at 625 nm and 670 nm within the broad emission band, and dispersibility in chloroform solutions at varying concentrations. (b) Device geometries and comparison of quantum transport properties between alkyl-chain-functionalized GNRs and MGNRs. Reprinted with permission from ref. 25. Copyright 2023, Springer Nature.

modifications regulate the intrinsic properties of GNRs. We will also discuss strategies for integrating macrocyclic structures (such as porphyrins) directly into the GNR backbone. Compared to doping solely at the edges, introducing heteroatoms or heterocyclic structures into the backbone lattices exerts a more profound and versatile influence on the hybrid systems. This approach allows for a global reconstruction of the electronic band structure, enabling transformative changes such as the engineering of bandgap types, achieving metallicity with ballistic transport, introducing and precisely coupling spin centers, and even inducing topological phase transitions.[23,67,164,166,167]

Boron stands out for its electron-deficient nature and Lewis acidity. Introducing boron atoms into aromatic carbon frameworks can impart diverse functional properties to materials. However, the intrinsic susceptibility of organoboron compounds to moisture and oxygen has long impeded progress in the field of boron-doped GNRs. A representative work on boron atom doping in GNRs was reported in 2015 by Meyer *et al.*, who successfully synthesized boron-doped GNRs (B-GNRs) with widths of $N = 7$, 14, and 21 *via* on-surface chemical reactions using organoboron precursors (**36**) (Fig. 17a).[113] The boron atoms were precisely doped along the center row of the GNRs with a doping density of 4.8 atom%. Boron doping did not significantly alter the bandgap of the GNRs ($\sim$2.4 eV), but its electron-acceptor character introduced localized electronic states, enhanced the coupling between the GNRs and the metal substrate, and suppressed electron backscattering. The chemical reactivity of B-GNRs was explored through nitric oxide (NO) adsorption experiments (Fig. 17a), which revealed that NO molecules are most effectively captured at the boron sites, confirming their Lewis-acid character.[113]

In 2020, Pascual *et al.* reported the precise incorporation of boron atom pairs into 7-AGNRs, enabling effective control over topological boundary states and magnetism in GNRs (Fig. 17b).[115] A surface-assisted synthesis strategy was employed, in which boron-substituted trianthracene precursors (**38**) were co-deposited

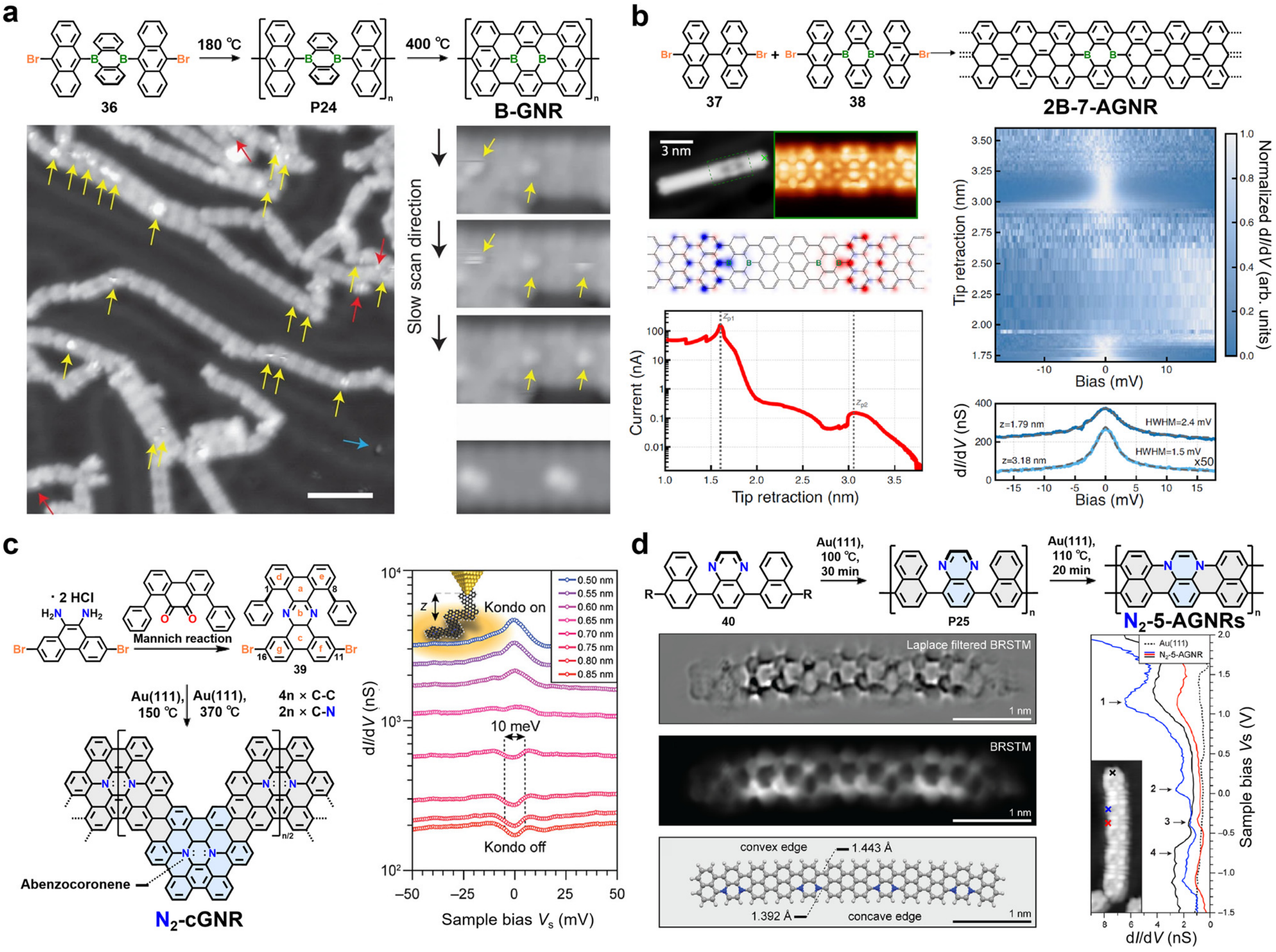

Fig. 17 (a) Synthesis of boron-doped GNRs and STM topography of B-GNR with NO molecules. Reprinted with permission from ref. 113. Copyright 2015, Springer Nature. (b) Multiscale characterization of the borylated GNR integrating constant-current/height STM imaging, cotunneling transport measurements with zero-bias resonance analysis. Reprinted with permission from ref. 115. Copyright 2020, American Physical Society. (c) Synthesis of N_2-cGNR and STS lift-off experiment performed on a heptamer N_2^+-cGNR. Reprinted with permission from ref. 123. Copyright 2022, American Chemical Society. (d) Bottom-up synthesis of N_2-5-AGNRs, bond-resolved STM (BRSTM) images and optimized structure of a tetramer, as well as the STS dI/dV spectra of the N_2-5-AGNRs. Reprinted with permission from ref. 120. Copyright 2023, American Chemical Society.

with undoped trianthracene-based precursors (**37**) on a metal substrate, followed by controlled polymerization and cyclization to successfully fabricate boron-doped 7-AGNRs (2B-7-AGNRs). The resulting 2B-7-AGNRs exhibit unique structural characteristics: the introduction of boron pairs significantly disrupts the π-electron conjugation system and induces localized spin-polarized boundary states on both sides (Fig. 17b). STM combined with transport measurements reveals that after decoupling the boron pairs from the metal substrate, the system displays clear Kondo resonance features, confirming the presence of spin states (Fig. 17b). DFT calculations confirmed that boron pairs disrupt π-conjugation and create localized spin-polarized boundary states, with spin configuration controlled by boron spacing and electron interactions.[115]

Precise nitrogen doping within the GNR backbone enables cooperative tuning of their electronic and spin properties. In 2022, Fischer and colleagues reported the design and synthesis of GNRs (N_2-cGNRs) doped with nitrogen atoms in the backbone using 11,16-dibromo-1,8-diphenyltetrabenzo[*a*,*c*,*h*,*j*]phenazine (**39**) as the monomer (Fig. 17c).[123] This backbone nitrogen doping strategy introduces extra π-electrons per unit cell of the GNR. Through charge transfer with the Au substrate, each unit loses one electron, forming a one-dimensional radical cation chain (N_2^+-cGNRs). STS measurements revealed a characteristic Kondo resonance peak at zero bias, confirming strong correlated interactions between the S = 1/2 spin carried by each diazahexabenzocoronene unit and the conduction electrons of the Au substrate. Combined "lift-off" transport experiments and first-principles calculations further revealed an exchange coupling of approximately 5 meV between neighboring spin centers and theoretically predicted that isolated N_2^+-cGNRs possess a ferromagnetically ordered ground state (Fig. 17c).[123] In 2023, they further succeeded in preparing nitrogen-core-doped 5-AGNRs (N_2-5-AGNRs) through an on-surface synthesis strategy (Fig. 17d).[120] The synthesis was achieved using 5,8-bis(4-iodonaphthalen-1-yl)quinoxaline (**40**) as the monomer. After deposition onto a Au(111) surface, the monomer underwent a two-step reaction sequence consisting of low-temperature step-growth polymerization followed by high-temperature cyclodehydrogenation, resulting in the efficient formation of fully aromatized GNR structures (Fig. 17d). The key to this synthetic route lies in leveraging the lower bond dissociation energy of the C–I bond to enable controlled polymerization and in utilizing surface-mediated cyclization to form C–N and C–C bonds, ultimately achieving precise embedding of nitrogen atoms within each repeating unit. The resulting N_2-5-AGNRs exhibit a distinctive asymmetric "convex–concave" edge morphology, accompanied by significant bond-length alternation and mirror-symmetry breaking (Fig. 17d). This "core-edge cooperative" doping configuration not only induces a Fermi-level shift of approximately 1.0 eV but also drives a transition from a direct to an indirect bandgap, alongside modulation of the topological order (Fig. 17d).[120]

In 2018, Foster and colleagues achieved precise co-doping of boron and nitrogen in GNRs *via* on-surface chemical reactions (Fig. 18a). Using 5-(10-chloroanthracen-9-yl)-10-(10-iodoanthracen-9-yl)-5,10-dihydrodibenzo[*b*,*e*][1,4]azaborinine (**41**) as the precursor molecule—a structure comprising three anthracene units linked by single bonds with a central C_4BN ring—they successfully synthesized an N = 7 B–N co-doped GNR (BN-GNR) through a two-step annealing process.[116] The key to this synthesis strategy lies in exploiting the differing reactivity of the halogen substituents (Cl and I) in the precursor. By regulating the coupling pathways, the doping sequence and structural periodicity can be precisely controlled, enabling accurate tuning of heteroatom positions and doping density. With CO-functionalized high-resolution AFM, they distinguished B, C, and N atoms directly at the atomic scale for the first time (Fig. 18a). STM further revealed that the BN-GNR on Au(111) exhibits a bandgap of approximately 2.3 eV, with the valence band maximum (VBM) located at about -0.3 eV and the conduction band minimum (CBM) at about +2.0 eV. Compared to the band edge positions of the pristine 7-AGNR, those of the BN-GNR are shifted upward by about 0.4 eV. This rigid band shift is attributed to the symmetric incorporation of B and N atoms at the center of the GNRs. Furthermore, in-gap impurity states were observed at +1.2 eV and +1.4 eV, which are assigned to a donor level introduced by nitrogen and an acceptor level introduced by boron, respectively (Fig. 18a).[116]

In 2025, Li *et al.* synthesized two oxygen-doped GNRs, a chevron type and a chiral (2,1) type, on Au(111) from the precursors 1,4-dibromoanthraquinone (**43**) and 1,5-dibromoanthraquinone (**44**).[114] The process involved an initial surface-catalyzed debrominative C–C coupling, followed by stepwise dehydrogenative C–O coupling reactions (Fig. 18b). The study reveals that both types of GNRs are direct-bandgap semiconductors but exhibit distinct responses to oxygen doping: oxygen dopants have a minor impact on the bandgap of chevron-GNR (increasing from 0.72 eV to 0.76 eV), whereas they significantly enlarge the bandgap of chiral (2,1)-GNR (from 0.6 eV to 1.56 eV). This difference originates from the varying contributions of the substituted intrinsic carbon atoms to the density of states near the Fermi level (Fig. 18b). Notably, in chiral (2,1)-GNR, the sp^2-hybridized oxygen atoms introduce extra electrons into the conduction band, leading to an upward shift of the Fermi surface and a transition of the band edges from the X point to the Γ point in the Brillouin zone.[114]

Another important hybrid strategy involves embedding extended π-systems, such as porphyrins, into the backbone of GNRs. Fusing porphyrin (or metalloporphyrin) units not only provides well-defined doping sites that impart localized magnetic moments but also helps maintain structural integrity during the synthesis due to their stable coordination environment.[23,59,67,164,166,167] The work by Fasel, Müllen, and colleagues reported the on-surface synthesis of ZGNRs with periodic porphyrin edge extensions (Por-ZGNRs), as illustrated in Fig. 19a.[59] To covalently incorporate porphyrin units along the zigzag edges of 3-ZGNRs, they designed 5-(2,7-dibromoanthracen-9-yl)porphyrin, MPor-DBA (**45**) as the key molecular precursor. This modular design encompasses the free-base porphyrin (M = 2H, 2HPor-DBA) as well as metallated derivatives with Zn or Fe coordinated in the macrocyclic core (ZnPor-DBA and FePor-DBA). The two bromine substituents on the anthracene moiety

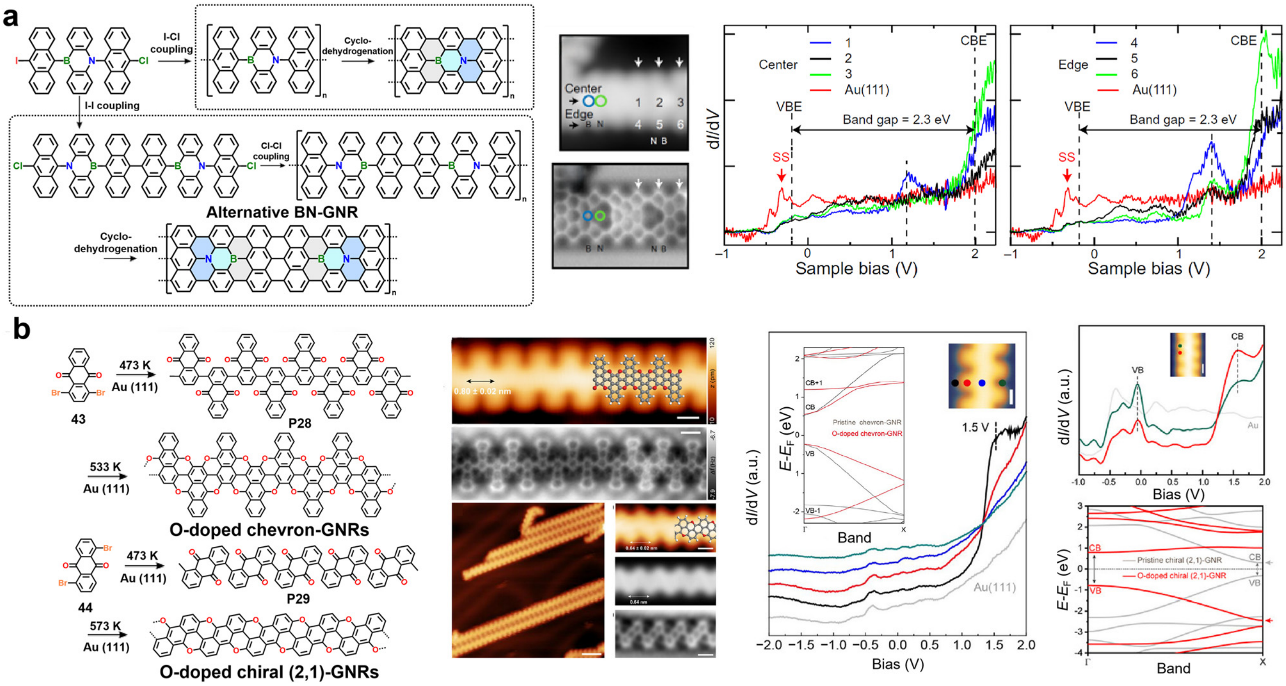

Fig. 18 (a) Comprehensive study encompassing the synthesis, characterization, and electronic properties of multiple heteroatom-substituted BN-GNRs. Reprinted with permission from ref. 116. Copyright 2018, American Association for the Advancement of Science. (b) Structures, STM/AFM characterization and electronic properties of O-doped chevron and chiral (2,1) GNRs. Reprinted with permission from ref. 114. Copyright 2025, Wiley-VCH.

serve as reactive handles for subsequent surface-mediated polymerization. During the on-surface synthesis, the precursors undergo thermally initiated homocoupling *via* C–Br bond cleavage, ultimately yielding a hybrid architecture in which porphyrin units are periodically fused into the GNR backbone (Fig. 19a). This structural design enables strong electronic coupling between the π-system of the porphyrins and the ZGNR framework. The results highlight that the integration of porphyrin motifs not only modulates the bandgap of the GNR through π-extension and strain effects but also allows precise tailoring of electronic and spin properties *via* the choice of transition metal (*e.g.*, Zn, Au, Fe) hosted within the porphyrin cavity.[59]

PGNRs with embedded porphyrin units can also be prepared *via* a solution-based synthetic route by designing monomers that incorporate porphyrin structural motifs.[67] Monomer (**46**), a dichloro-substituted nickel(II) porphyrin was synthesized and employed as the key building block by Anderson *et al.* in 2024. This monomer has been structurally optimized in multiple dimensions: bulky 2,6-dimethyl-4-dodecylphenyl groups were introduced at the meso positions of the porphyrin to suppress intermolecular aggregation in subsequent steps and ensure solubility of the final product; the nickel(II) ion integrated into the porphyrin core effectively prevents protonation of the porphyrin ring during the subsequent strong-acid cyclization step; more importantly, two chloro-substituted aryl reaction sites are extended from the porphyrin core *via* benzo[*m*]tetraphene structural units, providing precise coupling sites for linear polymerization. Through Yamamoto coupling and cyclodehydrogenation, structurally well-defined, PGNRs with fjord-edge topology are obtained (Fig. 19b). The PGNRs exhibit good solubility in common organic solvents such as toluene, 1,2-dichlorobenzene and TCB, benefiting from the twisted fjord-edge structure and flexible side chains that hinder π–π aggregation. They display a narrow optical bandgap of ∼1.0 eV, estimated from the absorption onset at ∼1200 nm, and a high intrinsic charge mobility ($\mu = e\tau/m^*$) of 450 $cm^2\ V^{-1}\ s^{-1}$ as revealed by time-resolved terahertz spectroscopy. These PGNRs can be used to construct high-performance single-molecule devices, such as field-effect transistors with ambipolar transport and high on/off ratios (10^3), as well as single-electron transistors showing Coulomb diamonds and negative differential conductance at low temperature (Fig. 19b).[67]

4.2 Nonbenzenoid GNRs

Introducing non-hexagonal rings into the sp^2-hybridized carbon lattice represents an important strategy for tuning the band structure of GNRs by inducing lattice imbalance. As intrinsic topological defects, non-hexagonal rings break the continuity of the ideal hexagonal lattice, giving rise to local lattice distortion, curvature-induced strain, and boundary-state reconstruction, thereby modulating carrier localization behavior, band-gap magnitude, and even spin distribution at the atomic scale.[76–79,104,105,168–170] Theoretical studies indicate that non-hexagonal rings, such as Stone–Wales defects, can induce localized electronic states and impart notable metallic or magnetic characteristics in carbon nanostructures. This "defect engineering" approach extends beyond the traditional regulation based solely on size and edge structure, offering a new pathway for band-structure design of GNRs (Fig. 20).

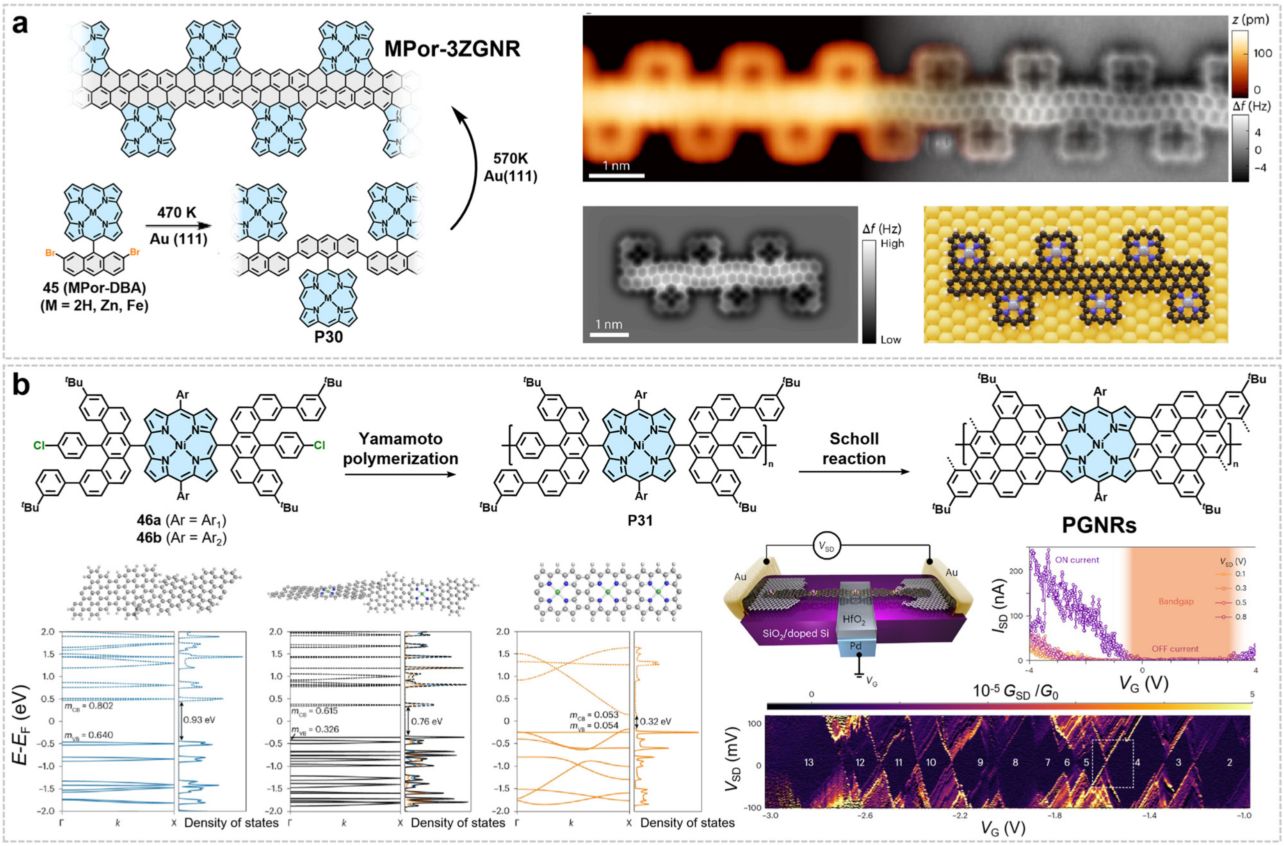

Fig. 19 (a) On-surface synthesis and STM/AFM characterization of MPor-3ZGNRs. Reprinted with permission from ref. 59. Copyright 2025, Springer Nature. (b) Synthesis and electronic properties of PGNRs, and their transistor and single-molecule charge transport performance. Reprinted with permission from ref. 67. Copyright 2024, Springer Nature.

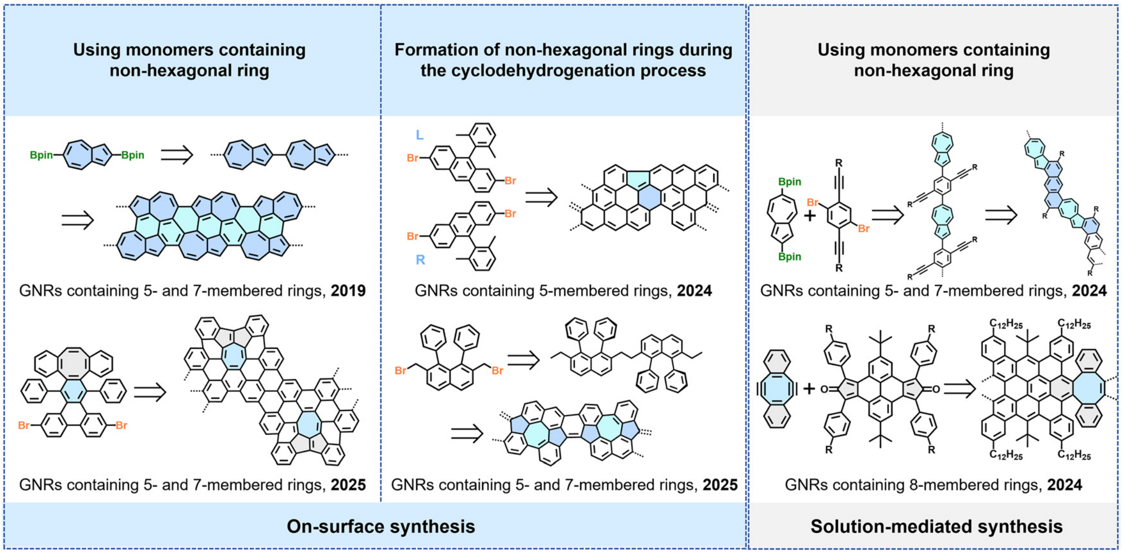

Fig. 20 Synthesis of GNRs containing non-hexagonal rings through tailored monomer design and controlled reaction pathways.

Therefore, this section reviews recent advances in the introduction of non-hexagonal ring structures into the backbone of GNRs. First, synthetic approaches based on oligophenylene precursors containing five- or seven-membered rings will be introduced. Subsequently, the latest breakthroughs in the on-surface synthesis of GNRs containing five-, seven-, or eight-membered rings, achieved through specifically designed precursor monomers, will be highlighted. In addition, we will also emphasize recent progress in preparing non-hexagonal-ring-containing GNRs *via* solution-phase synthesis.

Integrating non-benzenoid structural motifs into the backbone of GNRs represents a direct and effective strategy, which involves the design and synthesis of precursor monomers containing predefined non-hexagonal ring units, such as five- and seven-membered rings. Subsequently, these predetermined topological defects can be precisely translated into the final one-dimensional nanostructures *via* on-surface polymerization and cyclodehydrogenation reactions. In 2020, we designed and synthesized a monomer that incorporates a core-embedded 5-membered ring unit (**47**) (Fig. 21a).[171] Through a series of thermally driven on-surface reactions on Au(111), including dehalogenative coupling, oxidative ring-closure, and cyclodehydrogenation, this monomer was successfully converted into a nanographene containing multiple non-benzenoid topological units (such as pentalene and as-indacene) along with fused heptagonal rings. The resulting combination of 5- and 7-rings constitutes unique azulene-like topological defects, which significantly modulate the electronic structure of the GNR. This leads to a reduction in the frontier electronic gap and endows the system with open-shell biradical character. In-depth studies further revealed that surface-catalyzed skeletal ring-rearrangement reactions, driven by intramolecular strain, serve as a key step in the structural evolution (Fig. 21a).[171]

With a similar design principle, the bottom-up fabrication of GNRs containing precisely defined non-hexagonal rings has also been achieved through the use of tailored molecular precursors. For instance, in 2019, Gottfried *et al.* reported a method for preparing GNRs with non-alternant topology *via* an on-surface synthesis strategy (Fig. 21b).[78] Using 2,6-dibromoazulene (**48**) as the precursor, they successfully constructed polyazulene chains (**P32**)—consisting of fused pentagon-heptagon units—through on-surface Ullmann coupling. These chains can be regarded as one-dimensional line defects with continuous 5/7 ring sequences. Subsequently, lateral dehydrogenative coupling was employed to achieve precise "fusion" between two polyazulene chains, leading to the synthesis of two types of novel non-hexagonal GNRs: one structurally consistent with the theoretically predicted phagraphene nanoribbon, and the other forming a TPH-GNR containing four-, five-, and seven-membered rings (Fig. 21b). Both structures

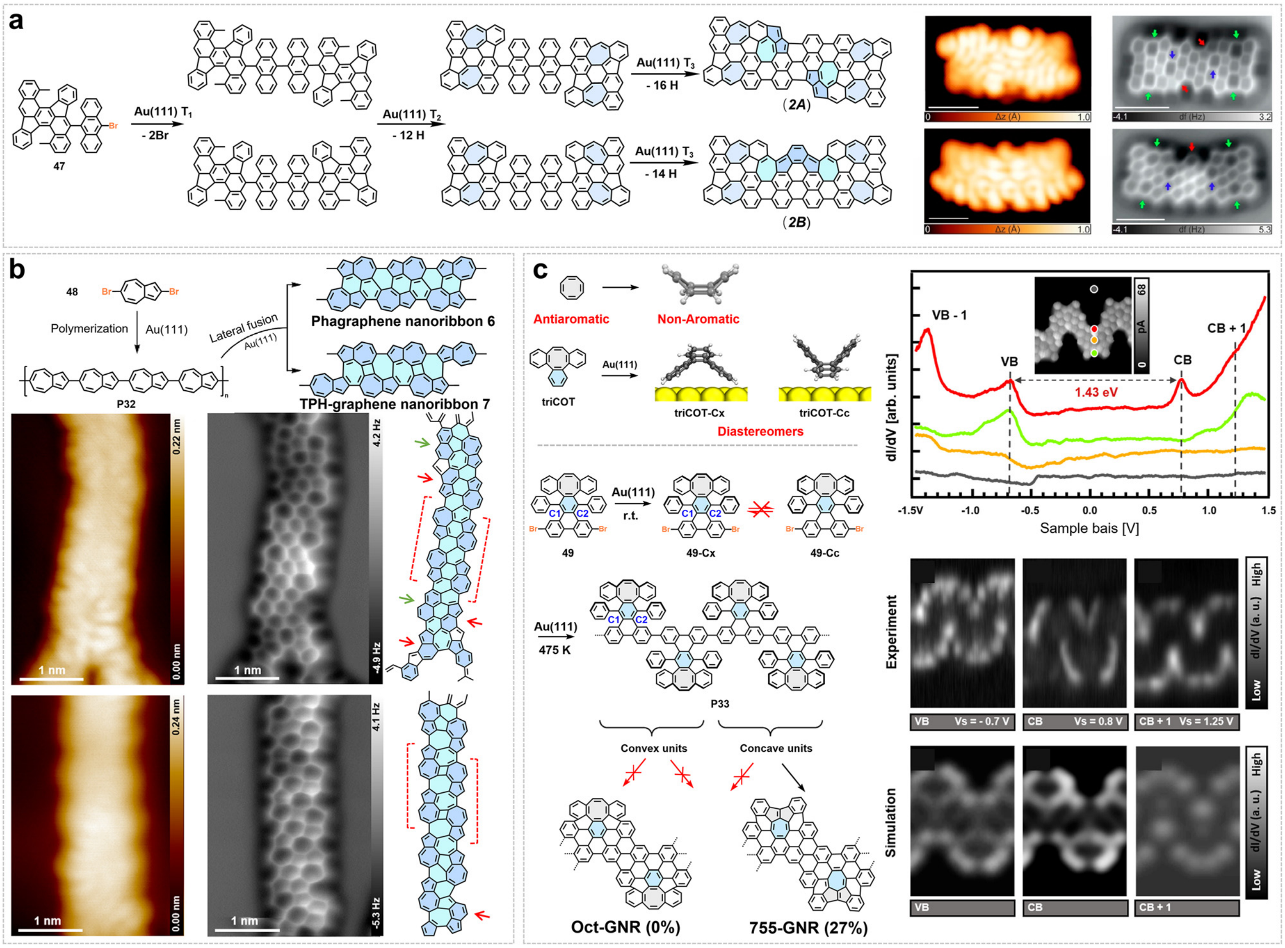

Fig. 21 (a) On-surface synthesis of non-benzenoid nanographenes by oxidative ring-closure and ring-rearrangement reactions. Reprinted with permission from ref. 171. Copyright 2020, American Chemical Society. (b) Synthesis of phagraphene and TPH-GNRs *via* Ullmann coupling of 2,6-dibromoazulene, with STM/nc-AFM characterization on Au(111). Reprinted with permission from ref. 78. Copyright 2019, American Chemical Society. (c) Schematic representation of the on-surface synthesis of the cyclopentaazulene-containing GNR (755-GNR) and the electronic characterization of the 755-GNR segment. Reprinted with permission from ref. 169. Copyright 2025, American Chemical Society.

originate from non-benzenoid, non-alternant π-electron systems, and their formation is determined by the relative alignment of the polyazulene chains, demonstrating controllable structural evolution in surface reactions. This work not only, from a synthetic chemistry perspective, illustrates the feasibility of precisely constructing complex non-hexagonal ring structures through stepwise on-surface reactions (coupling-isomerization-fusion), but also highlights the unique electronic properties of such non-alternant topological GNRs, which exhibit narrower bandgaps than conventional benzenoid GNRs.[78]

In 2025, Sánchez-Sánchez *et al.* reported a stereospecific on-surface skeletal rearrangement for synthesizing GNRs containing 5/7 rings (Fig. 21c).[169] Using a chiral monomer (**49**) containing a configurationally stable tribenzoannulated cyclooctatetraene (triCOT) unit, linear polymer precursors (**P33**) were first formed on Au(111) *via* Ullmann coupling. Upon adsorption, the polymer chains retained two diastereomeric configurations (concave and convex). Annealing to 625 K triggered cyclodehydrogenation; only the concave segments underwent a skeletal rearrangement mediated by surface Au adatoms, which inserted into the concave C_1–C_2 bond and facilitated its cleavage. This process converted the original octagonal ring into a cyclopenta[*cd*]azulene (755) unit, yielding a non-benzenoid GNR (755-GNR) with a 5/7/5 ring sequence. Quantum mechanics/molecular mechanics (QM/MM) simulations revealed that the rearrangement proceeds through an Au adatom-mediated mechanism, with the lowest activation barrier of 1.52 eV for cleaving the concave C_1–C_2 bond. STS measurements on the resulting 755-GNR gave a bandgap of 1.43 eV, which represents the narrowest bandgap reported to date for an all-carbon chevron-like GNR.[169]

In addition to directly employing monomers that contain non-hexagonal ring structural units, the rational design of precursor structures to enable the *in situ* generation of non-benzenoid topological defects during surface polymerization and cyclodehydrogenation also facilitates the direct construction of GNRs incorporating 5-, 7-, or 8-membered rings. In 2024, Yu *et al.* reported the synthesis of C-5-GNRs (Fig. 22a) by employing precursor (**50**) with a brominated anthracene core,[172] which on Au(111) first underwent Ullmann coupling at 473 K to form polymeric chains (**P34**) with both *trans* and *cis* linkages, followed by cyclodehydrogenation at 623 K. The *trans*-configured chains acted as key intermediates, which engaged in radical-mediated coupling *via* triangulene-like transition states. This process led to the sequential formation of 5-membered rings and cove edges, ultimately yielding a ribbon structure with periodic non-benzenoid units along the zigzag edges. DFT calculations combined with STS measurements reveal that C-5-GNRs exhibit a nontrivial topological band structure, as described by the Su–Schrieffer–Heeger (SSH) model. The DFT-calculated band structure shows two bands (CB and VB) near the Fermi level, with the intercell hopping amplitude being significantly larger than the intracell hopping. This hopping imbalance, together with the calculated intercellular Zak phase, confirms the nontrivial topological nature of C-5-GNRs.[172]

In a related approach, Zhu *et al.* achieved the bottom-up synthesis of GNRs embedded with non-alternant 5/7/5 ring motifs (Fig. 22b). Using a bromomethyl-functionalized precursor (**51**), a surface-assisted Wurtz-type coupling was performed on Au(111), leading to the formation of linear polymer chains (**P35**, **P36**). Subsequent annealing at 773 K induced complete cyclodehydrogenation and planarization, resulting in fully conjugated GNRs with integrated 5/7/5 units. The *trans* isomer exhibits helical symmetry with the 5/7/5 units aligned periodically along the ribbon, whereas the *cis* isomer adopts a Janus-type edge structure that compensates the mismatch between zigzag and armchair segments. DFT calculations show that the *trans*-575GNR has a bandgap of 2.14 eV, while the *cis*-575GNR exhibits a larger bandgap of 2.84 eV with flat-band features for both valence and conduction bands, giving a high density of states that matches the sharp peaks in dI/dV spectra. Notably, the antiaromatic character of the embedded 5/7/5 cores is stabilized by the surrounding aromatic hexagonal rings, contributing to the overall structural integrity.[76]

In 2021, Gottfried *et al.* demonstrated a notable example of GNRs containing 4-, 6-, and 8-membered rings through the synthesis of biphenylene-network GNRs with unique non-benzenoid topology *via* an on-surface strategy (Fig. 22c).[173] They first prepared the key precursor, 4,4′-dibromo-2,2′,2′′,5,5′,5′′-hexafluoro-1,1′:4′,1′′-terphenyl, DHTP (**52**). This monomer incorporates bromine atoms for linear polymerization and fluorine atoms that guide the subsequent cyclization. On the Au(111) surface, DHTP initially polymerized through thermally induced debrominative coupling to form highly ordered linear chains of poly(2,5-difluoro-*para*-phenylene), PFPP (**P37**). Subsequently, at higher temperatures, a specific intermolecular dehydrofluorination (HF-zipping) cyclization occurred between adjacent PFPP chains. This process occurs selectively between a C–H site on one chain and a C–F site on the neighboring chain, thereby avoiding the formation of conventional six-membered benzene rings. Through such a stepwise and selective surface polymerization strategy, a novel sp^2-carbon network consisting of periodic arrays of 4-, 6-, and 8-membered rings was successfully constructed (Fig. 22c). The resulting biphenylene GNRs exhibit distinct electronic properties: their bandgap decreases rapidly with increasing GNR width and displays metallic characteristics at larger widths (Fig. 22c).[173]

Beyond on-surface synthesis, significant progress has also been made in the solution-phase synthesis of non-benzenoid GNRs (Fig. 23).[65,174] In 2024, our group reported the first solution-phase synthesis strategy to construct wave-shaped GNRs (wGNRs) with periodic eight-membered rings embedded in their backbone (Fig. 23a).[65] The synthetic route is centered around a designed diyne monomer (**53**) and a dicyclopenta[*e*,*l*]pyrene-5,11-dione derivative monomer (**54**). Through an efficient A_2B_2-type Diels–Alder cycloaddition polymerization between them, a ladder-type polymer precursor (**P38**) was successfully constructed. Subsequently, a selective Scholl reaction catalyzed by a DDQ/TfOH system was employed to achieve cyclodehydrogenation of the polymer, ultimately yielding fully conjugated wGNRs (Fig. 23a).[65] The uniqueness of this structure stems from the periodically arranged tetraphenylene units (highly twisted eight-membered rings), which cause the entire GNR backbone to adopt a non-planar, wave-like

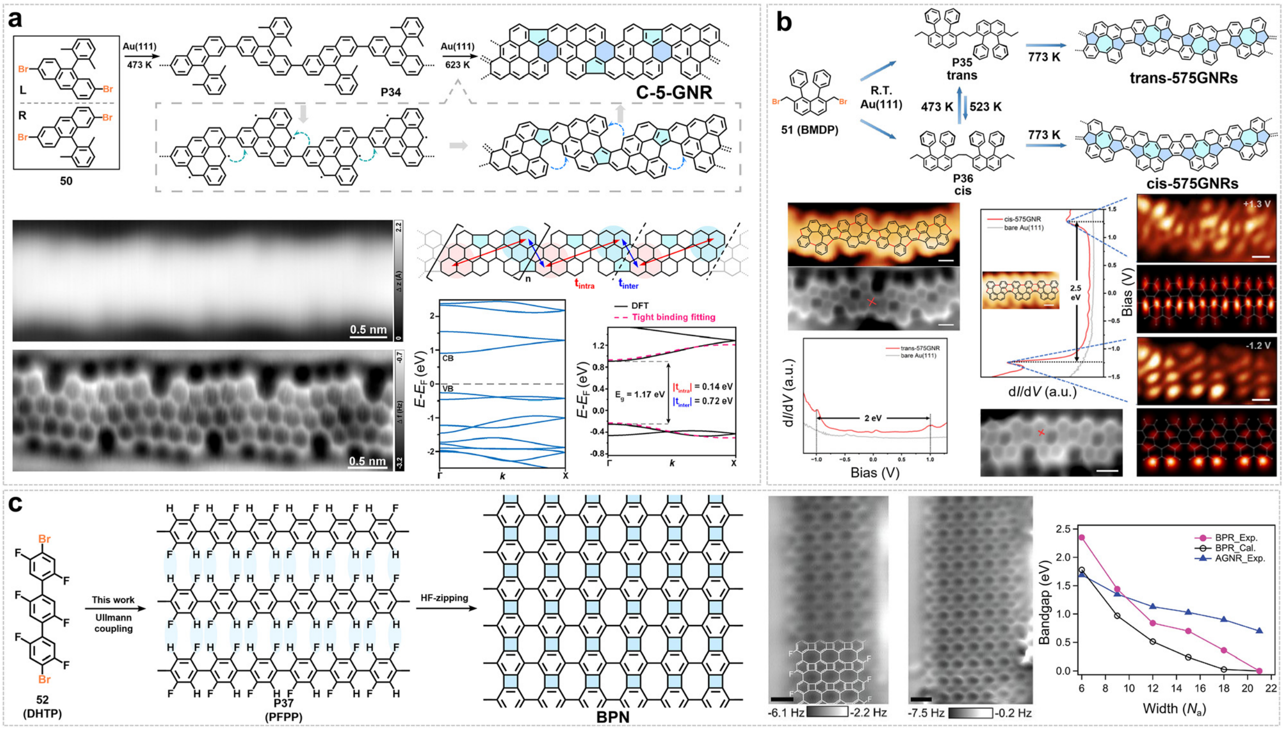

Fig. 22 (a) Synthesis and chemical STM characterization of C-5-GNR, which exhibits a nontrivial topological electronic structure. Reprinted with permission from ref. 172. Copyright 2024, American Chemical Society. (b) Reaction pathways of BMDP on Au(111) leading to *trans*- and *cis*-575GNRs, followed by STM characterization of the structural and electronic properties of the *trans*-575GNR. Reprinted with permission from ref. 76. Copyright 2025, American Chemical Society. (c) Synthesis, STM characterization, and electronic properties of planar nonbenzenoid biphenylene networks. Reprinted with permission from ref. 173. Copyright 2021, American Association for the Advancement of Science.

geometry (Fig. 23a). Owing to this distinctive configuration, the wGNRs exhibit excellent dispersibility (up to 10 mg mL^{-1} in chloroform) and effectively suppressed inter-ribbon π–π stacking, which consequently leads to pronounced PL in solution and an optical bandgap of approximately 2.16 eV. Building on these favorable properties, we successfully fabricated a GNR-based

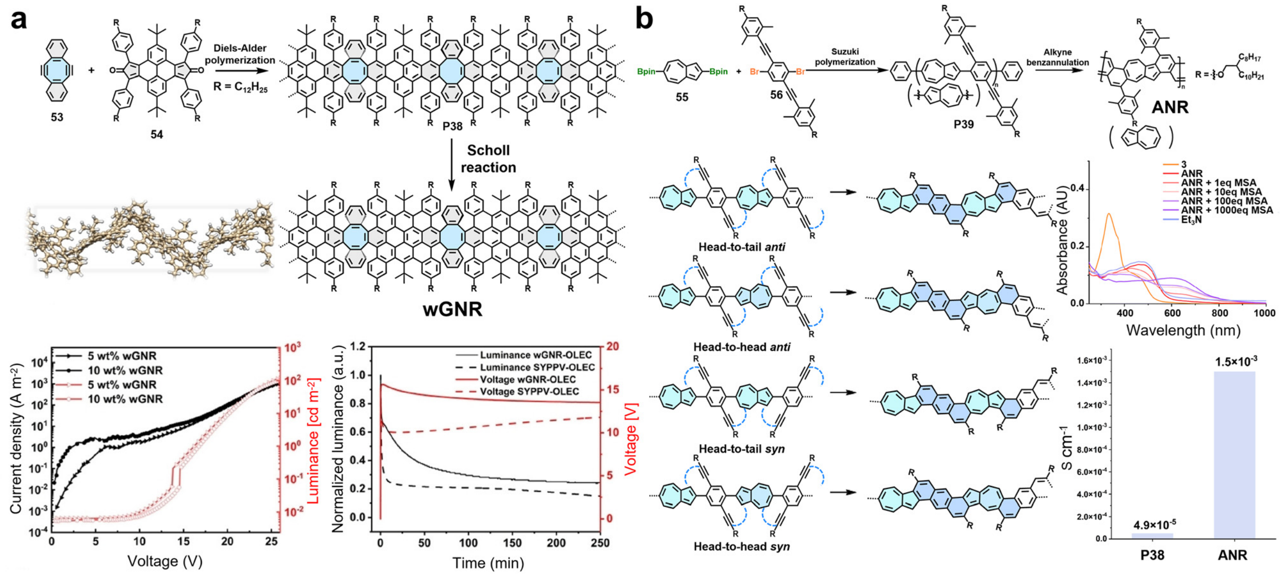

Fig. 23 (a) Synthesis of wGNR and electrochemical properties of wGNR in organic light-emitting cells. Reprinted with permission from ref. 65. Copyright 2024, Wiley-VCH. (b) Synthesis of ANR *via* diverse alkyne benzannulation pathways, with characterization of the optical and electrical properties. The electrical performance was obtained after the sample was exposed to trifluoroacetic acid (TFA) for 5 minutes. Reprinted with permission from ref. 174. Copyright 2021, The Royal Society of Chemistry.

organic light-emitting electrochemical cell by employing wGNR as the emitting layer, achieving a response time of less than 10 seconds (Fig. 23a).[65]

In 2024, Morin *et al.* reported the solution-phase synthesis of non-benzenoid GNRs containing 5/7 rings (named as ANRs) achieved *via* alkyne benzannulation as the key step (Fig. 23b).[174] This work employed a 2,6-disubstituted pyrene unit (**55**) with C_{2v} symmetry as the crucial non-benzenoid building block, which underwent Suzuki–Miyaura polymerization with an alkyne-containing conjugated monomer (**56**) to initially yield a regionally random linear precursor polymer (**P39**). This polymer exhibited good solubility in common organic solvents, primarily owing to the branched alkyl chains introduced as side groups. Subsequently, the polymer underwent cyclization and rigidification *via* a methanesulfonic acid-catalyzed alkyne benzannulation reaction at room temperature, yielding the fully conjugated GNR (Fig. 23b). As the benzannulation could occur at the 1, 3, 5, and 7 positions of the pyrene unit, the final product was a mixture of regioisomers comprising diverse π-conjugated segments (containing five- and seven-membered rings), thereby endowing ANR with a unique non-benzenoid, multi-topological block-conjugated structure (Fig. 23b). The resulting ANR exhibited an optical bandgap of 2.2 eV, which could be further tuned down to 1.7 eV *via* reversible protonation (Fig. 23b). In the film state after protonation doping, ANR demonstrated a conductivity as high as 1.5×10^{-3} S cm^{-1}, significantly outperforming its uncyclized precursor polymer (Fig. 23b).[174]

4.3 Porous GNRs

The introduction of precisely arranged nanoscale pores into sp^2-carbon networks—forming porous GNRs (pGNRs)---constitutes another strategy for engineering their electronic band structures. This selective removal of carbon atoms fundamentally reconstructs the electronic system by simultaneously enhancing quantum confinement, reconfiguring edge states, and modifying topological boundaries and electron-coupling pathways.[96,98,100,175,176] Theoretical studies suggest that pore geometry, size, and superlattice periodicity serve as powerful design parameters, enabling precise tuning of electronic properties such as bandgap, effective carrier mass, and band dispersion.[100,175,177,178] In terms of synthesis strategies, there are three main approaches for introducing well-defined pores into GNRs: first, directly constructing pGNRs through reactions between monomers; second, introducing monomers with pre-existing pore structures to form pores in GNRs based on their inherent architecture; and third, constructing porous structures through the fusion process of adjacent GNRs (Fig. 24).

In 2022, Fasel and we reported the synthesis of pGNRs containing nonplanar [14]annulene pores *via* an on-surface synthesis strategy (Fig. 25a).[179] We designed and synthesized a dibromohexabenzotetracene, DBHBT (**57**) monomer featuring four cove-edges. The monomer was subjected to stepwise thermal annealing on a Au(111) surface: first, dehalogenative aryl–aryl coupling occurred at 200 °C, forming a polymer precursor (**P40**) with rotational freedom, followed by cyclodehydrogenation above 400 °C. However, this step did not fully achieve the intended structural cyclization, resulting in a defective porous GNR in which nonplanar [14]annulene pores were partially formed, accompanied by the generation of five-membered rings (Fig. 25a). Characterization by STM and nc-AFM revealed that the obtained GNR exhibits distinct nonplanar distortion, with hydrogen atoms in the pore region adopting alternating orientations and the edge hexagons displaying a wavy arrangement due to steric repulsion (Fig. 25a).[179]

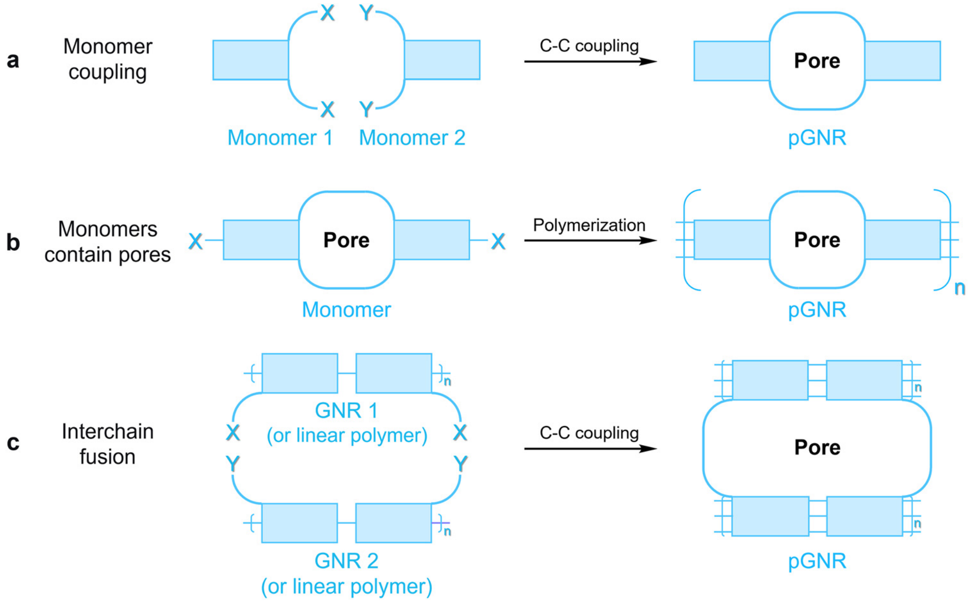

Fig. 24 Three typical strategies for introducing porous structures into GNRs. (a) Direct construction of pGNRs through reactions between special monomers. (b) Introducing monomers with pre-existing pore structures to create pores in GNRs. (c) Constructing pGNRs through the fusion of adjacent GNRs.

In 2022, Wang *et al.* utilized monatomic step edges on an Au(111) surface to assist on-surface synthesis, thereby fabricating 8-AGNRs (DV8-aGNRs) embedded with periodic divacancies and featuring a nonplanar configuration (Fig. 25b).[180] The key precursor, 5,8-dibromopentacene, DBP (**58**), underwent stepwise reactions on Au(111), where the critical cyclodehydrogenation at 720 K at the step edges enabled the efficient formation of divacancies. This process underscores the catalytic role of step edges and Au adatoms in reducing energy barriers. The resulting DV8-aGNR exhibits a nonplanar backbone due to asymmetrically distributed divacancies, leading to a significantly widened bandgap of ∼3.36 eV (much larger than that of pristine 8-aGNR, ∼1.00 eV). STS resolves the valence band at −1.26 V and the conduction band at 2.10 V, and d*I*/d*V* maps reveal that the frontier orbitals are reshaped into wiggling patterns along the zigzag direction, in contrast to the linear states observed on the armchair edges (Fig. 25b). In 2024, Gottfried *et al.* synthesized long porous 12-AGNRs on Au(111) using 7,10-dibromo-1,4-diphenyltriphenylene, DBDT (**59**) *via* stepwise Ullmann coupling and cyclodehydrogenation (Fig. 25c).[96] This process yields a periodic array of 18-membered nanopores, which enlarges the experimental bandgap to ∼3.3 eV—far exceeding that of non-porous 12-AGNRs (∼1.13 eV). This effect is well described by a "sub-band" model, where the electronic structure is governed by the narrowest continuous graphene strip confined between pores. The functionality of pGNRs can be further modulated through structural fusion and heteroatom doping. Laterally fused pGNRs form extended nanoporous graphene sheets with tunable junction topologies (graphene-type or biphenylene-type), which correspondingly exhibit direct or indirect bandgap characteristics (Fig. 25d).[100] Additionally, Meyer *et al.* synthesized nitrogen-doped pGNRs (N-GNRs) on Ag(111) *via* surface-assisted Ullmann coupling of a brominated tetrabenzophenazine derivative. The resulting structure features symmetric nitrogen atoms around each pore, forming a periodic donor–acceptor architecture with a bandgap of ∼2.7 eV and spatially separated frontier orbitals.[97]

In contrast to the strategy of *in situ* pore construction through polymerization reactions, the use of monomers containing pre-formed pore motifs offers an effective route for directly "embedding" pores into GNRs.[181] In 2023, our team

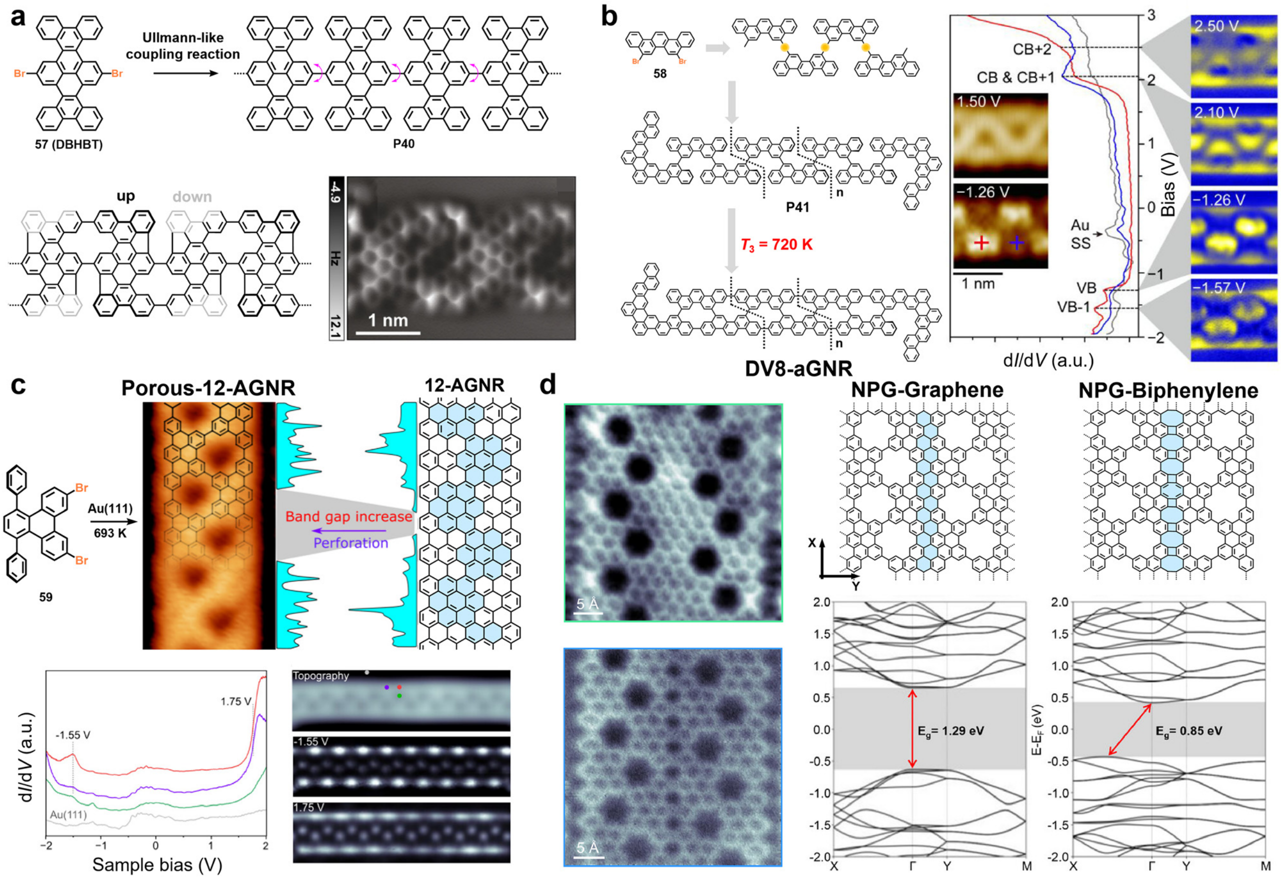

Fig. 25 (a) On-surface synthesis and STM characterization of GNRs incorporating nonplanar [14]annulene pores and five-membered rings. Reprinted with permission from ref. 179. Copyright 2022, Wiley-VCH. (b) Schematic representation of the stepwise bottom-up synthesis of the DV8-aGNR on Au(111) and electronic properties of the DV8-aGNR. Reprinted with permission from ref. 180. Copyright 2022, American Chemical Society. (c) Synthesis and characterization of the porous 12-atom-wide AGNRs and their electronic properties. Reprinted with permission from ref. 96. Copyright 2024, American Chemical Society. (d) Structural models and DFT calculated band structures of NPG with a graphene-type fusion pattern, and NPG with a biphenylene-type fusion pattern. Reprinted with permission from ref. 100. Copyright 2025, Wiley-VCH.

reported the first bottom-up solution-phase synthesis of pGNRs with precisely defined nanopore structures by employing such pore-containing precursors (Fig. 26a).[181] The core of this synthetic strategy lies in the design and preparation of a novel macrocyclic monomer, which contains a pre-embedded hexagonal nanopore composed of phenanthrene units. Through an A_2B_2-type Suzuki polymerization, this macrocyclic monomer (**60**) efficiently copolymerizes with a dihalogenated monomer (**61**), yielding a linear polyphenylene precursor polymer. Subsequently, the polymer undergoes a Scholl reaction to afford the target pGNRs (Fig. 26a). The uniqueness of this synthetic route lies in the precise molecular-level integration of periodic, uniformly sized nanopores (carbon-to-carbon diameter ≈ 0.6 nm, pore-to-pore distance ≈ 1.7 nm) into the GNR backbone while

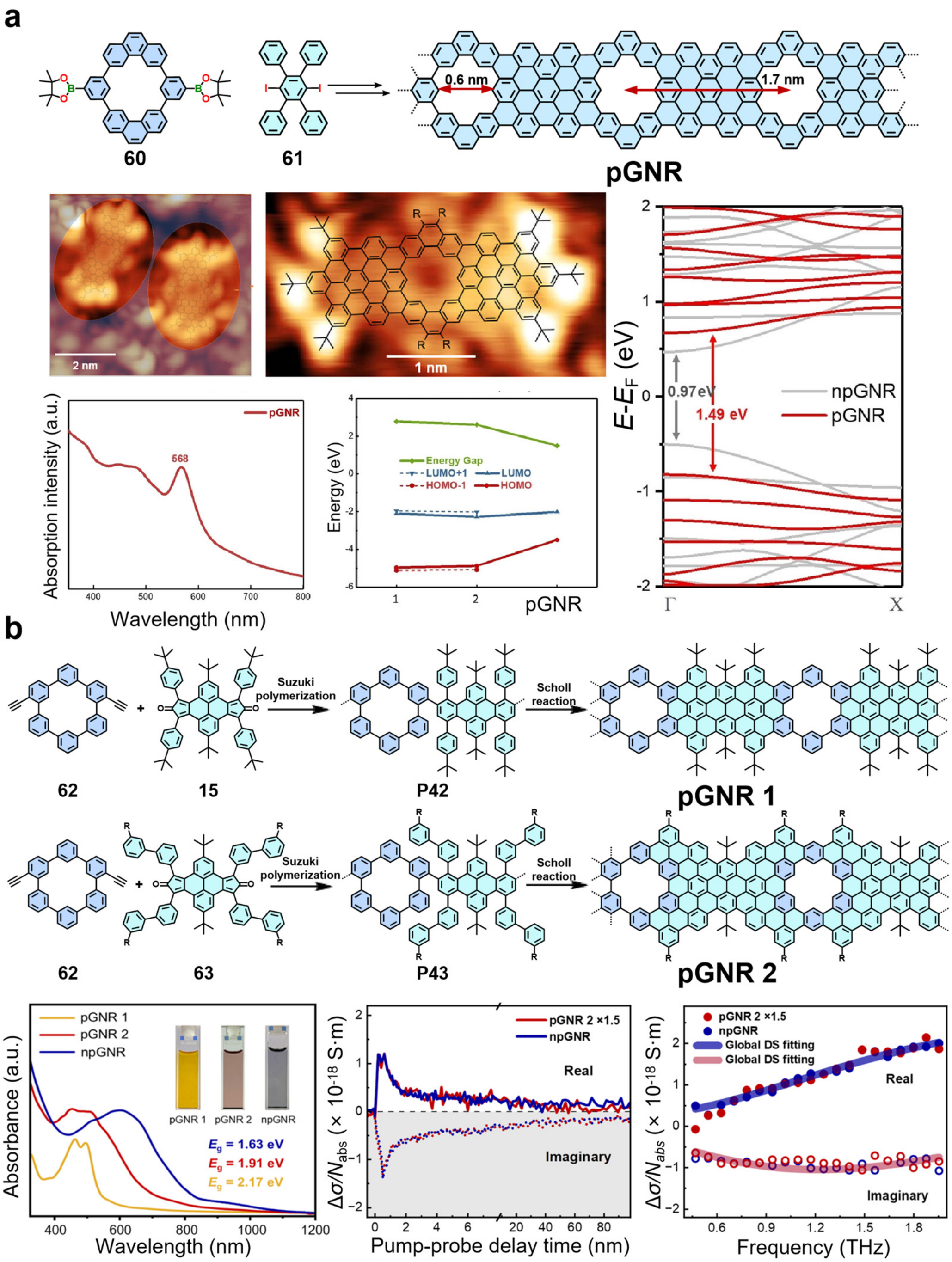

Fig. 26 (a) Solution synthesis of pGNRs, with STM imaging of model compound, UV/Vis absorption in THF, and calculated electronic structure. Reprinted with permission from ref. 181. Copyright 2023, Wiley-VCH. (b) Synthesis and UV-vis absorption spectra of pGNR 1, pGNR 2, and npGNR, as well as time-resolved and frequency-resolved complex terahertz photoconductivity of pGNR 2 and npGNR. Reprinted with permission from ref. 182. Copyright 2024, Wiley-VCH.

maintaining the overall continuity of the conjugated framework (Fig. 26a). The resulting pGNRs exhibit a distinctive structure in which the periodic nanopores significantly reduce intermolecular π–π stacking, thereby imparting excellent solution processability. Compared to non-porous GNRs of similar width, the nanoporous architecture effectively modulates the electronic energy levels, leading to a notably enlarged bandgap of approximately 2.0 eV (Fig. 26a).[181]

In 2026, our group further synthesized two novel types of pGNRs along with a non-porous GNR (npGNR) as a reference *via* A_2B_2-type Diels–Alder polymerization followed by Scholl cyclodehydrogenation (Fig. 26b).[182] A designed macrocyclic monomer (**62**) containing diethynyl-substituted cycloparaphenylene units was copolymerized with a cyclopentadienone derivative (**15**, **63**), affording a high-molecular-weight linear polyphenylene precursor (**P42**, **P43**). Subsequent $FeCl_3$-catalyzed Scholl reaction efficiently transformed this precursor in a one-pot cyclodehydrogenation step into fully conjugated pGNRs (Fig. 26b). The obtained pGNRs feature a periodic array of precisely sized [18]annulene-type nanopores (pore diameter: ~6 Å), creating a unique topology in which gulf edges alternate with the nanopores. This structural motif not only significantly enhances the dispersibility of the GNRs in organic solvents but also markedly modulates their electronic band structure. Spectroscopic studies revealed that the introduction of nanopores leads to an optical band-gap enlargement of 0.28 eV for pGNR-2 (1.91 eV) compared to the width-matched npGNR (1.63 eV) (Fig. 26b). Further time-resolved THz spectroscopy analysis indicated that the nanopores do not notably increase carrier scattering; instead, they induce a flattening of the bands, which increases the effective mass of the charge carriers (Fig. 26b). Consequently, the μ_{DC} ($\mu_{DC} = \mu(1 + c)$) of pGNR-2 (~27 $cm^2\ V^{-1}\ s^{-1}$) is lower than that of the npGNR (~40 $cm^2\ V^{-1}\ s^{-1}$). Through precise synthetic chemistry, this work systematically elucidates the influence of nanopore architecture on the electronic properties and charge-transport behavior of GNRs.[182]

pGNRs can be constructed through the lateral fusion of polymer chains or pre-formed GNRs (Fig. 27). In 2020, Yu *et al.* achieved hierarchically precise control over the Ullmann coupling reaction through a stepwise on-surface synthesis strategy by exploiting the difference in reactivity between two halogens (Br and Cl) on a U-shaped precursor, thereby successfully preparing two pGNRs with distinct structures.[99] On Au(111), sequential Ullmann coupling and cyclodehydrogenation, guided by the distinct cleavage temperatures of the two halogens, first produce linear (**P44**) or cyclic (**65**) polymeric precursors. Subsequent dechlorination, concurrent with cyclodehydrogenation, drives inter-chain lateral fusion while circumventing steric hindrance,

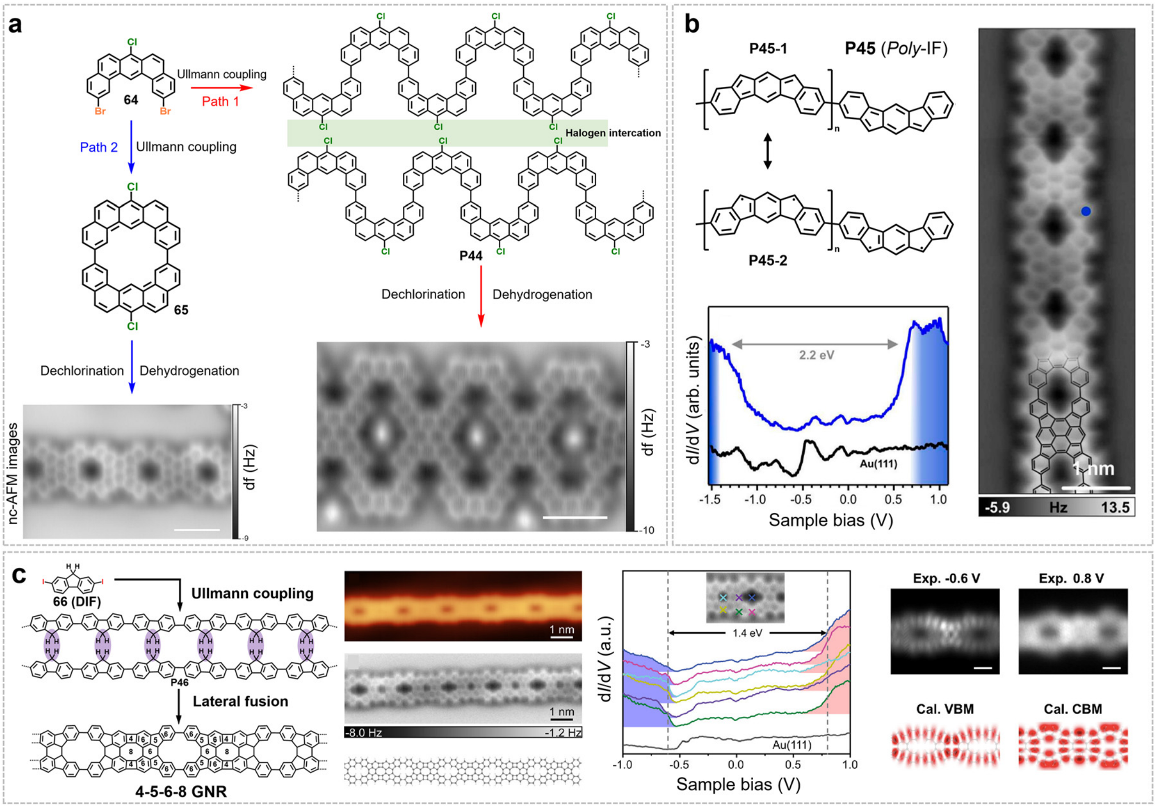

Fig. 27 (a) Synthetic hierarchical path for the fabrication of PGNRs and the corresponding AFM images. Reprinted with permission from ref. 99. Copyright 2020, American Chemical Society. (b) pGNRs formed *via* lateral fusion of poly-IF on Au(111), the nc-AFM image and d*I*/d*V* spectrum of the pGNRs. Reprinted with permission from ref. 183. Copyright 2019, American Chemical Society. (c) On-surface reactions toward the formation of the pGNR composed of 4-5-6-8-membered rings and the corresponding STM and nc-AFM images. Reprinted with permission from ref. 184. Copyright 2023, American Chemical Society.

yielding pGNRs with alternating 4-ZGNR segments connected by porous units (Fig. 27a). The resulting structure, featuring purely zigzag edges and an etched topology, exhibits a bandgap of ~2.2 eV—significantly wider than pristine ZGNRs—with STS confirming localized states at pore edges.[99,183] In 2019, Fasel and coworkers achieved the on-surface polymerization of the antiaromatic, open-shell indeno[2,1-*b*]fluorene (IF) unit, followed by lateral fusion to form non-benzenoid pGNRs (Fig. 27b). Starting from a dibromo-dimethyl-terphenyl monomer, stepwise reactions on Au(111) yielded a poly-IF chain (**P45**). Annealing induced inter-chain dehydrogenative coupling, producing a uniform porous architecture corresponding to tetraindenopyrene. These pGNRs retain a narrow bandgap (~2.2 eV) and exhibit distinctive electronic and spin properties inherited from the IF unit's antiaromatic and diradical character. In 2023, Xu *et al.* synthesized a novel 4-5-6-8 GNR containing 4-, 5-, 6-, and 8-membered rings (Fig. 27c).[184] Using 2,7-diiodo-9*H*-fluorene, DIF (**66**) on Au(111), dehalogenative coupling first formed polyfluorene chains (**P46**). High-temperature annealing then triggered "face-to-face" dehydrogenative C–C coupling between adjacent chains, leading to lateral fusion and the precise formation of the multi-polygonal ribbon. Bond-resolved STM/nc-AFM confirmed the periodic arrangement of four-, five-, six- and eight-membered rings. The GNR shows a semiconducting gap of ~1.4 eV on Au(111), with the valence band maximum at −0.6 V and the conduction band minimum at 0.8 V. d*I*/d*V* maps reveal that the local density of states is maximized over the tetragonal and octagonal rings, consistent with DFT-simulated local density of states (LDOS) at the band onsets (Fig. 27c).[184]

In 2018, Sinitskii *et al.* reported the on-surface synthesis of phenyl-functionalized GNRs (mGNRs) and systematically investigated the influence of edge phenyl substitution on the assembly behavior, electronic properties, and subsequent fusion-based construction of pGNRs (Fig. 28a).[185] Starting from the precursor 2,3-di([1,1′-biphenyl]-4-yl)-6,11-dibromo-1,4-diphenyltriphenylene, debrominative coupling was initiated on the Au(111) surface by annealing at 250 °C to form polymer chains (**P47**). A key feature of this polymerization stage is that the functionalized phenyl side chains guide adjacent polymer chains into ordered parallel alignment through π–π interactions, significantly enhancing the length and regularity of the polymer chains. Subsequent high-temperature cyclodehydrogenation at 440 °C yielded fully planarized phenyl-modified mGNRs. The obtained mGNRs exhibit both structural inheritance and uniqueness: while retaining the backbone of the chevron GNR, the introduction of lateral phenyl groups not only enables controllable assembly during the on-surface polymerization process but also provides two possible reaction sites for subsequent lateral fusion between GNRs. By regulating the fusion pathways, pGNRs with different sizes and shapes can be obtained, expanding the structural diversity of GNR-based nanostructures (Fig. 28a).[185] In 2018, Mugarza *et al.* proposed a hierarchically controlled synthesis strategy using 2,2′-di([1,1′-biphenyl]-4-yl)-10,10′-dibromo-9,9′-bianthracene, DP-DBBA (**67**) as a precursor to progressively construct a network of laterally connected pGNRs on an Au(111) surface *via* a three-step reaction sequence (Fig. 28b).[177] The process includes: Ullmann coupling (200 °C) to form polymer chains (**P48**), cyclodehydrogenation (400 °C) to generate width-tunable 7–13 AGNRs, and dehydrogenative cross-coupling (450 °C) to achieve lateral linkage of the GNRs. This ultimately yields a GNR network with a highly ordered porous superstructure, featuring pore dimensions of approximately 0.4 nm × 0.9 nm and a density as high as 4.8 × 10^5 pores per mm^2. This porous GNR network exhibits an anisotropic electronic structure: the

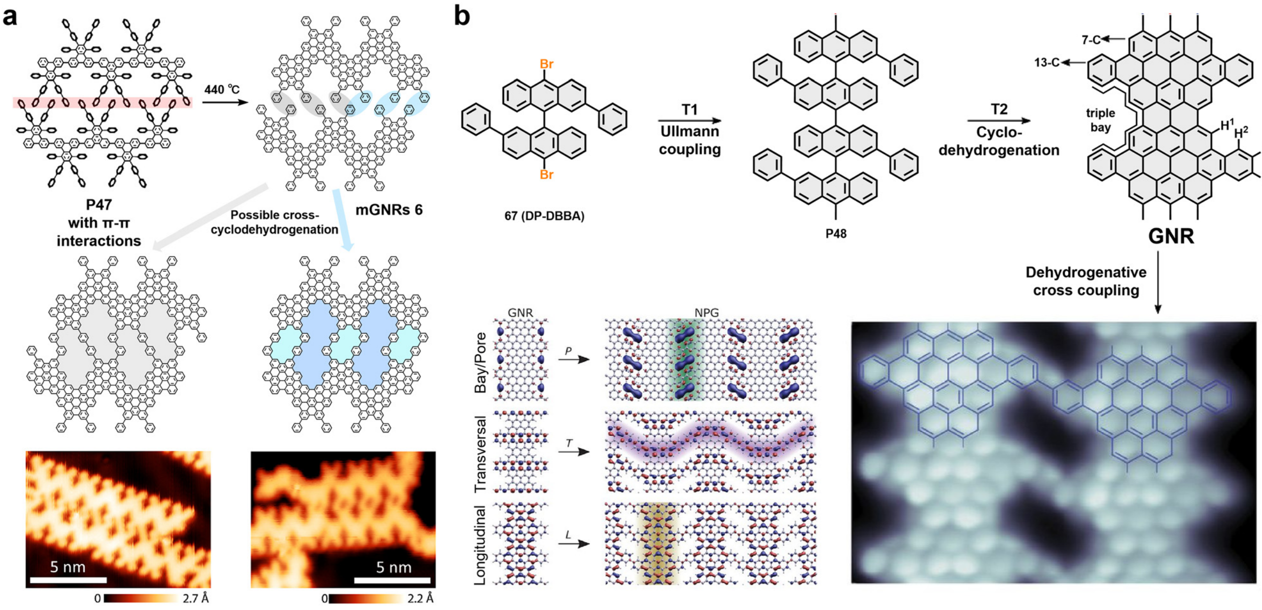

Fig. 28 (a) Lateral fusion of mGNRs into graphene nanopores and their STM image. Reprinted with permission from ref. 185. Copyright 2018, American Chemical Society. (b) Schematic illustration of the hierarchical synthesis of NPG and the corresponding wave functions of GNR and NPG at Γ. Reprinted with permission from ref. 177. Copyright 2018, American Association for the Advancement of Science.

longitudinal bands (L-bands) along the GNR direction possess a bandgap of about 1.0 eV, while the transverse bands (T-bands) form one-dimensional conduction channels in the direction perpendicular to the GNRs. Additionally, localized pore bands (P-bands) emerge within the pore cavities. The coexistence of these multiple bands enables purely longitudinal transport (along a single GNR direction) at low bias and bidirectional conduction (across neighboring GNRs) at higher energies, providing a unique material platform based on the porous GNR network for multifunctional device applications.[177,178]

4.4 GNRs with helical structures

In Section 3.1.2, we noted that introducing nonplanar configurations, such as cove-edge and fjord-edge, in GNRs can induce localized twisting and bending *via* steric hindrance from C–H bonds, thereby leading to nonplanar geometries and significantly affecting their band structures and charge-transport properties.[47,61,62,64,74] However, such structural changes are typically confined to the edge regions, primarily resulting in ''edge-helical'' distortions, in which nonplanarity is relatively localized and insufficient to exert a more profound influence on the overall properties of the GNRs. In contrast to strategies based on edge reconstruction or localized chemical modification, this section will focus on GNRs in which more extensive and pronounced geometric deformations are introduced into the GNR backbone. In these GNRs, the carbon skeleton undergoes substantial, global structural transformation, redistributing the bond lengths and angles of C–C bonds across the entire structure, thereby forming ''backbone-helical'' twisted or spiral conformations and introducing lattice distortions on a broader scale.[101–103,186,187] Studies have shown that in such GNRs with curved or helical backbones, the overall geometric deformation not only influences their dispersion behavior in solution but also significantly modulates their bandgaps and can even induce novel properties such as magnetism or topological electronic states. This opens up new dimensions for the property tuning of GNRs.

Systematic theoretical studies indicate that such specially structured GNRs possess a series of tunable physical properties.[187–192] For instance, by adjusting the pitch of helical GNRs, continuous modulation of interlayer coupling can be achieved, thereby driving a metal-semiconductor electronic phase transition, which offers a flexibly tunable parameter space for band engineering.[192] Furthermore, introducing asymmetric polar units (*e.g.*, azulene moieties) into the helical backbone can break the structural centrosymmetry, thereby significantly enhancing their second-order nonlinear optical response.[187] Additionally, these twisted GNRs exhibit excellent electrical and energy-conversion performance: their charge-transport behavior can be effectively regulated by a transverse electric field, enabling a high on/off ratio in field-effect devices; meanwhile, the synergistic effect of geometric twisting and vacancy defects could improve the thermoelectric conversion efficiency of GNRs.[191]

The above intriguing prospects have motivated substantial experimental efforts to synthesize well-defined twisted or helical GNRs. Certain progress has been made in synthesizing such non-planar structures in recent years, allowing for direct experimental validation of their predicted properties. In 2017, Morin's team reported a solution-phase synthetic strategy using chlorinated poly-*meta*-phenylene precursors (**68**), which produced structurally helical GNRs through regioselective photochemical cyclodehydrochlorination (Fig. 29a).[186] The resulting GNRs adopt a helical topology resembling that of multiple helicenes and can be viewed as synthetic graphene Riemann surfaces. Raman spectroscopy reveals splitting of the G-band, a feature attributed to unique vibrational modes induced by the helical conformation (Fig. 29a). These helical GNRs exhibit a relatively large bandgap of 2.15 eV (Fig. 29a) and show pronounced visible-light emission both in solution and in the solid state, with their optical properties closely linked to intramolecular π-stacking effects promoted by the helical structure.[186] Furthermore, using a similar approach, they synthesized both linear and helical GNRs containing electron-rich pyrrole units (L-PyGNR and H-PyGNR) (Fig. 29b) in 2021.[101] The helical architecture (H-PyGNR) was found to influence the properties in multiple ways. Compared with the linear analogue, the helical conformation contracts the backbone, reducing the hydrodynamic radius and apparent molecular weight in solution. Although the solution absorption spectra are similar, H-PyGNR displays a larger red-shift and broader low-energy tail in the solid state, indicating stronger π–π stacking (Fig. 29b). Electrochemical measurements and theoretical calculations show that the helical structure possesses slightly higher HOMO/LUMO energy levels and a larger bandgap, resulting from reduced π-orbital overlap due to the twisted conformation.[101]

In 2022, Du *et al.* reported the synthesis of a helical GNR (referred to as CNS) with a Riemann surface structure (Fig. 29c).[102] First, through a palladium-catalyzed Suzuki coupling reaction, a hexaphenylbenzene derivative bearing boronate groups (**69**) was copolymerized with a biphenyl linker unit containing *ortho*-bromo substituents (**70**) to yield a helical polyphenylene precursor (**P52**) (Fig. 29c). Subsequently, a Scholl reaction mediated by DDQ/TfOH enabled intramolecular cyclodehydrogenation, ultimately constructing a three-dimensional fully π-conjugated GNR with continuous helical topology (Fig. 29c). The key to this synthetic route lies in the synergistic induction of the helical structure through steric hindrance and π-extension effects, achieved by utilizing rigid hexaphenylbenzene units along with *ortho*-substituted linkers. The resulting CNS exhibits a unique single-stranded helical morphology, with a pitch of about 0.41 nm and a diameter of about 2.7 nm, displaying a continuously twisted topology analogous to a Riemann surface. This structure was directly visualized and precisely resolved *via* low-dose integrated differential phase-contrast scanning transmission electron microscopy (iDPC-STEM) (Fig. 29c). In terms of properties, CNS shows a narrow optical bandgap (≈1.97 eV) and intense red PL (Fig. 29c), while the strain-induced localization of π-electrons within its helical architecture endows it with high spin density and paramagnetic response, exhibiting complex magnetic ordering behavior at low temperatures (Fig. 29c).[102] This work not only provides a novel approach for synthesizing helical topological carbon nanostructures but also demonstrates the potential of non-planar π-extended systems for simultaneously tuning optoelectronic and magnetic properties. Following the same strategy, they further synthesized

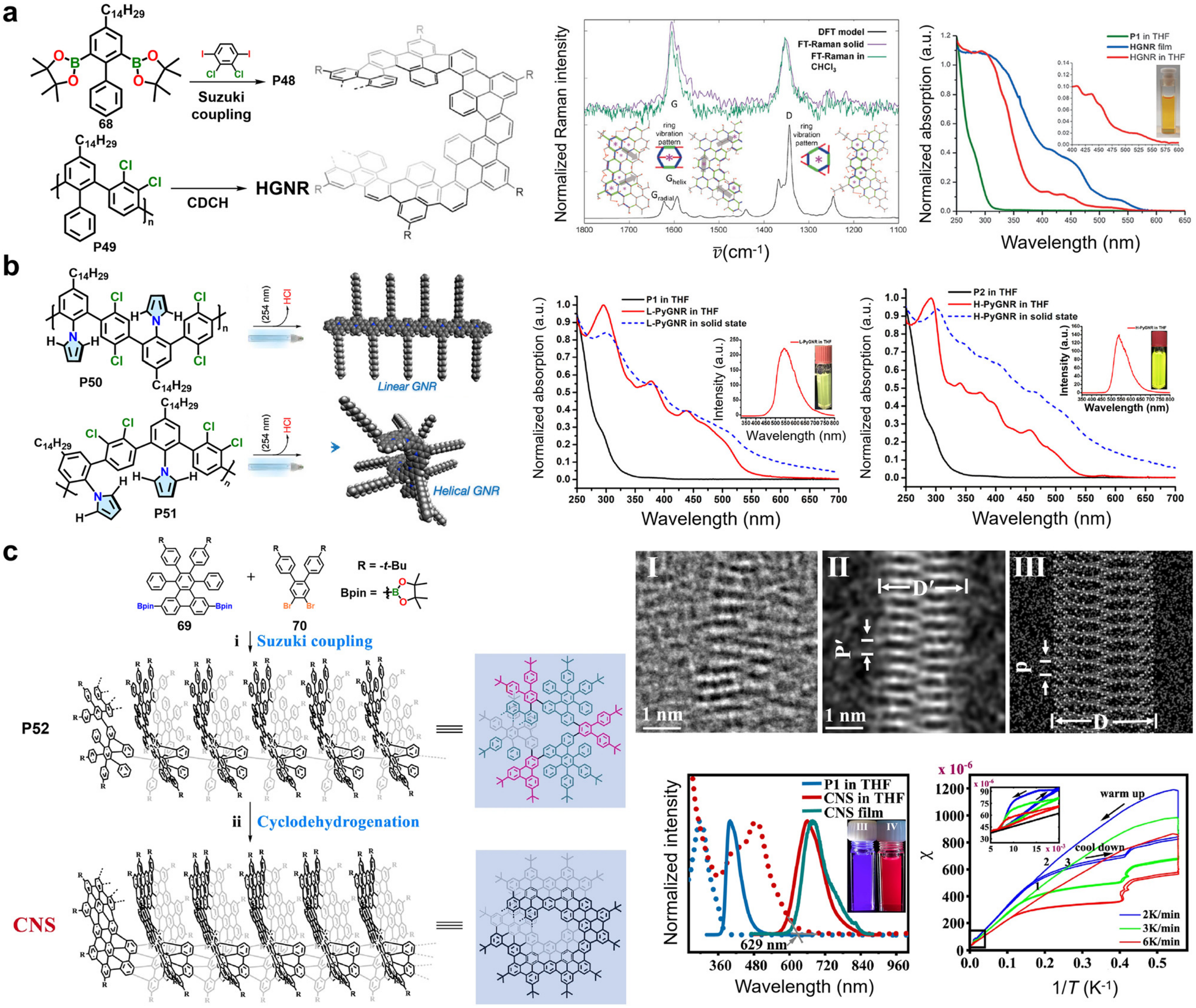

Fig. 29 (a) Synthesis of the helical GNR *via* cyclodehydrochlorination, with characterization by Raman spectroscopy and UV/Vis absorption spectroscopy. Reprinted with permission from ref. 186. Copyright 2017, Wiley-VCH. (b) Synthesis of L-PyGNR and HPyGNR *via* cyclodehydrochlorination, with their UV-vis/PL spectra. Reprinted with permission from ref. 101. Copyright 2021, American Chemical Society. (c) Synthesis, structural characterization, optical and magnetic properties of a three-dimensional fully π-extended curved single-stranded CNS. Reprinted with permission from ref. 102. Copyright 2022, Springer Nature.

nitrogen-doped helical GNRs (N-CNS) in 2023.[193] The synthesis involved two rationally designed monomers: one constructed from 5-bromopyrimidine *via* Sonogashira coupling and Diels–Alder reactions to introduce nitrogen atoms, and the other bearing two *ortho*-boryl groups and *tert*-butyl substituents to enhance solubility. The resulting helical structure of N-CNS, with a pitch of ≈0.40 nm and a width of ≈2.4 nm, was directly resolved by low-dose iDPC-STEM. N-CNS features broad visible-light absorption, a narrow bandgap (∼1.85 eV), and paramagnetic behavior, serving as an efficient metal-free photocatalyst that achieves excellent hydrogen evolution activity (up to 190.2 μmol g^{-1} h^{-1}) under visible light and performs various photoredox organic transformations with good stability and application potential.[193]

Despite advances in helical GNRs in recent years, their controlled synthesis remains a critical challenge. The foremost challenge lies in the concurrent realization of a long-range ordered helical topology while maintaining atomic-scale structural fidelity. Furthermore, the kinetic stability of the helical conformation, along with complex solvent effects, imposes more stringent thermodynamic and kinetic demands on the design of synthetic pathways. Although synthesis strategies guided by steric hindrance have been developed, significant difficulties remain in precisely controlling helical parameters such as pitch and diameter. Concurrently, the characterization of helical GNRs also presents significant challenges: while techniques such as iDPC-STEM enable direct imaging of helical morphology, current methods still have limitations in acquiring atomic-level structural information—including bond-length and angle distributions, dynamic conformational evolution, and local defect characteristics.

5. Heterostructure engineering in GNRs

In the previous sections, we discussed strategies for tuning the properties of GNRs by designing their edge and backbone structures. Nevertheless, the GNRs obtained *via* these strategies typically exhibit uniform structures, resulting in limited bandgap tunability and a lack of spatial electronic modulation. To overcome these constraints, a common approach in semiconductors is to create heterojunctions—coupling materials with distinct electronic properties to realign bands and redistribute carriers at the interface.[194–197] This strategy extends beyond single materials and enables advanced electronic tuning. Inspired by semiconductor heterojunctions, GNR heterojunctions—formed by covalently fusing GNR segments with distinct electronic properties—have gained significant interest.[83,198–204] Synthesized *via* copolymerization, sequential polymerization, and post-modification (Fig. 30b), they exhibit atomically precise interfaces that introduce tunable band structures, making them promising for exploring quantum and spintronic phenomena.[80–82,84,85,205–209]

The alignment of energy bands at the heterojunction interface is a key physical parameter determining carrier transport behavior.[195,196] Based on the band alignment, GNR heterostructures can be classified into the following main types: type I heterojunctions (straddling alignment), where the bandgap of one GNR segment lies entirely within that of the other, with both the VBM and CBM located in the same segment; type II heterojunctions (staggered alignment), in which the band edges of the two segments are offset—with the VBM of one segment higher and the CBM lower than those of the other; and type III heterojunctions (broken-gap alignment), where the bandgaps of the two segments are completely offset, with the CBM of one segment even lower than the VBM of the other (Fig. 30a). These different band alignments lead to significant differences in the electronic properties of GNR heterojunctions. Generally, type I heterojunctions are well-suited for optical and light-emitting devices due to their effective exciton confinement. Type II heterojunctions, which promote spatial separation of photogenerated carriers, are highly regarded for applications in photocatalysis and photovoltaics. In contrast, type III heterojunctions, though unfavorable for carrier separation and thus limited in optoelectronic applications, exhibit unique broken-gap characteristics that show potential in quantum tunneling-based and other non-classical electronic devices. Currently, research on type III heterojunctions remains relatively limited.

5.1 Synthetic strategy for GNR heterojunction

5.1.1 Copolymerization strategy. The most straightforward approach to constructing GNR heterojunctions is through copolymerization of two or more monomers. Due to the challenges in directly characterizing solution-synthesized GNRs, such copolymerization primarily employs on-surface synthesis.[80,106,207,209,210] A typical process involves depositing monomers onto an Au(111) substrate under ultra-high vacuum, followed by thermally initiated radical polymerization and final cyclodehydrogenation. Although the synthesis conditions can be carefully optimized, for example, by tuning the monomer feed ratio and modulating the relative reactivity of different monomers, and nearly all surface-synthesized GNRs can form heterostructures in this manner, affording a wide variety of heterojunction architectures. This approach typically yields copolymers with random statistical composition and limited structural control. As a result, only locally ordered heterojunction segments possess substantial research value.

Width-modulated GNR heterojunctions can be fabricated by copolymerizing precursor monomers of GNRs with different widths. Among them, AGNRs, whose electronic band structure is highly sensitive to their width, are commonly employed to

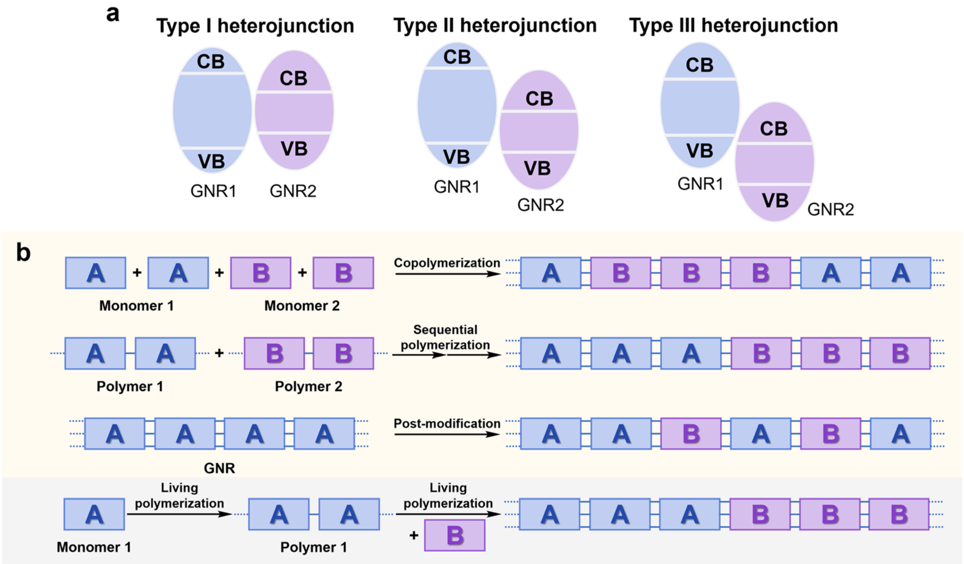

Fig. 30 (a) Alignment of energy bands at the heterojunction interface. (b) Schematic of three representative synthesis strategies for GNR heterojunctions. The first three strategies are primarily implemented through surface synthesis, while the last strategy is achieved through solution synthesis.

construct such width-modulated heterojunctions. Taking the 7–13 AGNR heterojunction as an example, its synthesis is achieved by Crommie *et al.* in 2015 through a two-step annealing process on an Au(111) surface (Fig. 31a).[106] In 2015, Crommie *et al.* completed a classic work. First, monomers of N = 7 (**71**) and N = 13 (**72**) AGNRs are deposited onto the substrate at room temperature under UHV. Subsequently, annealing at 470 K for 10 minutes cleaves the C–Br bonds,

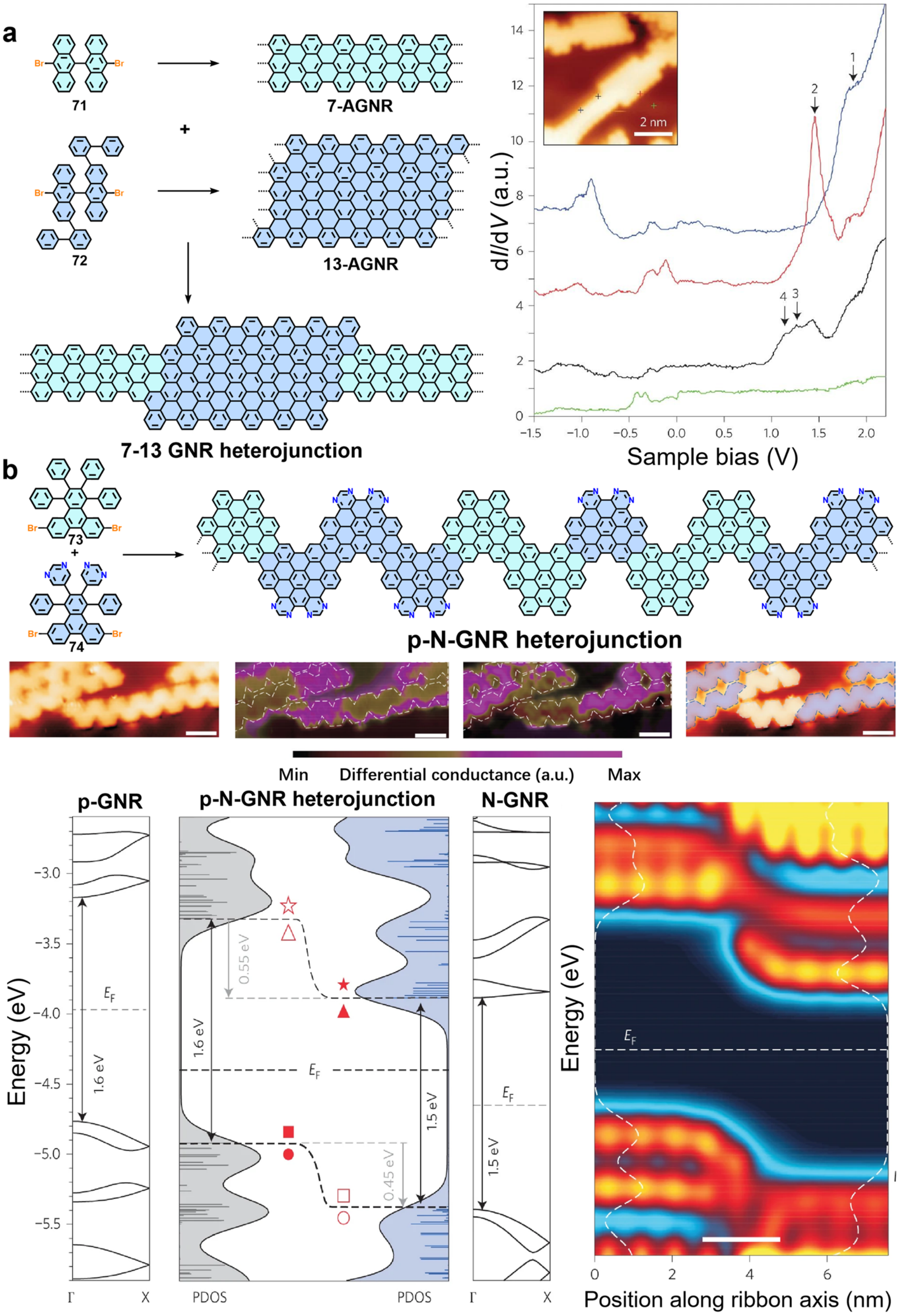

Fig. 31 (a) Synthesis of 7–13 GNR heterojunctions and the STS spectroscopy of their electronic structure. Reprinted with permission from ref. 106. Copyright 2015, Springer Nature. (b) Fabrication and identification of p-N-GNR heterojunctions as well as calculated results for them, showing the band structures of p-GNR and N-GNR, the PDOS of each segment, and the measured LDOS across the junction. Reprinted with permission from ref. 80. Copyright 2014, Springer Nature.

and the resulting biradical intermediates couple on the surface to form linear polymers. Finally, annealing at 670 K for 10 minutes induces cyclodehydrogenation, yielding the target heterojunction (Fig. 31a). Although both 7-AGNR and 13-AGNR belong to the $N = 3p + 1$ family, 13-AGNR exhibits a smaller bandgap. STS measurements show that the CBM and VBM of 7-AGNR are +1.86 V and −0.90 V, respectively, whereas those of 13-AGNR are +1.45 V and −0.12 V. Since the entire band structure of 13-AGNR lies completely within the bandgap of 7-AGNR, they form a typical type-I heterojunction band alignment (Fig. 31a).[106]

Heteroatom-doped GNR heterojunctions can be synthesized by copolymerizing pure oligophenylene monomers with their heterocycle-substituted counterparts (Fig. 31b). For instance, using 6,11-dibromo-1,2,3,4-tetraphenyltriphenylene (**73**) and its pyrimidine-substituted analogue (**74**) as precursors yields a heterojunction consisting of undoped (p-type) and N-doped (n-type) cGNR segments, effectively forming a GNR-based p–n junction (Fig. 31b).[80] Undoped and doped segments exhibit bandgaps of 1.6 eV and 1.5 eV, respectively, with a conduction band offset (CBO) of approximately 0.7 eV, as confirmed by STS. DFT calculations predict a type-II staggered band alignment at the heterojunction. Projected density of states (PDOS) analysis reveals a band offset of about 0.5 eV across the junction, while LDOS mapping shows that this shift occurs within an ultrasharp interface ($\sim$2 nm). This creates a strong built-in electric field of $\sim 2 \times 10^8$ V m^{-1}, two orders of magnitude greater than in conventional p-n junctions (Fig. 31b). The resulting band bending enables highly efficient carrier separation, spatially isolating electrons and holes across the interface under excitation.[80]

5.1.2 Controlled sequential polymerization. During the synthesis of GNR heterojunctions *via* the surface-assisted method, the thermally induced homolytic cleavage of carbon–halogen bonds is a key step in polymerization. By leveraging the significant differences in bond dissociation energies among various carbon–halogen bonds, the copolymerization process can be precisely controlled.[85] Monomers containing specific bonds can be sequentially activated at different temperatures, enabling a stepwise polymer growth. Furthermore, by designing bifunctional linkers containing two distinct types of carbon–halogen bonds, a hierarchical polymerization strategy can be achieved: after the initial polymerization, the product undergoes sequential bond cleavage in a temperature gradient, acting as a monofunctional active-site module for secondary growth. Finally, a highly ordered single-interface block copolymer GNR heterojunction is formed *via* cyclodehydrogenation. Using this strategy, a precisely sequenced, single-interface width-modulated cGNR/binaph-cGNR heterojunction was constructed by Crommie *et al.* in 2018 (Fig. 32a).[85] The bifunctional linker increased the yield of well-defined heterojunctions sevenfold over random copolymerization. STS and DFT analysis revealed a type-I band alignment: cGNR has a bandgap of 2.45 ± 0.05 eV and binaph-cGNR 2.10 ± 0.05 eV, with all band extrema located in the same segment. dI/dV mapping showed that the states of binaph-cGNR (CB_2, VB_2) and cGNR's conduction band (CB_1) are localized to their respective domains, while cGNR's valence band (VB_1) remains delocalized, consistent with DFT simulations (Fig. 32a). The superior structural control capabilities demonstrated by this modified copolymerization strategy provide a crucial methodological foundation for advancing the approach toward practical applications. However, the synthesis of bifunctional linkers containing two distinct carbon–halogen bonds remains undoubtedly challenging. Additionally, to prevent insufficient molecular weight of polymer segments, the amount of capping agent must be significantly lower than that of the main monomer, which makes it difficult to construct multiple composite interfaces.[85]

5.1.3 Post-modification strategy. By incorporating the functional moieties with thermal or electrical responsiveness into polymerizable monomers, homogeneous GNRs can first be synthesized and subsequently modified *via* the reactivity of these active groups to obtain heterostructures.[208,211] Compared to the copolymerization approach for synthesizing GNR heterojunctions, this post-modification strategy eliminates the need to prepare two distinct monomers, thereby simplifying the synthetic procedure. Furthermore, since post-modification processes are generally easier to control than co-polymerization processes, this strategy offers the potential to achieve more precise, controllable construction of GNR heterojunctions. The carbonyl group, with its combined properties of thermal cleavability and significant electron-withdrawing effect, can modulate the electronic properties of GNRs and is therefore an ideal functional group for constructing GNR heterojunctions. Building on this, Crommie *et al.* in 2017 first prepared fluorenone-functionalized chevron-type GNRs with removable edge carbonyl groups on an Au(111) surface *via* stepwise polymerization and cyclodehydrogenation (Fig. 32b).[208] Subsequently, vacuum annealing at 350 °C triggered decarbonylation, successfully constructing an edge-structure modulated heterojunction consisting of unmodified cGNR segments and fluorenone-GNR segments. Experimental results showed that the fluorenone-functionalized GNR has a bandgap of 2.33 eV, which is 0.20 eV lower than that of the unmodified chevron GNR (2.53 eV), with both VBM and CBM shifting toward lower energy. Meanwhile, spatially resolved STS imaging revealed that conduction-band states are primarily localized in the fluorenone-modified segments, whereas valence-band states are concentrated in the unmodified segments, indicating the characteristic spatial separation of electronic states typical of a type-II heterojunction. Furthermore, both theory and experiment indicate that the band-alignment transition occurs within an interfacial region of less than 1 nm, generating a strong localized electric field of approximately 5×10^8 V m^{-1} (Fig. 32b).[208]

In addition to simple thermal cleavage, certain units can undergo structural reconstruction at high temperatures. For example, methylcarbazole undergoes two competitive thermal reactions: demethylation to carbazole or rearrangement to phenanthridine. Notably, when located at GNR edges, carbazole acts as an electron donor, whereas phenanthridine acts as an electron acceptor, thereby enabling GNR heterojunctions with unique electronic properties. Based on this, a methylcarbazole-functionalized polymer precursor (P55) was synthesized (Fig. 32c).[211] During its on-surface polymerization and cyclodehydrogenation on Au(111),

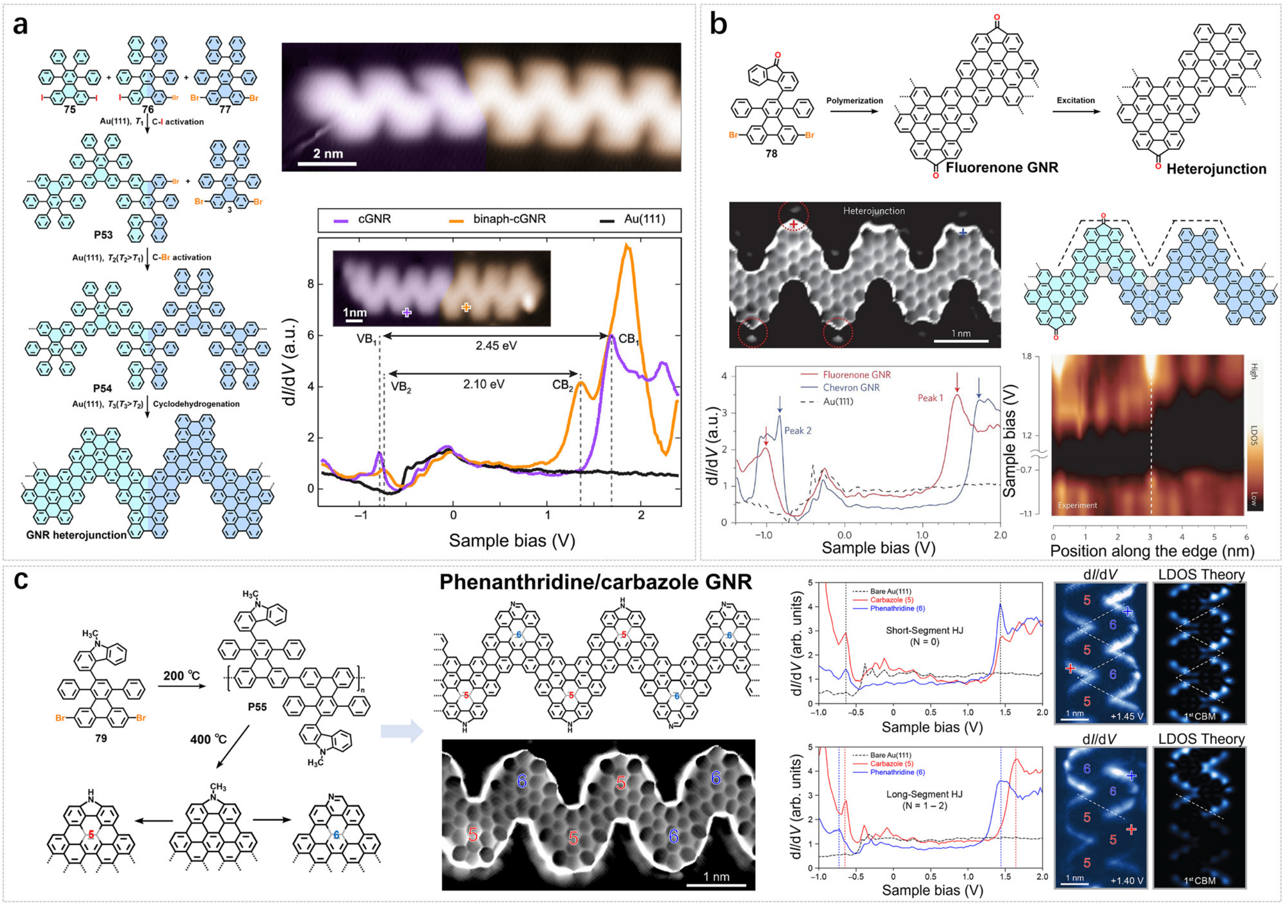

Fig. 32 (a) Schematic representation of the hierarchical on-surface synthesis of cGNR/binaph-cGNR heterojunctions as well as their STM image and spatially inhomogeneous bandgap. Reprinted with permission from ref. 85. Copyright 2018, American Chemical Society. (b) Fabrication of fluorenone/unfunctionalized chevron GNR heterojunctions as well as their BRSTM image, electronic structure and the band alignment across the heterojunction interface. Reprinted with permission from ref. 208. Copyright 2017, Springer Nature. (c) Bottom-up fabrication of carbazole/phenanthridine edge-functionalized GNR heterostructures with corresponding BRSTM imaging, revealing length-dependent band offset and wave function localization at heterojunction interfaces *via* combined STM and simulation. Reprinted with permission from ref. 211. Copyright 2019, American Chemical Society.

simultaneous edge reconstruction resulted in GNRs containing nitrogen in two distinct configurations. The electronic band structure of these GNR heterojunctions exhibits a distinct length dependence (Fig. 32c). In the shortest heterojunction with alternating blocks (N = 0), the VBE and CBE on both sides of the interface were nearly aligned, resulting in a negligible band offset. As the heterojunction length increased (N = 1 to N = 2), a distinct staggered type-II band alignment emerged across the interface. Specifically, in the 5-block regions (N = 2) compared to the 6-block region (N = 1), a VBE offset of 0.07 eV and a CBE offset of 0.21 eV were observed (Fig. 32c).[211] Corresponding dI/dV mapping further revealed the spatial distribution characteristics of the wave functions: in short heterojunctions, charge carrier wave functions were uniformly distributed across both sides of the interface, whereas in longer heterojunctions, the CBE state became notably localized on the phenanthridine (6-block) side with higher electron affinity. Combined with theoretical analysis, this length-dependent band offset primarily originates from charge-transfer-driven electrostatic potential renormalization at the interface—strong charge transfer in short heterojunctions nearly cancels out the intrinsic electron affinity difference between the monomers, while as the length increases, the charge transfer effect weakens, allowing the intrinsic energy level differences between monomers to become prominent. This systematically modulates the band alignment behavior of the heterojunction.[211]

5.1.4 Edge fusion and partial dehydrogenation. By controlling the reaction process during GNR synthesis, such as regulating the molecular alignment of GNRs or applying additional annealing procedures, heterojunctions can be constructed by leveraging the intrinsic edge reactivity of GNRs, such as through the lateral fusion of AGNRs.[22,84,212,213] Under thermal annealing, adjacent AGNR segments fuse *via* edge-crossing dehydrogenative coupling. This width-dependent fusion is exemplified by 7-AGNR (N = 3p + 1 family) forming 14-AGNR (N = 3p + 2 family), a narrow-bandgap, quasi-metallic quantum dot embedded in the wider-gap 7-AGNR matrix, creating a unique heterostructure (Fig. 33a).[213] STS confirms that the heterojunction composed of 14-AGNR and 7-AGNR forms a type I band alignment, with the entire band structure of 14-AGNR lying within the bandgap of 7-AGNR. Six low-energy

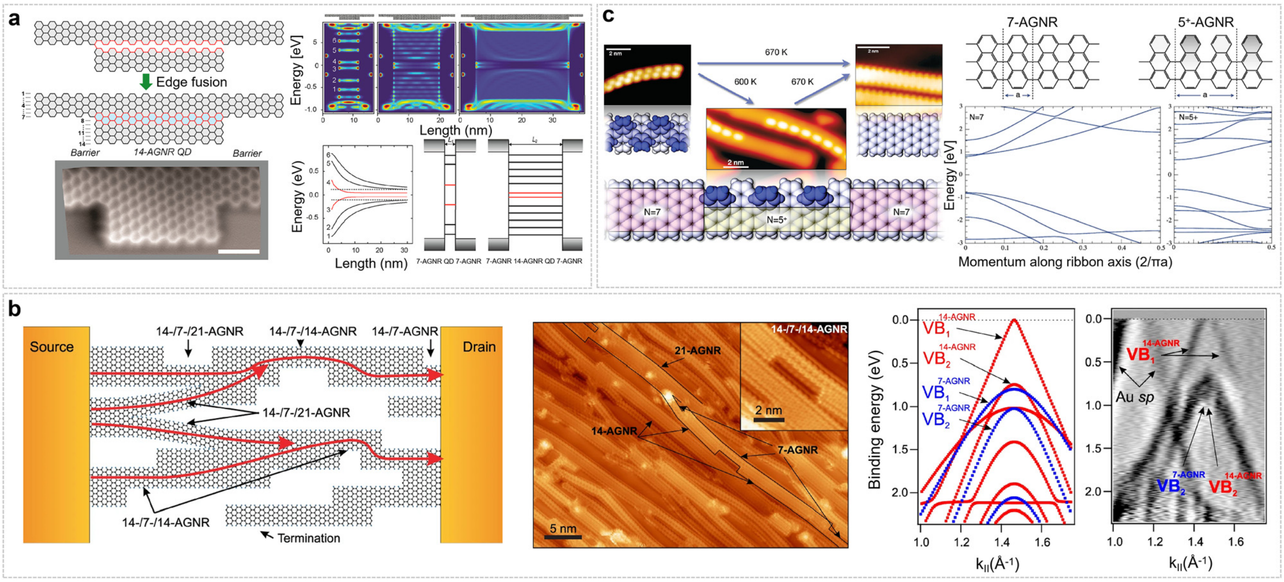

Fig. 33 (a) Schematic and STM image showing 7-14-7 AGNR heterostructures formed *via* edge fusion and their length-dependent energy level scheme. Reprinted with permission from ref. 213. Copyright 2017, American Chemical Society. (b) Schematic and STM image of 7–14 aligned GNR heterojunctions *via* edge fusion, and comparison between the calculated electronic band structures of each segment, as well as the momentum-derivative angle-resolved photoemission spectroscopy (ARPES) scan of fused GNRs and their charge transport characterization of with different length. Reprinted with permission from ref. 22. Copyright 2021, Springer Nature. (c) Realization of GNR heterojunctions by partial cyclodehydrogenation of polyanthrylene oligomers and band structure calculations for each segment. Reprinted with permission from ref. 84. Copyright 2012, American Chemical Society.

states are localized in the quantum dot: the central HOMO and LUMO (interface states with a 5 nm decay length) and four bulk states. Tight-binding modeling shows that interface-state splitting is highly length-dependent, dropping exponentially from 400 meV to 80 meV as length increases from 2 to 10 nm, enabling nanoscale electrical tuning (Fig. 33a). The bulk states converge more slowly, following a typical inverse-length dependence.

Using stepped Au(788) substrates enables the growth of aligned 7-AGNR arrays. Upon thermal annealing, adjacent GNRs undergo cascaded edge fusion, progressively forming segments of 14-, 21-, and 28-AGNRs, thus creating arrays of width-modulated heterojunctions (Fig. 33b).[22] In these arrays, quasi-metallic wide segments are connected by wide-bandgap 7-AGNR sections. STM and transport measurements confirm a type-I band alignment at the 7-/14-AGNR interface, with a ∼1.35 eV barrier. For electrical transport characterization, aligned GNR heterojunction films were transferred onto SiO_2/Si substrates by electrochemical delamination to fabricate back-gated field-effect transistors (FETs). These devices show nonlinear I–V curves, ambipolar gating, low mobility, and weak temperature dependence, consistent with multi-barrier tunneling at the heterojunction interfaces. Current decays exponentially with channel length, supporting a WKB-type tunneling model (Fig. 33b).[22]

In the synthesis of GNR heterojunctions, in addition to the previously mentioned "additive" modification strategies achieved through additional chemical reactions, reverse modulation of the reaction process is also noteworthy. Specifically, by precisely controlling key steps in bottom-up synthesis, such as selectively inhibiting or partially carrying out cyclodehydrogenation, GNRs with heterogeneous structures can be directly constructed. Pignedoli *et al.* discovered that the cyclodehydrogenation efficiency of linear polymer precursors for GNRs is highly dependent on both annealing temperature and duration.[84] By precisely controlling these two key parameters, it is possible to achieve the ordered coexistence of fully dehydrogenated and partially dehydrogenated structural units within the GNR, thereby directly constructing GNR heterojunctions without additional functionalization or modification steps (Fig. 33c).[84] Based on this concept, they used polyanthrylene oligomers as precursors on an Au(111) surface. Through self-assembly and thermally induced cyclodehydrogenation, they successfully fabricated ultra-narrow GNR heterojunctions with widths below 2 nm. By carefully tuning the annealing temperature, partial dehydrogenation was achieved, resulting in the formation of intra-ribbon heterojunctions composed of alternating fully dehydrogenated 7-AGNR segments and partially dehydrogenated 5^+-AGNR segments (Fig. 33c). DFT calculations revealed that the dehydrogenation process follows a "unilateral domino" mechanism, in which the reaction proceeds progressively along one side of the polymer chain rather than the conventional "zipper-like" bilateral alternation. This mechanism leads to the formation of partially dehydrogenated products along one side, avoiding the complexity of mixed segments with fully dehydrogenated, partially dehydrogenated, and non-dehydrogenated regions. Further theoretical calculations reveal a 0.3 eV bandgap difference between 7-AGNR and 5^+-AGNR, with the latter's entire band structure nested within the 7-AGNR bandgap, forming a characteristic type-I heterojunction (Fig. 33c).[84]

5.1.5 Stepwise synthesis strategy. Most heterojunction synthesis methods described earlier typically yield randomly arranged GNR copolymers due to limited control over the polymerization process. Therefore, constructing structurally ordered block-copolymer-type GNR heterojunctions represents a critical step. The core of building such ordered structures lies in achieving highly controllable polymerization processes, in which iterative stepwise polymerization strategies provide nearly optimal synthetic precision and control.[129,131,133,134,208,214–218] In iterative synthesis, precise molecular design strictly confines each coupling reaction to predetermined active sites, enabling absolute and accurate control over the polymer sequence. Among various iterative strategies, the protecting-group-assisted iterative synthesis approach, due to its high yield and selectivity during terminal activation and reconstruction, has emerged as a route to synthesizing GNR heterojunctions.[130,219] Suzuki–Miyaura coupling (SMC) is a commonly used coupling reaction in GNR precursor synthesis, typically involving halogen substituents and boronic acid/ester groups on aromatic rings. The protecting-group-assisted iterative method based on SMC has been employed to construct monodisperse 9-AGNR/chevron GNR heterostructures (Fig. 34a).[130] This synthesis uses bifunctional monomers (**80**, **81**) bearing both a bromo group and a boronic acid group, protected by 1,8-diaminonaphthalene. Each synthesis cycle consists of two defined steps: first, SMC precisely links a monomer unit to the exposed boronic acid group at the growing chain terminus; subsequently, acidolysis removes the boronic acid protecting group on the newly incorporated monomer, regenerating the active boronic acid group for the next coupling cycle. The precisely synthesized GNR heterojunction precursor polymer is then transferred onto an Au(111) surface *via* matrix-assisted direct transfer (MAD) techniques, followed by cyclodehydrogenation to form the target GNR heterojunction (Fig. 34a). Notably, by introducing monomers with two functional groups arranged at a specific angle, kink points can be incorporated into the structure, enabling the synthesis of kinked GNR heterojunctions with defined turn angles.[130]

The aforementioned methods enable precise synthesis of GNR heterojunctions, yet they suffer from low efficiency, cumbersome procedures, and solubility limitations that hinder the preparation of long-chain structures. To overcome these constraints, researchers have integrated protecting-group-assisted iterative synthesis with iterative binomial synthesis, developing a combined iterative binomial synthesis strategy. Implementing this strategy requires that both terminal functional groups of the monomer be activatable. To meet this requirement, in 2023, Dong's team replaced the conventional aryl bromide with a phenol hydroxyl group as the activatable terminus—triflate-activated to generate the OTf group—and combined it with a B(dan)-protected boronate building block. Through iterative parallel deprotection/triflate activation and Suzuki–Miyaura coupling steps, exponential growth in polymer chain length and

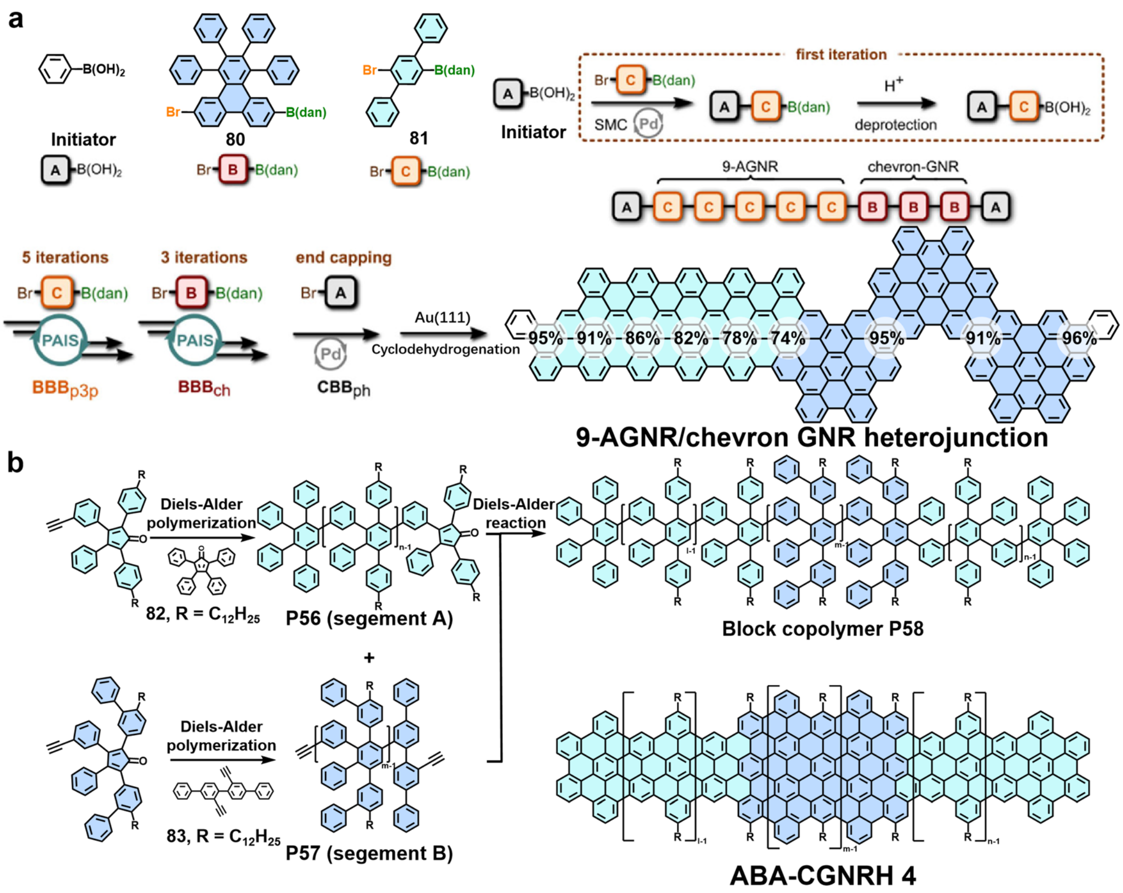

Fig. 34 (a) Synthesis of 9-chGNRs *via* PAIS strategy. Reprinted with permission from ref. 130. Copyright 2022, American Chemical Society. (b) The synthesis of ABA-CGNRHs.

precise sequence control are achieved.[220] This hybrid strategy provides dual control: iterative binomial synthesis doubles the chain length in each cycle (requiring only five iterations to yield a 64-unit polymer), while protecting-group-assisted iterative synthesis allows tailored heterostructure design through customized monomer introduction. It should be noted that this work produced only well-defined polyphenylene precursors, which still require subsequent on-surface cyclodehydrogenation to yield the final GNR heterojunctions.[220]

In 2023, Müllen *et al.* reported a bottom-up synthetic strategy based on the Diels-Alder reaction for the controlled construction of solution-processable, gulf-edged GNR heterojunctions (CGNRHs). This work employed two distinct aromatic precursors with well-defined and different widths as monomers (**82**, **83**)—specifically designed for synthesizing narrow 4CGNRs and wide 6CGNRs.[206] Through segmented synthesis, interfacial assembly, and cyclodehydrogenation, a clearly defined double-interface heterojunction with an explicit ABA sequence (corresponding to the alternating A- and B-segments illustrated in Fig. 34b) was successfully constructed. The key to the synthesis lies in the controlled cycloaddition of two structurally complementary capping molecules, coupled with precise temperature-gradient control over the reaction sequence, thereby enabling stepwise growth of a heterojunction with atomically precise edge structure. The resulting CGNRHs combine atomic-level structural precision with unique optoelectronic properties. Scanning probe microscopy and Raman spectroscopy confirmed their high structural uniformity, and self-assembled thin-film devices on diamond exhibited photoresponse peaks that matched the absorption spectra. Real-time DFT simulations further revealed a type-I band alignment and wavelength-dependent reversal of charge-transfer direction.[206]

5.1.6 Chain growth polymerization strategy. The aforementioned modular stepwise synthesis strategy enables the preparation of structurally well-defined GNR heterojunctions with controllable lengths. However, its stepwise assembly process is highly cumbersome, significantly increasing the time and effort required for heterojunction synthesis. In linear polymerization, living polymerization methods can achieve precise control over the polymer chain ends,[135–137,221–228] similar to that in stepwise synthesis strategies, thereby allowing the construction of GNR heterojunctions with well-defined structures *via* a comparable rationale. This approach eliminates the need for isolation and purification of intermediate products, substantially reducing the synthetic workload. Its core lies in the precise regulation of chain-growth active centers, thereby preventing spontaneous termination and chain-transfer reactions and enabling highly controlled polymerization. If the reaction is not actively terminated, the system can maintain a single active chain end, yielding well-defined building blocks for heterostructures.

In 2023, our group reported a chain-growth polymerization strategy utilizing Suzuki–Miyaura catalyst-transfer polymerization (SCTP), which enables the efficient and controlled construction of structurally well-defined heterojunctions composed of 9-AGNRs and chevron GNRs (9-AGNR/cGNR) from two distinct monomers (Fig. 35).[135] The key to this synthetic route lies in the design and synthesis of monomers **84** and **85**, both of which bear long alkyl side chains. Specifically, **84** is a mono-bromo-substituted terphenyl-type compound, and **85** is a mono-bromo-substituted triphenylene-based boronic ester decorated with four additional phenyl rings. These structures are precisely designed not only to participate in the SCTP reaction for controlled polymerization but also to impart good solubility to the intermediate products *via* their side chains, thereby facilitating subsequent solution processing. During the polymerization process, under an optimized palladium catalytic condition, **84** and **85** were sequentially added *via* a living polymerization approach. This "one-pot" sequential reaction yielded a block copolymer precursor (**P59**) with controlled structure and a

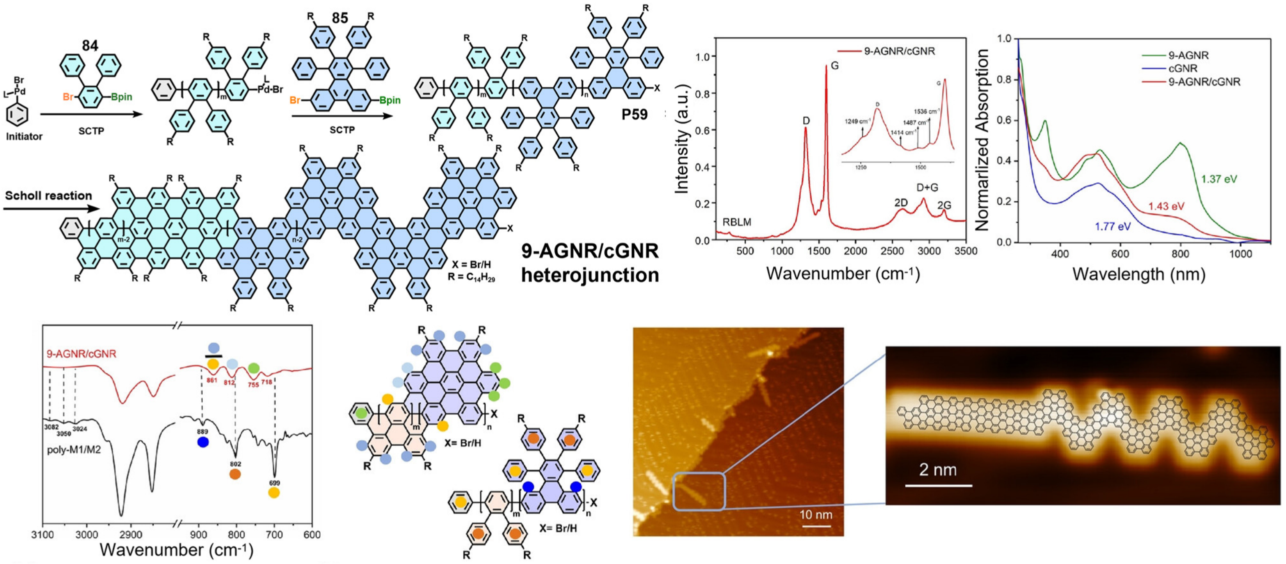

Fig. 35 Controlled synthesis of 9-AGNR/cGNR heterojunctions *via* chain-growth polymerization, characterized by FT-IR and Raman spectroscopy, UV/Vis absorption, and topographic STM imaging on Au(111). Reprinted with permission from ref. 135. Copyright 2023, Wiley-VCH.

narrow molecular weight distribution (Fig. 35).[135] This polymerization process avoids the tedious isolation and purification steps required in traditional stepwise synthesis, significantly enhancing both synthetic efficiency and controllability. Subsequently, through an $FeCl_3$-mediated Scholl reaction, the block copolymer precursor undergoes efficient intramolecular cyclodehydrogenation in solution, ultimately transforming into a fully conjugated heterojunction structure. The resulting heterojunction consists of two GNR segments with distinct topologies (9-AGNRs and chevron GNR) covalently linked to form a hybrid system with atomically precise interfaces and the structure was directly verified using STM (Fig. 35). It exhibits characteristic spectroscopic signals from both parent GNRs, with its optical absorption significantly red-shifted into the near-infrared region and an optical bandgap intermediate between those of the two GNRs (Fig. 35).[135] Notably, the chain-growth polymerization strategy exhibits a high degree of generality, making it broadly applicable, and holds significant promise for the construction of various other GNR-based heterojunctions.

5.2 Topological state in GNR heterostructure

At the heterojunction interface, in addition to the realignment of energy bands at the nanoscale between the two GNR segments, a reorganization of topological invariants may also occur.[81,82,229] While band alignment can endow the heterojunction with unique electronic properties, changes in topological invariants may introduce novel topological features. By coupling GNR units with different topological invariants, modulation and coupling of topological states can be achieved at the interface, thereby enabling the construction of topological GNR heterojunctions with designable electronic properties. In 2018, Fischer *et al.* fabricated a GNR superlattice composed of alternating topologically distinct 7-AGNR ($\mathbb{Z}_2 = 0$) and 9-AGNR ($\mathbb{Z}_2 = 1$) segments (Fig. 36a).[82] Combined low-temperature STM measurements and first-principles calculations revealed that its unique band structure is primarily dominated by topologically protected interface states. Experimental results indicated the presence of four characteristic electronic states (peaks A–D) in the superlattice bulk region. Peaks B and C, located near the Fermi level, form a bandgap of approximately 0.74 eV, which is significantly narrower than that of homogeneous 7-AGNR (~2.3 eV) and 9-AGNR (~1.4 eV), demonstrating that the coupling of topological interface states effectively modulates the frontier band structure of the GNR. Furthermore, they observed three topological end states (end states 1–3) localized at the terminal unit cell of the superlattice, residing

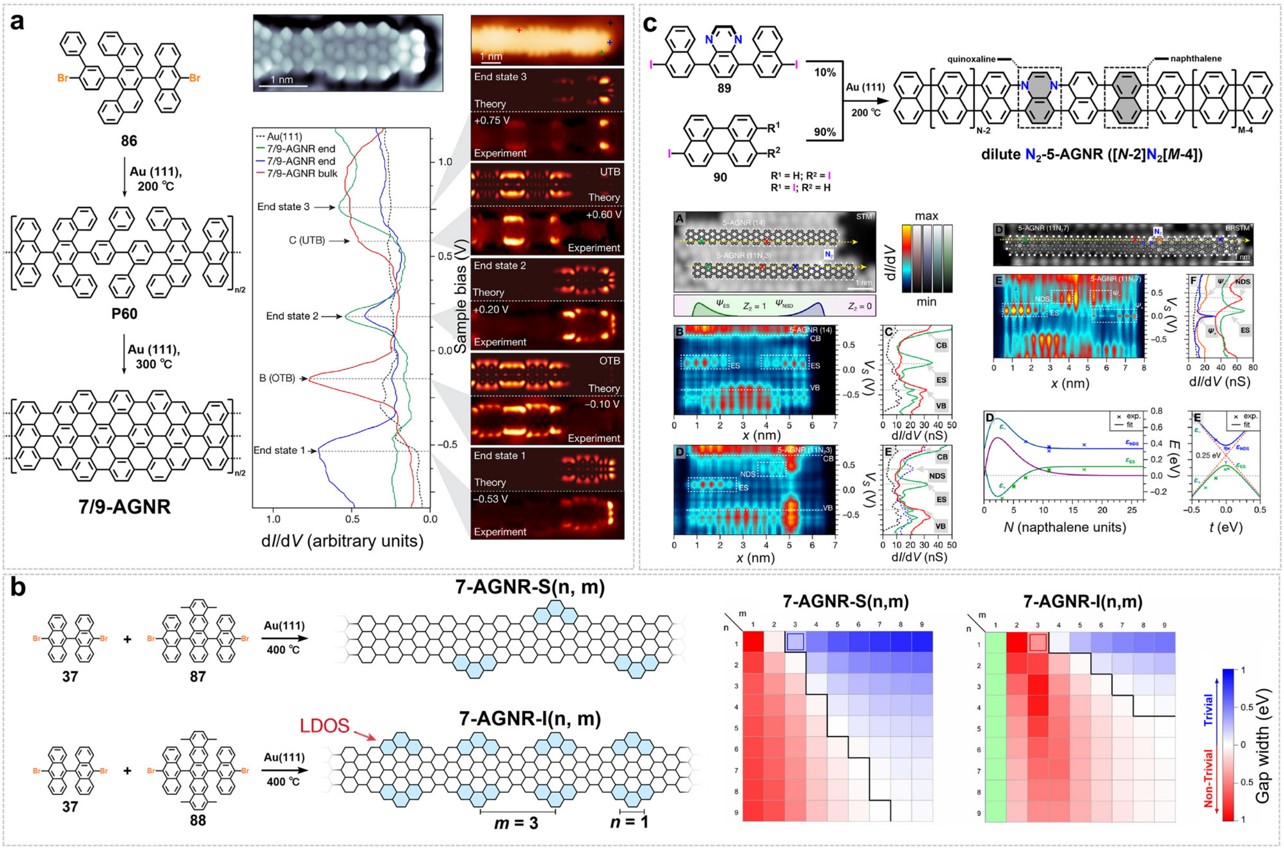

Fig. 36 (a) Bottom-up synthesis of 7/9-AGNR superlattice, and electronic structure of its superlattice end states. Reprinted with permission from ref. 82. Copyright 2018, Springer Nature. (b) Synthesis of 7-AGNR-*S*(*n*,*m*) and 7-AGNR-*I*(*n*,*m*) and the topological phase diagram (according to $\mathbb{Z}_2$) of the 7-each structure family. Reprinted with permission from ref. 81. Copyright 2018, Springer Nature. (c) Synthesis of dilute N-doped N_2-5-AGNRs, with experimental and simulated STS data for 5-AGNR(14), 5-AGNR(11$N_2$3), and 5-AGNR(11$N_2$7). Includes topographic imaging, line scans, point spectra, and the distance-dependent interaction, along with empirical model fitting and calculated results. Reprinted with permission from ref. 229. Copyright 2025, American Chemical Society.

within the energy gaps of the bulk bands A/B, B/C, and C/D, respectively.[82] Among them, end state 2 is located nearly at the center of the bulk B–C gap (Fig. 36a). Theoretical analysis indicated that the existence of these end states stems from the topologically nontrivial nature ($\mathbb{Z}_2 = 1$) of the overall superlattice across all three energy gaps, consistent with the topological bulk-boundary correspondence. Fitting with a tight-binding model yielded the hopping amplitudes for the topological interface states. The coupling from the 9-AGNR to the 7-AGNR segment was $t_1 = 0.33$ eV, and the reverse coupling was $t_2 = -0.07$ eV. The opposite signs of these amplitudes give rise to a direct bandgap at the Γ point, elucidating the mechanism of topological band formation.[82]

Also in 2018, to elucidate the tunability of topological interface states and the impact of coupling between topological boundary states on the electronic band structure, Fasel and us designed two types of edge-extended heterojunction structures based on 7-AGNRs (Fig. 36b): the staggered 7-AGNR-*S* and the in-line 7-AGNR-*I*.[81] Combined scanning tunneling microscopy measurements and tight-binding theoretical calculations reveal electronic structures that resemble those of the SSH model, dominated by coupling between topological boundary states. Experimental results confirm that by varying the structural parameters, *i.e.*, the extended segment length n and the spacing between extended segments m, the intracell coupling strength t_n (the coupling between two boundary states within the same extended segment) and the intercell coupling strength t_m (the coupling between boundary states located on different extended segments, mediated by the main backbone segment) can be continuously adjusted.[81] This enables effective control over the transition between topologically trivial ($\mathbb{Z}_2 = 0$) and nontrivial ($\mathbb{Z}_2 = 1$) phases, which is directly reflected in the presence or absence of localized zero-energy end states. When $t_n < t_m$, the system is in a topologically nontrivial phase ($\mathbb{Z}_2 = 1$) and exhibits topologically protected zero-energy end states; when $t_n > t_m$, the system is in a trivial phase ($\mathbb{Z}_2 = 0$) without zero-energy end states; and when $t_n \approx t_m$, the system reaches a metallic critical point where the bandgap closes (Fig. 36b). This demonstrates that without altering the main ribbon width N, continuous and precise control over the electronic bandgap, bandwidth, and topological end-state energy can be achieved solely by adjusting parameters *n* and *m*, thereby offering substantial design freedom for the realization of customizable topological quantum devices. Further research shows that even without altering geometric dimensions (*n* and *m*), changing only the spatial arrangement of the extended segments can induce a quantum phase transition from a topologically trivial to a nontrivial state. High-resolution STS reveals that no localized zero-energy state is observed at the ends of 7-AGNR-*S*(1,3), whereas a clear localized topological end state is detected at the ends of 7-AGNR-*I*(1,3). This demonstrates that the geometric arrangement is also a crucial independent variable governing topological properties.[81]

Furthermore, introducing heteroatoms into the GNR backbone can alter the topological invariants of the corresponding segments, thereby inducing topological interface states within the heterojunction.[229] By controlling the distance between doping sites, the spatial distribution of different topological interface states can also be modulated. To investigate the evolution of the topological reconstruction process with reconstruction length, in 2025, Fischer *et al.* synthesized sparsely nitrogen-doped GNRs (N_2-5-AGNRs) *via* copolymerization of nitrogen-containing monomers (**89**) with undoped perylene-based precursors (**90**) (Fig. 36c).[229] By varying the feed ratio of the nitrogen-containing monomer, products with different spacings between doping sites were obtained (Fig. 36c). STM characterization identified two localized states: a topological end state at ∼110 meV and a nitrogen-induced boundary state at ∼440 meV, separated by $\Delta\varepsilon \approx 330$ meV. Studies of heterojunctions have shown that these topological states interact significantly. As the distance between them increases, their mutual coupling decays, but the energy offset remains finite. This coupling hybridizes the two nondegenerate modes, resulting in bonding (lower energy) and antibonding (higher energy) states, which appear as new peaks in the d*I*/d*V* spectra (Fig. 36c).[229]

6. Conclusion and perspective

Since the pioneering work on the synthesis of atomically precise GNRs in 2010, this research field has undergone rapid development over the past decade. In addition to the previously defined armchair and zigzag edge structures, a series of novel edge configurations have been successfully synthesized, including cove, fjord, chiral, and asymmetric edges. Building upon this, the community has further expanded the structural diversity to include heteroatom-doped GNRs, non-hexagonal-ring-embedded structures, porous GNRs, and helical GNRs. In recent years, significant attention has focused on GNR heterojunctions with precisely defined interfaces. This has spurred the development of various synthetic strategies—based on controlled polymerization or modular connection—and enabled detailed characterization of their electronic band structures, localized states, and topological properties. The deep integration of synthetic chemistry, high-resolution characterization, and theoretical calculations has established a systematic methodological foundation for elucidating the structure–property relationships in GNRs. These developments have thereby laid a solid scientific groundwork for their potential applications in the frontier fields such as nanoelectronics, spintronics, and quantum devices. However, despite significant advancements in structural design and property modulation, several key scientific challenges and technical obstacles in the field of GNRs still require systematic breakthroughs:

(1) Controllable synthesis and precise characterization of GNRs with unique edge topology or chiral structures. In terms of synthesis, the main challenges lie in the precise construction of cove-edges, fjord-edges, or even helical and chiral structures. Such structures can only be achieved through the rational design of precursors and by addressing a series of chemical kinetic control issues during the reaction process. These issues include the precise regulation of regioselectivity in cyclization reactions and the preservation of helical or chiral conformations under

thermodynamically metastable conditions. To accelerate progress, machine learning and artificial intelligence should be applied for high-throughput screening of novel monomers with target topological band structures, as well as for predicting reaction pathways and regioselectivity prior to experimental synthesis. In terms of characterization, the detailed analysis of such atypical structures also presents challenges. Conventional spectroscopic techniques have limited sensitivity when it comes to probing localized chemical environments at edges, chiral electronic states, and helical structures. While scanning probe microscopy can provide morphological information at the atomic scale, it still has limitations in reconstructing three-dimensional conformation and in tracking dynamic structural evolution. Future progress will depend on the deep integration of synthetic chemistry, characterization techniques, and theoretical calculations, ultimately enabling the precise customization and functionalized regulation of such GNR structures.

(2) Precision synthesis of non-benzenoid GNRs and porous GNRs. The key challenge arises from the lattice strain introduced by non-hexagonal rings and porous structures, which renders the entire π-conjugated framework thermodynamically metastable. This intrinsic instability can lead to uncontrollable skeletal rearrangements, ring contraction, or ring expansion during the cyclodehydrogenation process, thereby compromising the predefined topological structure and pore integrity. Although on-surface chemistry has enabled the construction of such structures, the harsh reaction conditions and extremely low yields limit their scalability, severely hindering large-scale production and subsequent applications in thermoelectronics, ion transport, and related fields. Consequently, several strategies are required: incorporating kinetically stable units (*e.g.*, sterically shielded aromatic cores) into precursors to suppress side reactions; developing novel cyclization reactions (*e.g.*, photochemical cyclodehydrogenation) that are both highly selective and mild; and exploring scalable liquid-phase synthesis routes. Together, these advances will enable the precise synthesis and efficient, scalable production of such GNR structures.

(3) New pathways toward precisely controlled GNR heterostructures. To prepare GNR heterostructures with complex architectures, it is essential to start from molecular design by developing modular and programmable precursor monomers, enabling precise control over heterojunction types, atomic-level interface structures, and topological edge states. Key strategies include developing living polymerization methods with sequence programming (*e.g.*, Suzuki–Miyaura catalyst-transfer polymerization, SCTP) to synthesize block copolymers with uniform lengths and controlled monomer sequences, as well as employing protecting-group-assisted iterative synthesis (PAIS) to construct sequence-defined monodisperse GNR precursors; both approaches, together with exploring a synergistic strategy that combines solution-phase polymerization with surface-assisted cyclodehydrogenation, represent promising routes for precise heterostructure fabrication. Through these routes, precise and controllable synthesis of GNR heterostructures can be realized, offering an ideal materials platform for in-depth investigation of quantum transport and other physical phenomenon in GNRs.

(4) Singly dispersed GNRs for functional device applications. This direction is currently hindered by several key challenges: the stable single-dispersion of GNRs in solution, and their controllable assembly and characterization at the single-molecule level. In liquid-phase dispersion, covalent edge functionalization strategies employing bulky substituents are primarily used to improve solubility; however, these methods face challenges, including complex synthesis procedures and difficulty precisely controlling the functionalized substituents, which significantly affect subsequent device integration. To overcome this, introducing either thermally cleavable or photo-cleavable temporary solubilizing side chains, or developing GNRs with intrinsically twisted backbone structures, provides effective strategies to minimize insulating barriers and improve charge injection. In the construction of single-molecule devices, techniques based on nanogap electrodes have enabled measurements of the electrical and quantum properties of individual GNRs, revealing their low-dimensional confinement characteristics. However, interfacial contact resistance, unclear structure-performance correlations, and difficulties in integration remain key bottlenecks hindering their practical application. Future efforts require the development of synergistic strategies that integrate functionalization, transfer, and characterization, and the establishment of a systematic research system spanning molecular structure modulation to device performance optimization to advance the development of GNRs in nanoelectronics and spintronics.

Author contributions

X. F., X. W., J. M., and X. L. conceived and supervised the project, and revised the entire manuscript. X. C., Y. Q. and X. W. wrote the full manuscript and prepared figures. J. Z. revised the manuscript, particularly the part on GNR heterojunctions. The manuscript was written with contributions from all authors. All authors have given approval to the final version of the manuscript.

Conflicts of interest

The authors declare no competing interests.

Data availability

No primary research results, software or code have been included and no new data were generated or analyzed as part of this review. The supplementary information file provides a detailed introduction to ultrafast optical-pump terahertz-probe spectroscopy, along with relevant references, a comprehensive list of abbreviations and their chemical structures. See DOI: https://doi.org/10.1039/d6cs00220j.

Acknowledgements

This work was financially supported by the National Natural Science Foundation of China (Grant No. 52422315, 52273012), the Sichuan Science and Technology Program (2024YFHZ0311), National Key Research and Development Program of China (No. 2024YFB3713200), EIC-2022-Pathfinder Open (ATYPIQUAL, 101099098), Max-PlanckGesellschaft/MPG internal project-Lighthouse (M.TT.A.MIKR00F1), Deutsche Forschungsgemeinschaft (DFG, German Research Foundation)–GRK2861–491865171, and the Center for Advancing Electronics Dresden (cfaed). J. M. thanks the National Natural Science Foundation of China for funding (Grant No. 92463307, 22575243). Open Access funding provided by the Max Planck Society.

Notes and references

1 A. K. Geim and K. S. Novoselov, *Nat. Mater.*, 2007, **6**, 183–191.
2 A. K. Geim, *Science*, 2009, **324**, 1530–1534.
3 A. H. Castro Neto, F. Guinea, N. M. R. Peres, K. S. Novoselov and A. K. Geim, *Rev. Mod. Phys.*, 2009, **81**, 109–162.
4 F. Bonaccorso, Z. Sun, T. Hasan and A. C. Ferrari, *Nat. Photonics*, 2010, **4**, 611–622.
5 M. Yi and Z. Shen, *J. Mater. Chem. A*, 2015, **3**, 11700–11715.
6 F. Perreault, A. Fonseca De Faria and M. Elimelech, *Chem. Soc. Rev.*, 2015, **44**, 5861–5896.
7 X. Yu, H. Cheng, M. Zhang, Y. Zhao, L. Qu and G. Shi, *Nat. Rev. Mater.*, 2017, **2**, 17046.
8 D. G. Papageorgiou, I. A. Kinloch and R. J. Young, *Prog. Mater. Sci.*, 2017, **90**, 75–127.
9 F. Schwierz, *Nat. Nanotechnol.*, 2010, **5**, 487–496.
10 H. Wang, H. S. Wang, C. Ma, L. Chen, C. Jiang, C. Chen, X. Xie, A.-P. Li and X. Wang, *Nat. Rev. Phys.*, 2021, **3**, 791–802.
11 R. S. K. Houtsma, J. De La Rie and M. Stöhr, *Chem. Soc. Rev.*, 2021, **50**, 6541–6568.
12 W. Xu and T.-W. Lee, *Mater. Horiz.*, 2016, **3**, 186–207.
13 J. Cai, P. Ruffieux, R. Jaafar, M. Bieri, T. Braun, S. Blankenburg, M. Muoth, A. P. Seitsonen, M. Saleh, X. Feng, K. Müllen and R. Fasel, *Nature*, 2010, **466**, 470–473.
14 O. V. Yazyev, *Acc. Chem. Res.*, 2013, **46**, 2319–2328.
15 K. Wakabayashi, K. Sasaki, T. Nakanishi and T. Enoki, *Sci. Technol. Adv. Mater.*, 2010, **11**, 054504.
16 K.-Y. Yoon and G. Dong, *Mater. Chem. Front.*, 2020, **4**, 29–45.
17 R. Yin, Z. Wang, S. Tan, C. Ma and B. Wang, *ACS Nano*, 2023, **17**, 17610–17623.
18 J. Zhang, J. Ma and X. Feng, *Macromol. Chem. Phys.*, 2023, **224**, 2200232.
19 H. Luo and G. Yu, *Chem. Mater.*, 2022, **34**, 3588–3615.
20 J. Zhang, B. Ghawri, D. Dutta, R. Fasel, M. Calame, G. Borin Barin and M. L. Perrin, *Nat. Rev. Mater.*, 2026, 0–19.
21 H. Deng, Z. Qu, Y. He, C. Huang, N. C. Panoiu and F. Ye, *Quantum Front.*, 2023, **2**, 11–20.
22 B. V. Senkovskiy, A. V. Nenashev, S. K. Alavi, Y. Falke, M. Hell, P. Bampoulis, D. V. Rybkovskiy, D. Yu. Usachov, A. V. Fedorov, A. I. Chernov, F. Gebhard, K. Meerholz, D. Hertel, M. Arita, T. Okuda, K. Miyamoto, K. Shimada, F. R. Fischer, T. Michely, S. D. Baranovskii, K. Lindfors, T. Szkopek and A. Grüneis, *Nat. Commun.*, 2021, **12**, 2542.
23 H. Zhu, G. Wen, W. Zheng, N. H. Rees, W. Stawski, H. I. Wang, M. Bonn and H. L. Anderson, *Angew. Chem., Int. Ed.*, 2025, **64**, e202417429.
24 Z. Chen, J.-R. Deng, M. Wang, N. Farmakidis, J. Baugh, H. Bhaskaran, J. A. Mol, H. L. Anderson, L. Bogani and J. O. Thomas, *J. Am. Chem. Soc.*, 2025, **147**, 22572–22579.
25 W. Niu, S. Sopp, A. Lodi, A. Gee, F. Kong, T. Pei, P. Gehring, J. Nägele, C. S. Lau, J. Ma, J. Liu, A. Narita, J. Mol, M. Burghard, K. Müllen, Y. Mai, X. Feng and L. Bogani, *Nat. Mater.*, 2023, **22**, 180–185.
26 J. Zhang, L. Qian, G. B. Barin, A. H. S. Daaoub, P. Chen, K. Müllen, S. Sangtarash, P. Ruffieux, R. Fasel, H. Sadeghi, J. Zhang, M. Calame and M. L. Perrin, *Nat. Electron.*, 2023, **6**, 572–581.
27 M. Slota, A. Keerthi, W. K. Myers, E. Tretyakov, M. Baumgarten, A. Ardavan, H. Sadeghi, C. J. Lambert, A. Narita, K. Müllen and L. Bogani, *Nature*, 2018, **557**, 691–695.
28 J. Zhang, G. B. Barin, R. Furrer, C.-Z. Du, X.-Y. Wang, K. Müllen, P. Ruffieux, R. Fasel, M. Calame and M. L. Perrin, *Nano Lett.*, 2023, **23**, 8474–8480.
29 X. Li, X. Wang, L. Zhang, S. Lee and H. Dai, *Science*, 2008, **319**, 1229–1232.
30 D. Wei, L. Xie, K. K. Lee, Z. Hu, S. Tan, W. Chen, C. H. Sow, K. Chen, Y. Liu and A. T. S. Wee, *Nat. Commun.*, 2013, **4**, 1374.
31 M. Y. Han, B. Özyilmaz, Y. Zhang and P. Kim, *Phys. Rev. Lett.*, 2007, **98**, 206805.
32 X. Wang and H. Dai, *Nat. Chem.*, 2010, **2**, 661–665.
33 L. Jiao, X. Wang, G. Diankov, H. Wang and H. Dai, *Nat. Nanotechnol.*, 2010, **5**, 321–325.
34 Z. Chen, Y.-M. Lin, M. J. Rooks and P. Avouris, *Phys. E*, 2007, **40**, 228–232.
35 T. Shimizu, J. Haruyama, D. C. Marcano, D. V. Kosinkin, J. M. Tour, K. Hirose and K. Suenaga, *Nat. Nanotechnol.*, 2011, **6**, 45–50.
36 D. V. Kosynkin, A. L. Higginbotham, A. Sinitskii, J. R. Lomeda, A. Dimiev, B. K. Price and J. M. Tour, *Nature*, 2009, **458**, 872–876.
37 L. Jiao, L. Zhang, X. Wang, G. Diankov and H. Dai, *Nature*, 2009, **458**, 877–880.
38 F. Liu, Y. Hu, Z. Qu, X. Ma, Z. Li, R. Zhu, Y. Yan, B. Wen, Q. Ma, M. Liu, S. Zhao, Z. Fan, J. Zeng, M. Liu, Z. Jin and Z. Lin, *Proc. Natl. Acad. Sci. U. S. A.*, 2023, **120**, e2303262120.
39 C. Chen, Y. Lin, W. Zhou, M. Gong, Z. He, F. Shi, X. Li, J. Z. Wu, K. T. Lam, J. N. Wang, F. Yang, Q. Zeng, J. Guo, W. Gao, J.-M. Zuo, J. Liu, G. Hong, A. L. Antaris, M.-C. Lin, W. L. Mao and H. Dai, *Nat. Electron.*, 2021, **4**, 653–663.
40 A. Narita, X. Feng and K. Müllen, *Chem. Rec.*, 2015, **15**, 295–309.
41 A. Narita, Z. Chen, Q. Chen and K. Müllen, *Chem. Sci.*, 2019, **10**, 964–975.
42 Y. Huang, F. Xu, L. Ganzer, F. V. A. Camargo, T. Nagahara, J. Teyssandier, H. Van Gorp, K. Basse, L. A. Straasø, V. Nagyte, C. Casiraghi, M. R. Hansen, S. De Feyter, D. Yan, K. Müllen, X. Feng, G. Cerullo and Y. Mai, *J. Am. Chem. Soc.*, 2018, **140**, 10416–10420.

43 B. K. Sturdza, F. Kong, X. Yao, W. Niu, J. Ma, X. Feng, M. K. Riede, L. Bogani and R. J. Nicholas, *Nat. Commun.*, 2024, **15**, 2985.

44 Y. Yin, F. Xu, M. Wlazło, Y. Chen, G. Wen, G. Velpula, S. Böckmann, M. R. Hansen, S. De Feyter, K. S. Mali, W. Liu, S. Osella, M. Bonn, H. I. Wang, K. Müllen, X. Feng and Y. Mai, *J. Am. Chem. Soc.*, 2026, **148**, 5012–5021.

45 S. Song, Y. Teng, W. Tang, Z. Xu, Y. He, J. Ruan, T. Kojima, W. Hu, F. J. Giessibl, H. Sakaguchi, S. G. Louie and J. Lu, *Nature*, 2025, **637**, 580–586.

46 B. Lyu, J. Chen, S. Wang, S. Lou, P. Shen, J. Xie, L. Qiu, I. Mitchell, C. Li, C. Hu, X. Zhou, K. Watanabe, T. Taniguchi, X. Wang, J. Jia, Q. Liang, G. Chen, T. Li, S. Wang, W. Ouyang, O. Hod, F. Ding, M. Urbakh and Z. Shi, *Nature*, 2024, **628**, 758–764.

47 W. Niu, J. Ma and X. Feng, *Acc. Chem. Res.*, 2022, **55**, 3322–3333.

48 T. Nagahara, F. V. A. Camargo, F. Xu, L. Ganzer, M. Russo, P. Zhang, A. Perri, G. De La Cruz Valbuena, I. A. Heisler, C. D'Andrea, D. Polli, K. Müllen, X. Feng, Y. Mai and G. Cerullo, *Nano Lett.*, 2024, **24**, 797–804.

49 I. Ivanov, Y. Hu, S. Osella, U. Beser, H. I. Wang, D. Beljonne, A. Narita, K. Müllen, D. Turchinovich and M. Bonn, *J. Am. Chem. Soc.*, 2017, **139**, 7982–7988.

50 L. Talirz, H. Söde, T. Dumslaff, S. Wang, J. R. Sanchez-Valencia, J. Liu, P. Shinde, C. A. Pignedoli, L. Liang, V. Meunier, N. C. Plumb, M. Shi, X. Feng, A. Narita, K. Müllen, R. Fasel and P. Ruffieux, *ACS Nano*, 2017, **11**, 1380–1388.

51 K. Sun, P. Ji, J. Zhang, J. Wang, X. Li, X. Xu, H. Zhang and L. Chi, *Small*, 2019, **15**, 1804526.

52 J. H. Hwang, N. Bassi, M. Fadel, O. Braun, T. Dumslaff, C. A. Pignedoli, M. Stiefel, R. Furrer, H. Hayashi, H. Yamada, A. Narita, K. Müllen, M. Calame, M. Perrin, R. Fasel, P. Ruffieux, V. Meunier and G. Borin Barin, *ACS Nano*, 2025, **19**, 37230–37240.

53 Z. Chen, H. I. Wang, N. Bilbao, J. Teyssandier, T. Prechtl, N. Cavani, A. Tries, R. Biagi, V. De Renzi, X. Feng, M. Kläui, S. De Feyter, M. Bonn, A. Narita and K. Müllen, *J. Am. Chem. Soc.*, 2017, **139**, 9483–9486.

54 J. Yamaguchi, H. Hayashi, H. Jippo, A. Shiotari, M. Ohtomo, M. Sakakura, N. Hieda, N. Aratani, M. Ohfuchi, Y. Sugimoto, H. Yamada and S. Sato, *Commun. Mater.*, 2020, **1**, 36.

55 A. Kimouche, M. M. Ervasti, R. Drost, S. Halonen, A. Harju, P. M. Joensuu, J. Sainio and P. Liljeroth, *Nat. Commun.*, 2015, **6**, 10177.

56 R. E. Blackwell, F. Zhao, E. Brooks, J. Zhu, I. Piskun, S. Wang, A. Delgado, Y.-L. Lee, S. G. Louie and F. R. Fischer, *Nature*, 2021, **600**, 647–652.

57 A. Kinikar, X. Xu, M. D. Giovannantonio, O. Gröning, K. Eimre, C. A. Pignedoli, K. Müllen, A. Narita, P. Ruffieux and R. Fasel, *Adv. Mater.*, 2023, **35**, 2306311.

58 J. Lawrence, A. Berdonces-Layunta, S. Edalatmanesh, J. Castro-Esteban, T. Wang, A. Jimenez-Martin, B. de la Torre, R. Castrillo-Bodero, P. Angulo-Portugal, M. S. G. Mohammed, A. Matěj, M. Vilas-Varela, F. Schiller, M. Corso, P. Jelinek, D. Peña and D. G. de Oteyza, *Nat. Chem.*, 2022, **14**, 1451–1458.

59 F. Xiang, Y. Gu, A. Kinikar, N. Bassi, A. Ortega-Guerrero, Z. Qiu, O. Gröning, P. Ruffieux, C. A. Pignedoli, K. Müllen and R. Fasel, *Nat. Chem.*, 2025, **17**, 1356–1363.

60 W. Niu, J. Liu, Y. Mai, K. Müllen and X. Feng, *Trends Chem.*, 2019, **1**, 549–558.

61 J. Liu, B.-W. Li, Y.-Z. Tan, A. Giannakopoulos, C. Sanchez-Sanchez, D. Beljonne, P. Ruffieux, R. Fasel, X. Feng and K. Müllen, *J. Am. Chem. Soc.*, 2015, **137**, 6097–6103.

62 X. Wang, J. Ma, W. Zheng, S. Osella, N. Arisnabarreta, J. Droste, G. Serra, O. Ivasenko, A. Lucotti, D. Beljonne, M. Bonn, X. Liu, M. R. Hansen, M. Tommasini, S. De Feyter, J. Liu, H. I. Wang and X. Feng, *J. Am. Chem. Soc.*, 2022, **144**, 228–235.

63 K. Liu, W. Zheng, S. Osella, Z.-L. Qiu, S. Böckmann, W. Niu, L. Meingast, H. Komber, S. Obermann, R. Gillen, M. Bonn, M. R. Hansen, J. Maultzsch, H. I. Wang, J. Ma and X. Feng, *J. Am. Chem. Soc.*, 2024, **146**, 1026–1034.

64 S. Obermann, W. Zheng, J. Melidonie, S. Böckmann, S. Osella, N. Arisnabarreta, L. A. Guerrero-León, F. Hennersdorf, D. Beljonne, J. J. Weigand, M. Bonn, S. De Feyter, M. R. Hansen, H. I. Wang, J. Ma and X. Feng, *Chem. Sci.*, 2023, **14**, 8607–8614.

65 S. Obermann, X. Zhou, L. A. Guerrero-León, G. Serra, S. Böckmann, Y. Fu, E. Dmitrieva, J. Zhang, F. Liu, A. A. Popov, A. Lucotti, M. R. Hansen, M. Tommasini, Y. Li, P. W. M. Blom, J. Ma and X. Feng, *Angew. Chem., Int. Ed.*, 2024, **63**, e202415670.

66 Y. L. Li, C.-T. Zee, J. B. Lin, V. M. Basile, M. Muni, M. D. Flores, J. Munárriz, R. B. Kaner, A. N. Alexandrova, K. N. Houk, S. H. Tolbert and Y. Rubin, *J. Am. Chem. Soc.*, 2020, **142**, 18093–18102.

67 Q. Chen, A. Lodi, H. Zhang, A. Gee, H. I. Wang, F. Kong, M. Clarke, M. Edmondson, J. Hart, J. N. O'Shea, W. Stawski, J. Baugh, A. Narita, A. Saywell, M. Bonn, K. Müllen, L. Bogani and H. L. Anderson, *Nat. Chem.*, 2024, **16**, 1133–1140.

68 Y. Huang, W. Dou, F. Xu, H. Ru, Q. Gong, D. Wu, D. Yan, H. Tian, X. He, Y. Mai and X. Feng, *Angew. Chem., Int. Ed.*, 2018, **57**, 3366–3371.

69 A. Narita, X. Feng, Y. Hernandez, S. A. Jensen, M. Bonn, H. Yang, I. A. Verzhbitskiy, C. Casiraghi, M. R. Hansen, A. H. R. Koch, G. Fytas, O. Ivasenko, B. Li, K. S. Mali, T. Balandina, S. Mahesh, S. De Feyter and K. Müllen, *Nat. Chem.*, 2014, **6**, 126–132.

70 W. Niu, J. Ma, P. Soltani, W. Zheng, F. Liu, A. A. Popov, J. J. Weigand, H. Komber, E. Poliani, C. Casiraghi, J. Droste, M. R. Hansen, S. Osella, D. Beljonne, M. Bonn, H. I. Wang, X. Feng, J. Liu and Y. Mai, *J. Am. Chem. Soc.*, 2020, **142**, 18293–18298.

71 P. P. Shinde, J. Liu, T. Dienel, O. Gröning, T. Dumslaff, M. Mühlinghaus, A. Narita, K. Müllen, C. A. Pignedoli, R. Fasel, P. Ruffieux and D. Passerone, *Carbon*, 2021, **175**, 50–59.

72 L. Yang, J. Ma, W. Zheng, S. Osella, J. Droste, H. Komber, K. Liu, S. Böckmann, D. Beljonne, M. R. Hansen, M. Bonn, H. I. Wang, J. Liu and X. Feng, *Adv. Sci.*, 2022, **9**, 2200708.

73 J. Li, S. Sanz, N. Merino-Díez, M. Vilas-Varela, A. Garcia-Lekue, M. Corso, D. G. De Oteyza, T. Frederiksen, D. Peña and J. I. Pascual, *Nat. Commun.*, 2021, **12**, 5538.

74 X. Yao, W. Zheng, S. Osella, Z. Qiu, S. Fu, D. Schollmeyer, B. Müller, D. Beljonne, M. Bonn, H. I. Wang, K. Müllen and A. Narita, *J. Am. Chem. Soc.*, 2021, **143**, 5654–5658.

75 Y. Huang, Y. Mai, U. Beser, J. Teyssandier, G. Velpula, H. Van Gorp, L. A. Straasø, M. R. Hansen, D. Rizzo, C. Casiraghi, R. Yang, G. Zhang, D. Wu, F. Zhang, D. Yan, S. De Feyter, K. Müllen and X. Feng, *J. Am. Chem. Soc.*, 2016, **138**, 10136–10139.

76 Z. Chen, J. Huang, Q. Chen, Y. Wu, X. Chen, D. Han, W. Yang, H. Ding, J. Hu, Q. Xu, C. Wu, Q. Fan, P. Jelínek and J. Zhu, *J. Am. Chem. Soc.*, 2025, **147**, 44941–44949.

77 D. J. Rizzo, G. Veber, J. Jiang, R. McCurdy, T. Cao, C. Bronner, T. Chen, S. G. Louie, F. R. Fischer and M. F. Crommie, *Science*, 2020, **369**, 1597–1603.

78 Q. Fan, D. Martin-Jimenez, D. Ebeling, C. K. Krug, L. Brechmann, C. Kohlmeyer, G. Hilt, W. Hieringer, A. Schirmeisen and J. M. Gottfried, *J. Am. Chem. Soc.*, 2019, **141**, 17713–17720.

79 H. Qu, M. Zhao and W. Xu, *Chem. – Eur. J.*, 2025, **31**, e202501399.

80 J. Cai, C. A. Pignedoli, L. Talirz, P. Ruffieux, H. Söde, L. Liang, V. Meunier, R. Berger, R. Li, X. Feng, K. Müllen and R. Fasel, *Nat. Nanotechnol.*, 2014, **9**, 896–900.

81 O. Gröning, S. Wang, X. Yao, C. A. Pignedoli, G. Borin Barin, C. Daniels, A. Cupo, V. Meunier, X. Feng, A. Narita, K. Müllen, P. Ruffieux and R. Fasel, *Nature*, 2018, **560**, 209–213.

82 D. J. Rizzo, G. Veber, T. Cao, C. Bronner, T. Chen, F. Zhao, H. Rodriguez, S. G. Louie, M. F. Crommie and F. R. Fischer, *Nature*, 2018, **560**, 204–208.

83 D. Wang, D.-L. Bao, Q. Zheng, C.-T. Wang, S. Wang, P. Fan, S. Mishra, L. Tao, Y. Xiao, L. Huang, X. Feng, K. Müllen, Y.-Y. Zhang, R. Fasel, P. Ruffieux, S. Du and H.-J. Gao, *Nat. Commun.*, 2023, **14**, 1018.

84 S. Blankenburg, J. Cai, P. Ruffieux, R. Jaafar, D. Passerone, X. Feng, K. Müllen, R. Fasel and C. A. Pignedoli, *ACS Nano*, 2012, **6**, 2020–2025.

85 C. Bronner, R. A. Durr, D. J. Rizzo, Y.-L. Lee, T. Marangoni, A. M. Kalayjian, H. Rodriguez, W. Zhao, S. G. Louie, F. R. Fischer and M. F. Crommie, *ACS Nano*, 2018, **12**, 2193–2200.

86 C. Dobner, G. Li, M. Sarker, A. Sinitskii and A. Enders, *RSC Adv.*, 2022, **12**, 6615–6618.

87 V. Saraswat, R. M. Jacobberger and M. S. Arnold, *ACS Nano*, 2021, **15**, 3674–3708.

88 P. Ruffieux, S. Wang, B. Yang, C. Sánchez-Sánchez, J. Liu, T. Dienel, L. Talirz, P. Shinde, C. A. Pignedoli, D. Passerone, T. Dumslaff, X. Feng, K. Müllen and R. Fasel, *Nature*, 2016, **531**, 489–492.

89 C. Jiang, H. S. Wang, C. Liu, C. Chen, L. Chen, X. Wang, Y. Wang, Z. Kong, Y. Feng, Y. Liu, Y. Feng, Y. Zhang, Z. Wei, M. Guo, A. Tong, G. Mu, Y. Yang, K. Watanabe, T. Taniguchi, W. Shi and H. Wang, *Nat. Mater.*, 2025, **24**, 1592–1599.

90 X. Yao, H. Zhang, F. Kong, A. Hinaut, R. Pawlak, M. Okuno, R. Graf, P. N. Horton, S. J. Coles, E. Meyer, L. Bogani, M. Bonn, H. I. Wang, K. Müllen and A. Narita, *Angew. Chem., Int. Ed.*, 2023, **62**, e202312610.

91 N. Merino-Díez, A. Garcia-Lekue, E. Carbonell-Sanromà, J. Li, M. Corso, L. Colazzo, F. Sedona, D. Sánchez-Portal, J. I. Pascual and D. G. De Oteyza, *ACS Nano*, 2017, **11**, 11661–11668.

92 S. Lindenthal, D. Fazzi, N. F. Zorn, A. A. El Yumin, S. Settele, B. Weidinger, E. Blasco and J. Zaumseil, *ACS Nano*, 2023, **17**, 18240–18252.

93 F. M. Arnold, T.-J. Liu, A. Kuc and T. Heine, *Phys. Rev. Lett.*, 2022, **129**, 216401.

94 T. Wang, S. Sanz, J. Castro-Esteban, J. Lawrence, A. Berdonces-Layunta, M. S. G. Mohammed, M. Vilas-Varela, M. Corso, D. Peña, T. Frederiksen and D. G. De Oteyza, *Nano Lett.*, 2022, **22**, 164–171.

95 H. S. Wang, L. Chen, K. Elibol, L. He, H. Wang, C. Chen, C. Jiang, C. Li, T. Wu, C. X. Cong, T. J. Pennycook, G. Argentero, D. Zhang, K. Watanabe, T. Taniguchi, W. Wei, Q. Yuan, J. C. Meyer and X. Xie, *Nat. Mater.*, 2021, **20**, 202–207.

96 Q. Fan, Z. Ruan, S. Werner, T. Naumann, R. Bolat, J. Martinez-Castro, T. Koehler, T. Vollgraff, W. Hieringer, R. Mandalia, C. Neiß, A. Görling, F. S. Tautz, J. Sundermeyer and J. M. Gottfried, *Nano Lett.*, 2024, **24**, 10718–10723.

97 R. Pawlak, X. Liu, S. Ninova, P. D'Astolfo, C. Drechsel, S. Sangtarash, R. Häner, S. Decurtins, H. Sadeghi, C. J. Lambert, U. Aschauer, S.-X. Liu and E. Meyer, *J. Am. Chem. Soc.*, 2020, **142**, 12568–12573.

98 M. Sarker, C. Dobner, P. Zahl, C. Fiankor, J. Zhang, A. Saxena, N. Aluru, A. Enders and A. Sinitskii, *J. Am. Chem. Soc.*, 2024, **146**, 14453–14467.

99 S. Cheng, X. Su, F. Gan, C. Shen, H. Qiu, K. Tao and P. Yu, *J. Phys. Chem. C*, 2020, **124**, 756–763.

100 P. Angulo-Portugal, M. Irizar, L. Huang, M. Sarker, M. A. Ashoush, Z. M. A. El-Fattah, J. Barth, F. Schiller, A. El-Sayed, F. Gao, D. G. De Oteyza, A. Sinitskii, A. Garcia-Lekue, M. Corso and I. Piquero-Zulaica, *Adv. Mater.*, 2025, e11706.

101 D. Miao, V. Di Michele, F. Gagnon, C. Aumaître, A. Lucotti, M. Del Zoppo, F. Lirette, M. Tommasini and J.-F. Morin, *J. Am. Chem. Soc.*, 2021, **143**, 11302–11308.

102 J. Wang, Y. Zhu, G. Zhuang, Y. Wu, S. Wang, P. Huang, G. Sheng, M. Chen, S. Yang, T. Greber and P. Du, *Nat. Commun.*, 2022, **13**, 1239.

103 F. Xu, H. Yu, A. Sadrzadeh and B. I. Yakobson, *Nano Lett.*, 2016, **16**, 34–39.

104 P. H. Jacobse, Z. Jin, J. Jiang, S. Peurifoy, Z. Yue, Z. Wang, D. J. Rizzo, S. G. Louie, C. Nuckolls and M. F. Crommie, *Sci. Adv.*, 2021, **7**, eabl5892.

105 X. Xu, K. Sun, A. Ishikawa, A. Narita and S. Kawai, *Angew. Chem., Int. Ed.*, 2023, **62**, e202302534.

106 Y.-C. Chen, T. Cao, C. Chen, Z. Pedramrazi, D. Haberer, D. G. De Oteyza, F. R. Fischer, S. G. Louie and M. F. Crommie, *Nat. Nanotechnol.*, 2015, **10**, 156–160.

107 G. Li, K.-Y. Yoon, X. Zhong, J. Wang, R. Zhang, J. R. Guest, J. Wen, X.-Y. Zhu and G. Dong, *Nat. Commun.*, 2018, **9**, 1687.

108 X. Chang, L. Huang, Y. Gao, Y. Fu, J. Ma, H. Yang, J. Liu, X. Fu, X. Lin, X. Feng, S. Du and H.-J. Gao, *Nano Res.*, 2023, **16**, 10436–10442.

109 Y. Fu, H. Yang, Y. Gao, L. Huang, R. Berger, J. Liu, H. Lu, Z. Cheng, S. Du, H.-J. Gao and X. Feng, *Angew. Chem., Int. Ed.*, 2020, **59**, 8873–8879.

110 Y.-F. Zhang, Y. Zhang, G. Li, J. Lu, Y. Que, H. Chen, R. Berger, X. Feng, K. Müllen, X. Lin, Y.-Y. Zhang, S. Du, S. T. Pantelides and H.-J. Gao, *Nano Res.*, 2017, **10**, 3377–3384.

111 X.-Y. Wang, J. I. Urgel, G. B. Barin, K. Eimre, M. Di Giovannantonio, A. Milani, M. Tommasini, C. A. Pignedoli, P. Ruffieux, X. Feng, R. Fasel, K. Müllen and A. Narita, *J. Am. Chem. Soc.*, 2018, **140**, 9104–9107.

112 G. D. Nguyen, F. M. Toma, T. Cao, Z. Pedramrazi, C. Chen, D. J. Rizzo, T. Joshi, C. Bronner, Y.-C. Chen, M. Favaro, S. G. Louie, F. R. Fischer and M. F. Crommie, *J. Phys. Chem. C*, 2016, **120**, 2684–2687.

113 S. Kawai, S. Saito, S. Osumi, S. Yamaguchi, A. S. Foster, P. Spijker and E. Meyer, *Nat. Commun.*, 2015, **6**, 8098.

114 Y. Zhao, L.-X. Kang, Y.-J. Wang, Y. Wu, G.-Y. Xing, S.-W. Li, J. Pan, N.-W. Wang, Y.-T. Ren, Y. Wang, Y.-C. Zhu, X.-Q. Shi, M. Liu, X. Qiu, P.-N. Liu and D.-Y. Li, *Angew. Chem., Int. Ed.*, 2025, **64**, e202500490.

115 N. Friedrich, P. Brandimarte, J. Li, S. Saito, S. Yamaguchi, I. Pozo, D. Peña, T. Frederiksen, A. Garcia-Lekue, D. Sánchez-Portal and J. I. Pascual, *Phys. Rev. Lett.*, 2020, **125**, 146801.

116 S. Kawai, S. Nakatsuka, T. Hatakeyama, R. Pawlak, T. Meier, J. Tracey, E. Meyer and A. S. Foster, *Sci. Adv.*, 2018, **4**, eaar7181.

117 X.-Y. Wang, X. Yao, A. Narita and K. Müllen, *Acc. Chem. Res.*, 2019, **52**, 2491–2505.

118 A. Takahashi, C.-J. Lin, K. Ohshimizu, T. Higashihara, W.-C. Chen and M. Ueda, *Polym. Chem.*, 2012, **3**, 479–485.

119 D. Miao, M. Daigle, A. Lucotti, J. Boismenu-Lavoie, M. Tommasini and J.-F. Morin, *Angew. Chem., Int. Ed.*, 2018, **57**, 3588–3592.

120 E. C. H. Wen, P. H. Jacobse, J. Jiang, Z. Wang, S. G. Louie, M. F. Crommie and F. R. Fischer, *J. Am. Chem. Soc.*, 2023, **145**, 19338–19346.

121 Y. L. Li, C.-T. Zee, J. B. Lin, V. M. Basile, M. Muni, M. D. Flores, J. Munárriz, R. B. Kaner, A. N. Alexandrova, K. N. Houk, S. H. Tolbert and Y. Rubin, *J. Am. Chem. Soc.*, 2020, **142**, 18093–18102.

122 Y. Zhang, J. Lu, Y. Li, B. Li, Z. Ruan, H. Zhang, Z. Hao, S. Sun, W. Xiong, L. Gao, L. Chen and J. Cai, *Angew. Chem., Int. Ed.*, 2022, **61**, e202204736.

123 E. C. H. Wen, P. H. Jacobse, J. Jiang, Z. Wang, R. D. McCurdy, S. G. Louie, M. F. Crommie and F. R. Fischer, *J. Am. Chem. Soc.*, 2022, **144**, 13696–13703.

124 L. Chen, Y. Hernandez, X. Feng and K. Müllen, *Angew. Chem., Int. Ed.*, 2012, **51**, 7640–7654.

125 S. Song, J. Su, M. Telychko, J. Li, G. Li, Y. Li, C. Su, J. Wu and J. Lu, *Chem. Soc. Rev.*, 2021, **50**, 3238–3262.

126 Z. Chen, A. Narita and K. Müllen, *Adv. Mater.*, 2020, **32**, 2001893.

127 X. Zhou and G. Yu, *Adv. Mater.*, 2020, **32**, 1905957.

128 T. H. Vo, M. Shekhirev, D. A. Kunkel, M. D. Morton, E. Berglund, L. Kong, P. M. Wilson, P. A. Dowben, A. Enders and A. Sinitskii, *Nat. Commun.*, 2014, **5**, 3189.

129 R. K. Dubey, M. Marongiu, S. Fu, G. Wen, M. Bonn, H. I. Wang, M. Melle-Franco and A. Mateo-Alonso, *Chem*, 2023, **9**, 2983–2996.

130 J. Yin, P. H. Jacobse, D. Pyle, Z. Wang, M. F. Crommie and G. Dong, *J. Am. Chem. Soc.*, 2022, **144**, 16012–16019.

131 R. K. Dubey, M. Melle-Franco and A. Mateo-Alonso, *J. Am. Chem. Soc.*, 2021, **143**, 6593–6600.

132 D. Cortizo-Lacalle, J. P. Mora-Fuentes, K. Strutyński, A. Saeki, M. Melle-Franco and A. Mateo-Alonso, *Angew. Chem., Int. Ed.*, 2018, **57**, 703–708.

133 K. Yang, Z. Li and Z. Zeng, *Chem*, 2023, **9**, 2730–2732.

134 F. Hernández-Culebras, M. Melle-Franco and A. Mateo-Alonso, *Angew. Chem., Int. Ed.*, 2022, **61**, e202205018.

135 J. Zhang, K. Liu, Y. Xiao, X. Yu, L. Huang, H. Gao, J. Ma and X. Feng, *Angew. Chem., Int. Ed.*, 2023, **62**, e202310880.

136 J. Ma and X. Feng, *Chem*, 2024, **10**, 435–437.

137 S. Von Kugelgen, I. Piskun, J. H. Griffin, C. T. Eckdahl, N. N. Jarenwattananon and F. R. Fischer, *J. Am. Chem. Soc.*, 2019, **141**, 11050–11058.

138 H. Shen, Y. Shi and X. Wang, *Synth. Met.*, 2015, **210**, 109–122.

139 P. H. Jacobse, M. J. J. Mangnus, S. J. M. Zevenhuizen and I. Swart, *ACS Nano*, 2018, **12**, 7048–7056.

140 M. Kolmer, A.-K. Steiner, I. Izydorczyk, W. Ko, M. Engelund, M. Szymonski, A.-P. Li and K. Amsharov, *Science*, 2020, **369**, 571–575.

141 R. Zuzak, J. Castro-Esteban, M. Engelund, D. Pérez, D. Peña and S. Godlewski, *ACS Nano*, 2023, **17**, 2580–2587.

142 A. Keerthi, C. Sánchez-Sánchez, O. Deniz, P. Ruffieux, D. Schollmeyer, X. Feng, A. Narita, R. Fasel and K. Müllen, *Chem. – Asian J.*, 2020, **15**, 3807–3811.

143 P.-H. Gao, C. Chen and X.-Y. Wang, *Chin. J. Chem.*, 2024, **42**, 2877–2894.

144 J.-J. Zhang, J. Ma and X. Feng, *Macromol. Chem. Phys.*, 2023, **224**, 2200232.

145 K. Matsumoto, A. Onoda, T. Kitano, T. Sakata, H. Yasuda, S. Campidelli and T. Hayashi, *ACS Appl. Mater. Interfaces*, 2021, **13**, 15101–15112.

146 Z. Feng, A. Mazaheripour, D. J. Dibble, P. Wagner, G. Czap, G. Kladnik, A. Cossaro, A. Verdini, L. Floreano, G. Bavdek, W. Ho, G. Comelli, D. Cvetko, A. Morgante and A. A. Gorodetsky, *Carbon*, 2020, **170**, 677–684.

147 T. H. Vo, U. G. E. Perera, M. Shekhirev, M. Mehdi Pour, D. A. Kunkel, H. Lu, A. Gruverman, E. Sutter, M. Cotlet, D. Nykypanchuk, P. Zahl, A. Enders, A. Sinitskii and P. Sutter, *Nano Lett.*, 2015, **15**, 5771–5777.

148 D. J. Dibble, Y. S. Park, A. Mazaheripour, M. J. Umerani, J. W. Ziller and A. A. Gorodetsky, *Angew. Chem., Int. Ed.*, 2015, **54**, 5883–5887.

149 C. Bronner, S. Stremlau, M. Gille, F. Brauße, A. Haase, S. Hecht and P. Tegeder, *Angew. Chem., Int. Ed.*, 2013, **52**, 4422–4425.

150 P. Zhang, Y. Fei, Q. Zeng, J. Xu, F. Li, J. Mao, C. Xia, Y. Chen, J. Liu, Y. Wang, X. Wang, J. Ju, L. Meng, H. Bai,

H. Dong, X. Tang, D. Gao, X. Wang, X. Dong, H. Mao, H. Zheng and K. Li, *Angew. Chem.*, 2025, **137**, e202510339.

151 X. Wang, F. Zhang, K. S. Schellhammer, P. Machata, F. Ortmann, G. Cuniberti, Y. Fu, J. Hunger, R. Tang, A. A. Popov, R. Berger, K. Müllen and X. Feng, *J. Am. Chem. Soc.*, 2016, **138**, 11606–11615.

152 J. Zhang, Q. Jiang, Q. Cheng, R. Wang, R. Jia, C. Liu, Y. Xiong, W. Han, Z. Jin, C. Nuckolls and L. Jiang, *Chem*, 2026, 102835.

153 S. T. Bao, Y. Hong, H. Jiang, L. T. Lackovic, S. Louie, D. Xu, F. Ng, N. Olsen, X. Zhu, M. L. Steigerwald, M. Delor, C. Nuckolls and Q. Jiang, *Angew. Chem., Int. Ed.*, 2025, **64**, e202508426.

154 E. Carbonell-Sanromà, J. Hieulle, M. Vilas-Varela, P. Brandimarte, M. Iraola, A. Barragán, J. Li, M. Abadia, M. Corso, D. Sánchez-Portal, D. Peña and J. I. Pascual, *ACS Nano*, 2017, **11**, 7355–7361.

155 A. Götz, X.-Y. Wang, A. Ruini, W. Zheng, P. Soltani, R. Graf, A. Tries, J. Li, C.-A. Palma, E. Molinari, M. R. Hansen, H. I. Wang, D. Prezzi, K. Müllen and A. Narita, *J. Mater. Chem. C*, 2022, **10**, 4173–4181.

156 Y.-Z. Tan, B. Yang, K. Parvez, A. Narita, S. Osella, D. Beljonne, X. Feng and K. Müllen, *Nat. Commun.*, 2013, **4**, 2646.

157 A. Nandgaye, K. Ghosh, S. Yamijala and K. Rao, *Angew. Chem., Int. Ed.*, 2025, **64**, e202418955.

158 S. R. Peurifoy, Q. Xu, R. May, N. A. Gadjieva, T. J. Sisto, Z. Jin, L. E. Marbella and C. Nuckolls, *Chem. Sci.*, 2020, **11**, 9978–9982.

159 S. Louie, Q. Jiang, D. J. Wisniewski, S. Tong, H. Zhang, K. Chivukula, Q. Fang, A. Garudapalli, S. R. Docherty, F. Ng, M. Steigerwald, Y. Zhong, D. Khodagholy and C. Nuckolls, *Sci. Adv.*, 2025, 1–7.

160 A. Keerthi, B. Radha, D. Rizzo, H. Lu, V. Diez Cabanes, I. C.-Y. Hou, D. Beljonne, J. Cornil, C. Casiraghi, M. Baumgarten, K. Müllen and A. Narita, *J. Am. Chem. Soc.*, 2017, **139**, 16454–16457.

161 W.-T. Dou, F. Xu, C.-X. Xu, J. Gao, H.-B. Ru, X. Luan, J. Zhang, L. Zhu, A. C. Sedgwick, G.-R. Chen, Y. Zang, T. D. James, H. Tian, J. Li, Y. Mai and X.-P. He, *Chem. Sci.*, 2021, **12**, 11089–11097.

162 F. Xu, C. Yu, A. Tries, H. Zhang, M. Kläui, K. Basse, M. R. Hansen, N. Bilbao, M. Bonn, H. I. Wang and Y. Mai, *J. Am. Chem. Soc.*, 2019, **141**, 10972–10977.

163 D. Joshi, M. Hauser, G. Veber, A. Berl, K. Xu and F. R. Fischer, *J. Am. Chem. Soc.*, 2018, **140**, 9574–9580.

164 M. Edmondson, M. Clarke, J. N. O'Shea, Q. Chen, H. L. Anderson and A. Saywell, *ACS Nano*, 2024, **18**, 33390–33397.

165 N. Friedrich, R. E. Menchón, I. Pozo, J. Hieulle, A. Vegliante, J. Li, D. Sánchez-Portal, D. Peña, A. Garcia-Lekue and J. I. Pascual, *ACS Nano*, 2022, **16**, 14819–14826.

166 J. Deyerling, M. Pörtner, L. Đorđević, A. Riss, D. Bonifazi and W. Auwärter, *J. Phys. Chem. C*, 2022, **126**, 8467–8476.

167 Z. Chen, J.-R. Deng, S. Hou, X. Bian, J. L. Swett, Q. Wu, J. Baugh, L. Bogani, G. A. D. Briggs, J. A. Mol, C. J. Lambert, H. L. Anderson and J. O. Thomas, *J. Am. Chem. Soc.*, 2023, **145**, 15265–15274.

168 R. Pawlak, K. N. Anindya, T. Shimizu, J.-C. Liu, T. Sakamaki, R. Shang, A. Rochefort, E. Nakamura and E. Meyer, *J. Phys. Chem. C*, 2022, **126**, 19726–19732.

169 F. Villalobos, J. I. Mendieta-Moreno, J. Lobo-Checa, S. P. Morcillo, J. I. Martínez, J. M. Gómez-Fernández, P. L. De Andres, J. A. Martin-Gago, J. M. Cuerva, A. G. Campaña and C. Sánchez-Sánchez, *J. Am. Chem. Soc.*, 2025, **147**, 7245–7254.

170 M. Liu, M. Liu, L. She, Z. Zha, J. Pan, S. Li, T. Li, Y. He, Z. Cai, J. Wang, Y. Zheng, X. Qiu and D. Zhong, *Nat. Commun.*, 2017, **8**, 14924.

171 T. G. Lohr, J. I. Urgel, K. Eimre, J. Liu, M. Di Giovannantonio, S. Mishra, R. Berger, P. Ruffieux, C. A. Pignedoli, R. Fasel and X. Feng, *J. Am. Chem. Soc.*, 2020, **142**, 13565–13572.

172 X. Zhu, K. Li, J. Liu, Z. Wang, Z. Ding, Y. Su, B. Yang, K. Yan, G. Li and P. Yu, *J. Am. Chem. Soc.*, 2024, **146**, 7152–7158.

173 Q. Fan, L. Yan, M. W. Tripp, O. Krejčí, S. Dimosthenous, S. R. Kachel, M. Chen, A. S. Foster, U. Koert, P. Liljeroth and J. M. Gottfried, *Science*, 2021, **372**, 1–5.

174 P. Mathey, Q. Sobczak, A. Darvish and J.-F. Morin, *Chem. Commun.*, 2024, **60**, 4854–4857.

175 D. S. Gomes, I. M. Felix, W. F. Radel, A. C. Dias, L. A. R. Junior and M. L. P. Junior, *Nano Lett.*, 2025, **25**, 8596–8603.

176 C. Moreno, X. Diaz De Cerio, M. Tenorio, F. Gao, M. Vilas-Varela, A. Sarasola, D. Peña, A. Garcia-Lekue and A. Mugarza, *Commun. Chem.*, 2024, **7**, 219.

177 C. Moreno, M. Vilas-Varela, B. Kretz, A. Garcia-Lekue, M. V. Costache, M. Paradinas, M. Panighel, G. Ceballos, S. O. Valenzuela, D. Peña and A. Mugarza, *Science*, 2018, **360**, 199–203.

178 I. Alcón, A. W. Cummings, E. Ribas, S. Roche and A. Mugarza, *Nanoscale Adv.*, 2025, **7**, 5932–5943.

179 M. R. Ajayakumar, M. Di Giovannantonio, C. A. Pignedoli, L. Yang, P. Ruffieux, J. Ma, R. Fasel and X. Feng, *J. Polym. Sci.*, 2022, **60**, 1912–1917.

180 R. Yin, J. Wang, Z.-L. Qiu, J. Meng, H. Xu, Z. Wang, Y. Liang, X.-J. Zhao, C. Ma, Y.-Z. Tan, Q. Li and B. Wang, *J. Am. Chem. Soc.*, 2022, **144**, 14798–14808.

181 W. Niu, Y. Fu, G. Serra, K. Liu, J. Droste, Y. Lee, Z. Ling, F. Xu, J. D. Cojal González, A. Lucotti, J. P. Rabe, M. Ryan Hansen, W. Pisula, P. W. M. Blom, C.-A. Palma, M. Tommasini, Y. Mai, J. Ma and X. Feng, *Angew. Chem., Int. Ed.*, 2023, **62**, e202305737.

182 K. Liu, G. Wen, G. Serra, N. Arisnabarreta, H. Yu, A. Lucotti, Y. P. Walg, H. Komber, Z.-L. Qiu, Q.-S. Deng, R. He, W. Niu, T. Heine, E. Brunner, M. Bonn, S. De Feyter, M. Tommasini, H. I. Wang, J. Ma and X. Feng, *Angew. Chem., Int. Ed.*, 2026, e24299.

183 M. Di Giovannantonio, K. Eimre, A. V. Yakutovich, Q. Chen, S. Mishra, J. I. Urgel, C. A. Pignedoli, P. Ruffieux, K. Müllen, A. Narita and R. Fasel, *J. Am. Chem. Soc.*, 2019, **141**, 12346–12354.

184 F. Kang, L. Sun, W. Gao, Q. Sun and W. Xu, *ACS Nano*, 2023, **17**, 8717–8722.

185 M. Shekhirev, P. Zahl and A. Sinitskii, *ACS Nano*, 2018, **12**, 8662–8669.

186 M. Daigle, D. Miao, A. Lucotti, M. Tommasini and J.-F. Morin, *Angew. Chem., Int. Ed.*, 2017, **56**, 6213–6217.

187 Y.-Y. He, J. Chen, X.-L. Zheng, X. Xu, W.-Q. Li, L. Yang and W. Q. Tian, *ACS Appl. Nano Mater.*, 2019, **2**, 1648–1654.

188 D.-B. Zhang and S.-H. Wei, *Npj Comput. Mater.*, 2017, **3**, 32–36.

189 A. V. Savin, E. A. Korznikova and S. V. Dmitriev, *Mech. Mater.*, 2019, **137**, 103123.

190 M. Saiz-Bretín, F. Domínguez-Adame and A. V. Malyshev, *Carbon*, 2019, **149**, 587–593.

191 R. Farghadan, *Phys. Rev. B*, 2024, **110**, 75132.

192 Z.-P. Liu, Y.-D. Guo, X.-H. Yan, H.-L. Zeng, X.-Y. Mou, Z.-R. Wang and J.-J. Wang, *J. Appl. Phys.*, 2019, **126**, 144303.

193 Y. Zhou, X. Zhang, G. Sheng, S. Wang, M. Chen, G. Zhuang, Y. Zhu and P. Du, *Nat. Commun.*, 2023, **14**, 5831.

194 B. Zhao, Z. Zhang, J. Xu, D. Guo, T. Gu, G. He, P. Lu, K. He, J. Li, Z. Chen, Q. Ren, L. Miao, J. Lu, Z. Ni, X. Duan and X. Duan, *Science*, 2025, **388**, 0–6.

195 J. Low, J. Yu, M. Jaroniec, S. Wageh and A. A. Al-Ghamdi, *Adv. Mater.*, 2017, **29**, 1601694.

196 H. Wang, L. Zhang, Z. Chen, J. Hu, S. Li, Z. Wang, J. Liu and X. Wang, *Chem. Soc. Rev.*, 2014, **43**, 5234.

197 Y. Liu, N. O. Weiss, X. Duan, H.-C. Cheng, Y. Huang and X. Duan, *Nat. Rev. Mater.*, 2016, **1**, 16042.

198 Z. F. Wang, Q. Li, Q. W. Shi, X. Wang, J. G. Hou, H. Zheng and J. Chen, *Appl. Phys. Lett.*, 2008, **92**, 133119.

199 X.-K. Chen, Z.-X. Xie, W.-X. Zhou, L.-M. Tang and K.-Q. Chen, *Carbon*, 2016, **100**, 492–500.

200 Y. Zhang, J. Lu, L. Gao, X. Zhao, G. Niu, X. Geng, Y. Zhang, S. Li, Y. Yang, Y.-Z. Tan, S. Du and J. Cai, *Nat. Commun.*, 2025, **16**, 5988.

201 P. Jiang, X. Tao, L. Kang, H. Hao, L. Song, J. Lan, X. Zheng, L. Zhang and Z. Zeng, *J. Phys. Appl. Phys.*, 2019, **52**, 015303.

202 B. Bian, J. Yang, X. Han, P. Yuan and Y. Ding, *Mod. Phys. Lett. B*, 2018, **32**, 1850395.

203 T. D. S. A. Cassiano, L. A. R. Júnior, G. M. E. Silva and P. H. D. O. Neto, *Adv. Theory Simul.*, 2023, **6**, 2200877.

204 Y. Ni, K. Yao, H. Fu, G. Gao, S. Zhu and S. Wang, *Sci. Rep.*, 2013, **3**, 1380.

205 L. M. Mateo, Q. Sun, K. Eimre, C. A. Pignedoli, T. Torres, R. Fasel and G. Bottari, *Chem. Sci.*, 2021, **12**, 247–252.

206 X. Zhang, Y. Hu, C. R. Lien-Medrano, J. Li, J. Shi, X. Qin, Z. Liao, Y. Wang, Z. Wang, J. Li, J. Chen, G. Zhang, J. V. Barth, T. Frauenheim, W. Auwärter, A. Narita, K. Müllen and C.-A. Palma, *J. Am. Chem. Soc.*, 2023, **145**, 8757–8763.

207 P. S. Costa, J. D. Teeter, A. Enders and A. Sinitskii, *Carbon*, 2018, **134**, 310–315.

208 G. D. Nguyen, H.-Z. Tsai, A. A. Omrani, T. Marangoni, M. Wu, D. J. Rizzo, G. F. Rodgers, R. R. Cloke, R. A. Durr, Y. Sakai, F. Liou, A. S. Aikawa, J. R. Chelikowsky, S. G. Louie, F. R. Fischer and M. F. Crommie, *Nat. Nanotechnol.*, 2017, **12**, 1077–1082.

209 W. Perkins and F. R. Fischer, *Chem. – Eur. J.*, 2017, **23**, 17687–17691.

210 K. Sun, O. Krejči, A. S. Foster, Y. Okuda, A. Orita and S. Kawai, *J. Phys. Chem. C*, 2019, **123**, 17632–17638.

211 D. J. Rizzo, M. Wu, H.-Z. Tsai, T. Marangoni, R. A. Durr, A. A. Omrani, F. Liou, C. Bronner, T. Joshi, G. D. Nguyen, G. F. Rodgers, W.-W. Choi, J. H. Jørgensen, F. R. Fischer, S. G. Louie and M. F. Crommie, *Nano Lett.*, 2019, **19**, 3221–3228.

212 S. Xing, B. Liu, W. Wang, J. Guo and W. Wang, *Chem. – Asian J.*, 2018, **13**, 2023–2026.

213 S. Wang, N. Kharche, E. Costa Girão, X. Feng, K. Müllen, V. Meunier, R. Fasel and P. Ruffieux, *Nano Lett.*, 2017, **17**, 4277–4283.

214 H. Noguchi, K. Hojo and M. Suginome, *J. Am. Chem. Soc.*, 2007, **129**, 758–759.

215 J.-F. Lutz, M. Ouchi, D. R. Liu and M. Sawamoto, *Science*, 2013, **341**, 1238149.

216 M. A. Baker, C. Tsai and K. J. T. Noonan, *Chem. – Eur. J.*, 2018, **24**, 13078–13088.

217 C. Xu, C. He, N. Li, S. Yang, Y. Du, K. Matyjaszewski and X. Pan, *Nat. Commun.*, 2021, **12**, 5853.

218 C. Xu, J. Dong, C. He, J. Yun and X. Pan, *Giant*, 2023, **14**, 100154.

219 J. Yin, H. Wang, D. Pyle, S. Choi, Y. Liu, J. Wen, J. R. Guest, J. W. Lyding and G. Dong, *ACS Nano*, 2025, **19**, 4366–4376.

220 J. Yin, S. Choi, D. Pyle, J. R. Guest and G. Dong, *J. Am. Chem. Soc.*, 2023, **145**, 19120–19128.

221 E. E. Sheina, J. Liu, M. C. Iovu, D. W. Laird and R. D. McCullough, *Macromolecules*, 2004, **37**, 3526–3528.

222 T. Yokozawa and A. Yokoyama, *Chem. Rev.*, 2009, **109**, 5595–5619.

223 A. Yokoyama, H. Suzuki, Y. Kubota, K. Ohuchi, H. Higashimura and T. Yokozawa, *J. Am. Chem. Soc.*, 2007, **129**, 7236–7237.

224 C. W. Bielawski and R. H. Grubbs, *Prog. Polym. Sci.*, 2007, **32**, 1–29.

225 P. Chen, *Acc. Chem. Res.*, 2016, **49**, 1052–1060.

226 K. Parkatzidis, H. S. Wang, N. P. Truong and A. Anastasaki, *Chem*, 2020, **6**, 1575–1588.

227 J. Lee, H. Ryu, S. Park, M. Cho and T.-L. Choi, *J. Am. Chem. Soc.*, 2023, **145**, 15488–15495.

228 S. H. Pun, A. Delgado, C. Dadich, A. Cronin and F. R. Fischer, *Chem*, 2024, **10**, 675–685.

229 P. H. Jacobse, M. Pizzochero, E. C. H. Wen, G. B. Barin, X. Li, Z. Mutlu, K. Müllen, E. Kaxiras, M. F. Crommie and F. R. Fischer, *ACS Nano*, 2025, **19**, 13029–13036.